

BRNO UNIVERSITY OF TECHNOLOGY

Faculty of Mechanical Engineering

DOCTORAL THESIS

Brno, 2020

Ing. Mgr. RADIM SKOUPÝ



BRNO UNIVERSITY OF TECHNOLOGY

VYSOKÉ UČENÍ TECHNICKÉ V BRNĚ

FACULTY OF MECHANICAL ENGINEERING

FAKULTA STROJNÍHO INŽENÝRSTVÍ

INSTITUTE OF PHYSICAL ENGINEERING

ÚSTAV FYZIKÁLNÍHO INŽENÝRSTVÍ

**QUANTITATIVE IMAGING IN SCANNING ELECTRON
MICROSCOPE**

KVANTITATIVNÍ ZOBRAZOVÁNÍ V RASTROVACÍM ELEKTRONOVÉM MIKROSKOPU

DOCTORAL THESIS

DIZERTAČNÍ PRÁCE

AUTHOR

AUTOR PRÁCE

Ing. Mgr. Radim Skoupý

ADVISOR

VEDOUCÍ PRÁCE

Ing. Vladislav Krzyžánek, Ph.D.

BRNO 2020

This doctoral thesis was created at



in Electron Microscopy Department,
group of Microscopy for Biomedicine
under supervision of Ing. Vladislav Krzyžánek, Ph.D.

ABSTRACT

This thesis deals with the possibilities of quantitative imaging in scanning (transmission) electron microscope (S|T|EM) together with its correlative applications. It starts with quantitative STEM (qSTEM) method description, where estimated local sample thickness can be related to irradiated dose and create a mass-loss study, which was applied on samples of ultrathin epoxy resin sections at variate conditions (age, temperature, staining, plasma cleaning, carbon covering, probe current). The possibilities of the detector calibration process, the necessary background of the Monte Carlo simulations of electron scattering and achievable accuracy of the method are discussed and demonstrated.

The method is then extrapolated for the use of back-scattered electron (BSE) detector, where new detector calibration technique, based on primary beam deflection on electron mirror, was postulated, developed and tested on various thin coating layers with thicknesses in range from 1 to 25 nm. The use of BSE detector brings the opportunity to measure the thickness of not only the electron transparent samples as in case of qSTEM, but also thin layers on substrates – qBSE. Both above-mentioned methods (qSTEM and qBSE) are intensity-based. This brings complication in the need of proper calibration, where just a slight drift of base-signal level causes a significant change of the results. This insufficiency was overcome in case of qSTEM by using the most probable scattering angle (captured by pixelated STEM detector) instead of an integral image intensity captured by an annular segment of STEM detector. The advantage of this method is its applicability post-acquisition, where no special previous actions are needed before each imaging session. The disadvantage is the limited range of detectable thicknesses given by the peak creation in signal/scattering-angle dependency. In general, low thickness region is immeasurable as well as those too thick (usable thickness range for latex is ~ 185 -1,000 nm; given by detection geometry and pixel size).

Moreover, multiple applications of conventional and commercially available quantitative techniques of cathodoluminescence (CL) and energy-dispersive X-ray spectroscopy (EDX) are presented in correlation with high-resolution images taken in secondary and transmitted electrons.

KEYWORDS

low-voltage STEM, SEM, quantitative imaging, qSTEM, qBSE, detector calibration, mass-loss, radiation caused damage, Monte Carlo simulation of electron scattering, coating layer thickness, electron mirror calibration, pixelated STEM detector, 4D STEM, calibration-less qSTEM, local sample thickness, EDX, CL, correlative imaging, cryo-SEM

ABSTRAKT

Tato práce se zabývá možnostmi kvantitativního zobrazování ve skenovacím (transmisním) elektronovém mikroskopu (S|T|EM) společně s jejich korelativní aplikací. Práce začíná popisem metody kvantitativního STEM (qSTEM), kde lze stanovenou lokální tloušťku vzorku dát do spojitosti s ozářenou dávkou, a vytvořit tak studii úbytku hmoty. Tato metoda byla použita při studiu ultratenkých řezů zalévací epoxidové pryskyřice za různých podmínek (stáří, teplota, kontrastování, čištění pomocí plazmy, pokrytí uhlíkem, proud ve svazku). V rámci této části jsou diskutovány a demonstrovány možnosti kalibračního procesu detektoru, nezbytné pozadí Monte Carlo simulací elektronového rozptylu a dosažitelná přesnost metody.

Metoda je pak rozšířena pro použití detektoru zpětně odražených elektronů (BSE), kde byla postulována, vyvinuta a testována nová kalibrační technika založená na odrazu primárního svazku na elektronovém zrcadle. Testovací vzorky byly různě tenké vrstvy v tloušťkách mezi 1 až 25 nm. Použití detektoru BSE přináší možnost měřit tloušťku nejen elektronově průhledných vzorků jako v případě qSTEM, ale také tenkých vrstev na substrátech - qBSE. Obě výše uvedené metody (qSTEM a qBSE) jsou založeny na intenzitě zaznamenaného obrazu, a to přináší komplikaci, protože vyžadují správnou kalibraci detektoru, kde jen malý posun úrovně základního signálu způsobí významnou změnu výsledků. Tato nedostatečnost byla překonána v případě qSTEM použitím nejpravděpodobnějšího úhlu rozptylu (zachyceného pixelovaným STEM detektorem), namísto integrální intenzity obrazu zachycené prstencovým segmentem detektoru STEM. Výhodou této metody je její použitelnost i na data, která nebyla předem zamýšlena pro využití qSTEM, protože pro aplikaci metody nejsou potřeba žádné zvláštní předchozí kroky. Nevýhodou je omezený rozsah detekovatelných tlouštěk vzorku způsobený absencí píku v závislosti signálu na úhlu rozptylu. Obecně platí, že oblast s malou tloušťkou je neměřitelná stejně tak jako tloušťka příliš silná (použitelný rozsah je pro latex $\sim 185 - 1\,000$ nm; rozsah je daný geometrií detekce a velikostí pixelů).

Navíc jsou v práci prezentovány korelativní aplikace konvenčních a komerčně dostupných kvantitativních technik katodoluminiscence (CL) a rentgenové energiově disperzní spektroskopie (EDX) spolu s vysokorozlišovacími obrazy vytvořenými pomocí sekundárních a prošlých elektronů.

KLÍČOVÁ SLOVA

nízkonapěťový STEM, SEM, kvantitativní zobrazování, qSTEM, qBSE, kalibrace detektoru, úbytek hmoty, radiační poškození, Monte Carlo simulace elektronového rozptylu, tloušťka krycí vrstvy, kalibrace pomocí elektronového zrcadla, pixelovaný STEM detektor, 4D STEM, bezkalibrační qSTEM, lokální tloušťka vzorku, EDX, CL, korelativní zobrazování, kryo-SEM

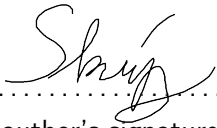
SKOUPÝ, Radim. *Quantitative imaging in scanning electron microscope*. Brno, 2020, 100 p. Doctoral thesis. Brno University of Technology, Faculty of Mechanical Engineering, Institute of physical engineering. Advised by Ing. Vladislav Krzyžánek, Ph.D.

DECLARATION

I declare that I have written the Doctoral Thesis titled “Quantitative imaging in scanning electron microscope” independently, under the guidance of the advisor and using exclusively the technical references and other sources of information cited in the thesis and listed in the comprehensive bibliography at the end of the thesis.

As the author I furthermore declare that, with respect to the creation of this Doctoral Thesis, I have not infringed any copyright or violated anyone’s personal and/or ownership rights. In this context, I am fully aware of the consequences of breaking Regulation § 11 of the Copyright Act No. 121/2000 Coll. of the Czech Republic, as amended, and of any breach of rights related to intellectual property or introduced within amendments to relevant Acts such as the Intellectual Property Act or the Criminal Code, Act No. 40/2009 Coll., Section 2, Head VI, Part 4.

Brno 20/9/2020


.....

author's signature

ACKNOWLEDGEMENT

I would like to express my gratitude and appreciation to supervisor Ing. Vladislav Krzyžánek, Ph.D. for his help during my work not only on this project and for all his time and attention he has dedicated to me during my Ph.D. studies. Of course, I would like to thank my colleagues from the group of Microscopy for Biomedicine and other colleagues from Institute of Scientific Instruments of the Czech Academy of Sciences, who helped me many times during the past six years.

Last but not least I would like to thank the financial support of various grants and projects: the Czech Academy of Sciences (project RVO:68081731), the Czech Science Foundation (GA14-20012S, GA17-15451S), the Technology Agency of the Czech Republic (TE01020118, TN01000008), the Ministry of Industry and Trade of the Czech Republic (TRIO FV30271), the Ministry of Education, Youth and Sports of the Czech Republic (LO1212), its infrastructure by Ministry of Education, Youth and Sports of the Czech Republic and European Commission (project CZ.1.05/2.1.00/01,0017) and ThermoFisher Scientific/Czechoslovak Microscopy Society scholarship (2017).

Brno 20/9/2020
.....


.....
author's signature

Contents

Contribution of the thesis	15
Introduction	16
I State of the art	17
1 Introduction to scanning (transmission) electron microscopy	18
2 Types of information in electron microscope	20
2.1 Emitted and deflected electrons	22
2.1.1 Secondary electrons (SE)	22
2.1.2 Back-scattered electrons (BSE)	23
2.1.3 Auger electrons (AE)	24
2.2 Transmitted electrons	25
2.2.1 Elastically scattered electrons	25
2.2.2 Inelastically scattered electrons	26
2.2.3 Multiply scattered electrons	27
2.3 Emitted photons	27
2.3.1 Cathodoluminescence (CL)	27
2.3.2 Characteristic X-rays	27
2.4 Generation of electron-hole pairs	29
3 Monte Carlo simulation of electron/sample interaction	30
3.1 Principle	30
3.1.1 Rutherford cross-section	31
3.1.2 Mott cross-section	32
3.1.3 ELSEPA based cross-section	33
3.2 Simulation software	33
3.3 Processing software for quantitative STEM	37
II Quantitative imaging	39
4 Quantitative STEM imaging	40
4.1 History	41
4.2 Principle	42
4.3 Application area	44
4.3.1 Annular STEM detector	44
4.3.2 Pixelated STEM detector	45
4.4 From qualitative to quantitative imaging	46
4.5 Density-thickness dualism	48

5	Quantitative BSE imaging	49
5.1	Principle	49
5.2	Calibration methods	49
5.3	Application area	51
III	Results	52
6	Motivation & research strategy	53
7	Quantitative imaging using scintillator based STEM detector	56
8	Quantitative imaging using semiconductor annular STEM detector	59
8.1	Calibration of STEM detector and primary beam current stability	59
8.2	Determining the accuracy of qSTEM	60
8.3	Influence of out-of-axis-detector	62
8.4	Application: Beam induced mass-loss of embedding epoxy resin	64
9	Quantitative imaging using pixelated STEM detector	69
9.1	Application: Thickness mapping of polymer blend PMMA/PS	70
10	Quantitative imaging using BSE detector	71
10.1	Application: Surface oxidation and thin coating thickness on substrates	72
11	Correlation of various signals in SEM	75
11.1	EDX-SEM: Analysis of ancient dental calculus	76
11.2	EDX-STEM: Characterisation of urban aerosol pollution	77
11.3	EDX-STEM: Selenium nanonutrients for fish	78
11.4	CL-STEM: Carboxylated nanodiamonds in THP-1 cells	79
11.5	EDX-CL-STEM: TiO ₂ nanoparticles distribution in mice organs	80
IV	Conclusion	82
	Bibliography	85
	List of abbreviations	100
V	Annexes	
A	List of all results	
A.1	Articles in journals with IF	
A.2	Articles in journals without IF	
A.3	Book section	
A.4	Conference abstracts	

B Referred full texts

- B.1 Quantitative STEM imaging of electron beam induced mass loss of epoxy resin sections
- B.2 4D-qSTEM-SRIP: calibration-less local thickness estimation of amorphous samples
- B.3 Nanoscale estimation of coating thickness on substrates via standard less BSE detector calibration
- B.4 The application of scanning electron microscopy with energy-dispersive X-Ray Spectroscopy (SEM-EDX) in ancient dental calculus for the reconstruction of human habits
- B.5 Size-segregated urban aerosol characterization by electron microscopy and dynamic light scattering and influence of sample preparation
- B.6 Application of advanced microscopic methods to study the interaction of carboxylated fluorescent nanodiamonds with membrane structures in THP-1 cells: Activation of inflammasome NLRP3 as the result of lysosome destabilisation

C Industrial designs

- C.1 Cryo-SEM holder for imaging of thin samples in the transmission mode with elemental and cathodoluminescence analysis
- C.2 Cryo-SEM holder and anticontaminator system for cathodoluminescence analysis in SEM at very low temperatures

List of Figures

1.1	Schematic comparing of the light microscope, transmission and scanning electron microscopes. Taken from [1].	18
2.1	(A) Signals generated in area of electron beam interaction with thin sample. (B) Schematic drawing of interaction volume. Redrawn from [2].	20
2.2	Monte Carlo simulations of electron trajectories in carbon sample with a density of 2.6 g/cm^3 for primary electron energies of 30, 15, 5 and 1 keV, respectively. Computed in CASINO 2.4.8.1 [3].	21
2.3	Schematic energy spectrum of emitted electrons consisting of secondary electrons (SE) with energy $\leq 50 \text{ eV}$, back-scattered electrons (BSE) with energy $> 50 \text{ eV}$, peaks of Auger electrons (AE) and low-loss electrons (LLE) with primary beam energy minus losses of a few hundreds of eV. Taken from [4].	22
2.4	(A) Different sources of SE in a vacuum chamber. (B) Distribution of different SE and their blurring effect. (C) Escape volume of SE is higher at the edges – they are brighter. Taken from [5].	23
2.5	Back-scattering coefficient η as a function of electron energy E for different elements (A) and atomic number Z for $E = 1, 5$ and 20 keV (B). Taken from [6].	24
3.1	Sequence of scattering processes in a Monte Carlo simulation with $s_n =$ free path lengths, $x_n, y_n, z_n =$ coordinates of electron at the n th collision, Θ_n and $X_n =$ scattering and azimuth angles after the n th collision. Taken from [4].	30
4.1	STEM detector calibration images. (A-B) Full and blanked beam image of the BF segment. (C-D) Full and blanked beam image of part of the HAADF segment. All images are taken with the same imaging conditions as a sample. One single change is in magnification (high $\rightarrow 48\times$).	43
4.2	Principle of qSTEM. Electrons scattered by a sample are captured by the detector with known detection angles. The intensity of detected signal normalised accordingly to calibration images (yellow scan shows signal in blue line due to the signal range in green) carries information about mass/thickness of a sample. The resulting thickness is determined by the MC simulation.	43
4.3	Comparison of annular and pixelated STEM detector. (A) The shown annular STEM detector can capture simultaneously up to three images, with given detection angles, describing electron scattering in a sample (BF, ADF, HAADF). (B) 2D-STEM detector captures full scattering pattern for each beam position and creates 4D dataset for further processing.	44
4.4	Monte Carlo simulation signal space of latex in BF (A) and HAADF (B). Notice the inverted signal axes. The used density of 1.05 g/cm^3 is highlighted in red. Capturing angles are 0-34 mrad for BF and 167-637 mrad for HAADF.	47
4.5	Geometrical body used for MC simulation of different thicknesses by performing single line scan (CASINOv 3.3.0.4). Supporting carbon layer is blue and simulated sample is green. The wedge angle is $\alpha = 5^\circ$. Local sample thickness is computed from the known beam position and the angle.	48

5.1	Principle of signal change in qBSE imaging. (A) Gold 5 nm; nearly all electrons penetrate the layer and scatter in the substrate but BSE coefficient is higher than in the case of pure substrate. (B) Gold 15 nm; a significant part of the electrons is back-scattered in gold layer and do not penetrate into the substrate. (C) Gold 30 nm; nearly all BSE are emitted from the gold layer – the accuracy of the method is decreasing. (D) Gold 50 nm; all BSE are emitted from the gold layer, there is no difference between the thick layer and a bulk – it is upper detection limit. All simulations were computed in CASINOv 2.48 (beam energy 5 keV, Mott cross-section).	50
6.1	The main instrumentation used in a project: (A) SEM Magellan 400L, FEI; (B) FIB-SEM Helios G4 HP, ThermoFisher Scientific; (C) SEM JSM 6700F, JEOL . . .	55
7.1	Model of two inch scintillator based STEM detector.	56
7.2	(A) Time dependence of beam and emission current after flash. (B) Long term ratio of condenser aperture (CA) and Farraday cup (FC) measured currents. . .	57
7.3	Test sample of latex nanospheres with diameter from 10 up to 400 nm imaged by home-made STEM detector in low magnification mode.	57
7.4	Latex nanospheres with a diameter around 400 nm captured by the home-made STEM detector in high-magnification mode.	58
7.5	Increasing of maximum magnification by external scanning unit.	58
8.1	Schematic drawing of individual STEM III detector segments layout.	59
8.2	Primary beam stability with a nominal probe current of 1.6 pA in the time range of (A) 120 s and (B) 3000 s.	60
8.3	Latex nanosphere images captured simultaneously in BF (A) and HAADF (B). (C) Calculation of the rotationally averaged signal (detected sphere – green, control of the integrity of the particle – red lines and detected centre – enlarged area; the distance of individual pixels from the detected nanosphere centre). Bar 200 nm.	60
8.4	Thickness of the sample estimated by quantitative STEM imaging in two different detector segments together with their mean and geometry. The problematic areas are highlighted in enlarged sections (low thickness region in blue and high thickness region in red).	61
8.5	Relative qSTEM thickness error dependency on the distance from the centre of the nanosphere (A) and on the local geometrical thickness (B).	62
8.6	The results of MC simulation. (A) Histogram of electrons impacted the STEM detector plane according to distance from the optical axis. (B) Control of the azimuth angle uniformity of simulated electrons.	63
8.7	Change of BF (A) and HAADF (B) signal in considering detector-axis deviation. (C) Analysis of STEM detector deviations from the optical axis. Circles show the position of BF segment in case of the STEM detector on the optical axis (blue) and actual position (red). The measured deviation is highlighted in graphs (A, B) by the magenta line.	63
8.8	Scheme of mass loss estimation by qSTEM.	65
8.9	The normalised BF signals (A) and recalculated relative mass (B) dependencies of the total irradiation dose on slices of various thicknesses with and without staining. Data were recorded on the second day. Taken from [7].	67

8.10	(A) The normalised BF signals of 60 and 150 nm slices cleaned for 20 s. (B) Relative mass-loss dependencies on the total irradiation dose for 60 and 150 nm slices. (C) The normalised bright-field signals of 30 nm slices cleaned for different times. All images were recorded on the seventh day from cutting. Figures A and B are taken from [8].	68
8.11	The normalised BF signal (A) and relative mass-loss (B) dependencies of the 60 nm sections on the total irradiation dose for 60 nm slices at different temperatures. Taken from [9].	68
9.1	Principle of 4D-qSTEM. (A) Test sample of a latex nanosphere with radius r is irradiated by scanning electron beam. Scattering patterns are captured independently for all beam positions. (B) Rotation sum of captured scattering pattern is computed and local dependency of the primary electron fraction is plotted accordingly to the scattering angle. (C) Simulated scattering angle dependency for several sample thicknesses. Note that the position of the peak is moving to the higher angles with increasing thickness.	69
9.2	(A) Test sample of a latex nanosphere with a diameter of 575 nm with the measured point in the middle of the sphere. (B) Comparison of scattering angle dependencies from the measured point and simulation for 555 nm thick layer of latex. Position of both peaks is at 61 mrad.	70
10.1	Diagram of energy-dependent calibration of STEM detector (A) and BSE detector (B). Calibration of the BSE detector is performed by primary beam reflection on the biased sample instead of direct imaging used in case of the STEM detector. Taken from [10].	71
10.2	Dependence of pixel intensity of the inner dark field segment DF1 of the STEM detector (A) and inner BSE detector segment A (B) on beam energy. Contrast/brightness settings were the same for the individual detectors across all energies. Taken from [10].	72
10.3	Results of qBSE imaging. (A) Comparison of measured and nominal thicknesses. Most of the measurements show an error lower than 1.2 nm. (B) Comparison of measured and nominal thicknesses. Most of the measurements show an error lower than 20%. The blue \times mark shows a data point out of the used y-axis range. (C) Theoretical BSE signal captured by A segment in working distance of 4 mm for Cr, Mo and Au. The individual points show mean values of measured samples with its standard deviation and horizontal lines indicates the thickness assigned by qBSE imaging. The oxidised layer of Cr is highlighted by square marks. Taken from [11].	73
10.4	Results of qBSE thickness mapping of the Mo layer with a nominal thickness of 25 nm. (A) Data without filtering – high influence of noise. (B) The same data after 2D median filtration with window 5×5 . (C) The same data after 2D median filtration with window 50×50 . (D) Histogram of values from image part C. (E) Resulting map shows thicker region in the lower part of an investigated area. Each map has information about the size of filter window \square and mean estimated thickness \uparrow	74
11.1	Analysis of human ancient tartar. Confirmation of the hypothesis of tooth damage caused by repeated opening of cartridges with bullet and gunpowder. Based on [12].	76

11.2	Analysis of urban aerosol nanoparticles by EDX-S(T)EM. (A) SEM micrograph of various particles with their identification. (B) Agglomerate of iron nanoparticles with diameters ranging from 5 to 55 nm. (C) EDX spectrum of previous agglomerate. Adapted from [13].	77
11.3	The bright-field STEM image of selenium particles with nominal size of 120 nm (A), its EDX spectrum (B) and EDX map for selenium (C). Adapted from [14]. .	78
11.4	(A) CL spectrum of fluorescent nanodiamond measured in SEM and fluorescence spectrum (insert) of the same sample. (B) Detail of intracellular vesicle coated by fluorescent nanodiamonds visualized by TEM. (C) CL detail of fluorescent nanodiamond cluster associated with intracellular vesicle in THP-1 cell. Adapted from [15].	79
11.5	Correlative imaging of TiO ₂ nanoparticles inside lung mouse tissue. High-resolution BF-STEM images are supplemented with CL, EDX mapping and EDX spectral analysis of chosen clusters.	80
11.6	Proof of evidence of TiO ₂ inside mouse erythrocytes. CL spectrum of erythrocytes with TiO ₂ is a combination of TiO ₂ free erythrocytes and pure TiO ₂ powder. This is visible at peak at 430 nm and extension of the main peak to the lower wavelengths.	81

List of Tables

1.1	Comparison of wavelengths, mass increasing ratio and speed of electrons accordingly to beam energy used in SEM.	19
2.1	Energy loss of electron after collision with different atoms. Computed in MONCA [16].	26
2.2	Comparison of analytical techniques. Adapted from [17].	28
3.1	Comparison of main features of MC software. Redrawn from [18] and actualised.	33
4.1	Mean free path dependency on beam energy and type of a sample. Calculated in software MONCA [16].	41
8.1	Composition of possible variants of embedding epoxy resin EMbed 812 [19]. . . .	64

Listings

8.1	Start of simulation in software MONCA2	62
-----	--	----

Contribution of the thesis

The scientific contribution of this doctoral thesis is supported by 22 scientific publications in total. It consists of 7 publications in impacted journals of which 2 of them as the first author, 2 in non-impacted journals and 13 in conference proceedings and abstracts. Full list of results can be found in the annex A.

The core of the thesis are: analysis of accuracy and error sources of quantitative scanning transmission electron microscopy, application of quantitative scanning transmission electron microscopy in epoxy resin mass-loss study and the development of new and innovative methodologies/techniques for quantitative imaging using annular back-scattered electron and pixelated scanning transmission electron microscopy detectors, which were published in high-quality scientific journals.

The new approaches may be summarised in following points (full papers can be found in the annex B):

- Epoxy resin sensitivity depends on many conditions, optimal sample preparation and imaging settings may be found and used for suppression of real sample mass-loss caused by electron beam irradiation.
- The use of electron deflection on electron mirror solves a problem with back-scattered electron detector calibration which is situated sensitive side down and just under a pole-piece of final demagnifying lens in a vacuum chamber of a scanning electron microscope.
- The use of pixelated detector of transmitted electrons overcomes a problem with imperfect and drifting calibration values of classical intensity based quantitative scanning transmission electron microscopy technique.

Design activity and development of equipment is documented by two industrial designs, which were used in individual applications (full documentation in the annex C).

The educational contribution of the thesis is represented by author's co-teaching of the course Physical methods in anthropology (2019; Faculty of Science, Masaryk University), supervising one bachelor student, who successfully defended her work in 2017, consultations for one master student (2016) and reviewer of two bachelor students in 2018.

Contribution to the popularisation of science is in author's participation in lectures and excursions within the Brno Days of Electron Microscopy, the Week of Science and Technology and a few workshops within Strategy AV21 of the Czech Academy of Sciences.

Introduction

The classical imaging in the field of electron microscopy brings spatial distribution of imaged physical or chemical properties of a sample without exact information about the amount of this property. Nowadays, imaging carrying exact information about chosen quantity is becoming more common. Accordingly to this progression from qualitative to quantitative imaging, a wide group of techniques and methods has been developed in last decades.

This thesis deals with the possibilities of quantitative imaging in a scanning electron microscope (SEM). There are many combinations of techniques which give information about different chemical, physical or geometrical properties of investigated samples. The thesis describes signals emitted from a sample in theoretical way with main focus to transmitted and back-scattered electrons. The thesis deals further with application of more or less established quantitative techniques in wide spectrum of separate studies and own methodology development in quantitative back-scatter and calibration-less transmitted electron imaging. The result part is divided into five separate chapters according to their focus.

The first one specifies possibilities and problems connected with the development of scintillator based fully calibrated quantitative scanning transmission electron microscopy (quantitative STEM or qSTEM) detector and its practical using. The detection system is designed as resistant to beam current fluctuation with suppression of associated errors. The second one, deals with qSTEM imaging including detailed theory description and literature review. qSTEM measurements are used for estimation of EMBED 812 epoxy resin sensitivity to irradiation by the primary electron beam accordingly to various conditions. It is an application of established technique for studying a material, which degradation directly influences the quality of transmission electron microscopy (TEM) images of samples embedded in this type of resin. The third one, describes a new method for calibration of retractable back-scattered electron (BSE) detectors inside the microscope chamber. There are papers dealing with quantitative BSE imaging, but direct calibration of the detector to primary electron beam is bypassed by capturing the signal of a sample with known composition – it is standard based calibration. This thesis presents a standardless absolute calibration method, which describes a response of the detector to the electron beam energy and position of an impact. This part includes detailed theory description and literature review. The fourth one, presents options of 2D pixelated detectors in qSTEM. Thanks to this type of semiconductor detector, the STEM detector calibration, which is in case of classical qSTEM needed before each imaging session, is not necessary. The literature review is limited because only a few papers deals with this new area. The last one describes the published results of ordinary quantitative techniques. Those are applications of cathodoluminescence (CL) and energy dispersive X-ray spectroscopy (EDX or EDS) in correlation with a high-resolution images based on secondary electron (SE) imaging or scanning transmission electron microscopy.

The aim of this Ph.D. thesis is methodological development, design, construction and testing of equipment and techniques for quantitative imaging with subsequent proposal of calibration procedures in SEM. The developed methods and procedures are than used in a wide range of applications including the samples from both fields of life and material sciences.

Part I

State of the art

1 Introduction to scanning (transmission) electron microscopy

Scanning electron microscopy is as its name suggests system with the serial acquisition of information about an investigated sample. The principle of all SEM techniques is based on the interaction of a focused electron probe with a sample and capturing of the generated signal by the appropriate detector. This information is then related to the position of primary beam given by the scanning unit and stored as a 2D matrix (image). The image is created in a computer by colour scale assignment (the most often used is grayscale) and it is displayed on a computer screen. The advantage of this approach is the possibility to assign the measured values to the exact part of a sample and measure different physical properties and phenomena. Classical light microscopy (LM) or transmission electron microscopy creates a real image by a system of lenses on a screen or camera. However, as visible in Fig. 1.1, the SEM has no lenses behind the sample. By the use of transmitted electron detector under a sample the scanning transmission electron microscope is created. It can be dedicated STEM working under various beam energies or so called low-voltage STEM, which has its origin in SEM. Absence of lenses behind the sample brings an advantage in vacancy of sample caused chromatic lens aberration.

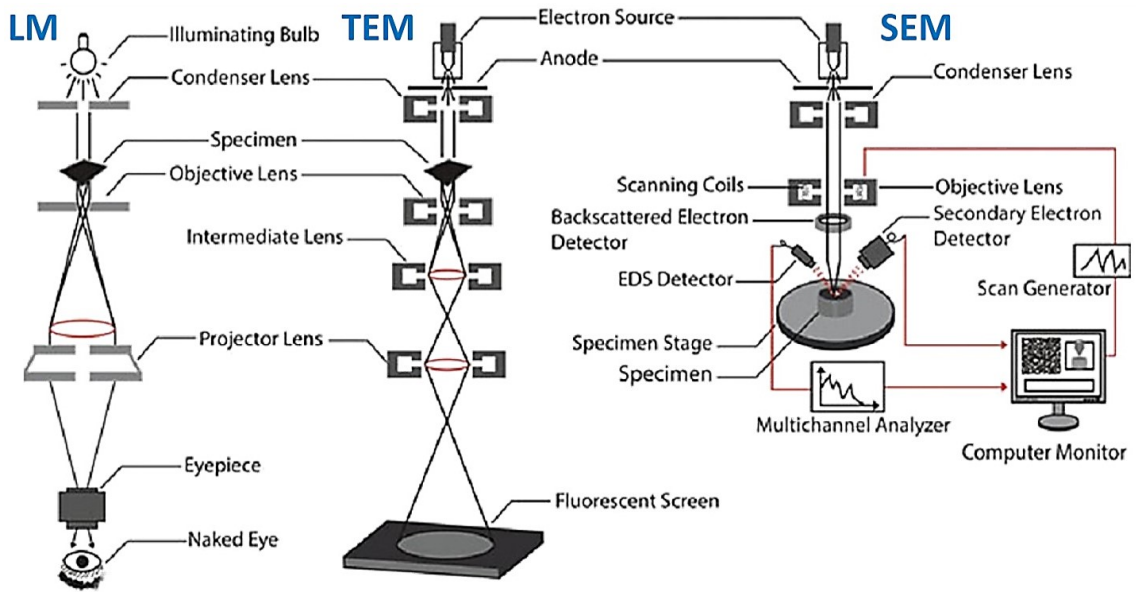


Fig. 1.1: Schematic comparing of the light microscope, transmission and scanning electron microscopes. Taken from [1].

The electrons have many convenient properties which make them suitable for use in microscopy. They have negative charge – they may be influenced by electric and magnetic fields. They are much lighter compared to protons (charged particles as well) and so sample destruction is much lower ($m_e = 9.109 \times 10^{-31}$ kg, $m_p = 1.672 \times 10^{-27}$ kg). They have accordingly to de Broglie equation ($\lambda = \frac{h}{p}$, where λ is the wavelength, h the Plack constant and p electron momentum) the wavelength much shorter than visible light, which enables to achieve much higher resolution. The wavelength of electron is given by

$$\lambda = \frac{h}{\sqrt{2m_e eU(1 + \frac{eU}{2m_e c^2})}}$$

where e is the electron charge (-1.602×10^{-19} C), U the acceleration voltage and c the speed of light. Properties of electrons with typical SEM energies are shown in Tab. 1.1.

Tab. 1.1: Comparison of wavelengths, mass increasing ratio and speed of electrons accordingly to beam energy used in SEM.

E [eV]	λ[pm]	m/m_e	v/c
100	122.6	1	0.019
1,000	38.8	1.012	0.063
10,000	12.2	1.019	0.195
20,000	8.6	1.040	0.273
30,000	7.0	1.059	0.328

The electron lenses cannot be constructed as reflective lenses used for light because of high scattering of electrons in condensed matter – it is necessary to avoid the interaction of electrons with other atoms during probe formation. There are two types of electron lenses based on electric or magnetic fields. The lenses are used for the creation of focused electron probe on the surface of a sample by crossover demagnification (for wolfram filament with crossover around $50 \mu\text{m}$ is contraction to 10 nm probe around $5,000 \times$, for field emission gun than only $10\text{-}100 \times$). The real magnification is then just a ratio between probe diameter and computer screen. Since it is possible to change the magnification value while an image is scaled on the screen, a more precise description is the use of image size in $\text{nm}/\mu\text{m}$ or pixel size. Amount of signal and its quality strongly depends on the time which the beam spends at every individual place. There are two opposing settings: high frame rate with small dwell time – higher noise, lower signal quality, lower beam damage or low frame rate with long dwell time producing high-quality data with low noise but influenced by sample drift, charging etc. Influence of those defects can be suppressed by different scanning strategies (line skipping, non-continuous area imaging), or imaging settings (line and frame integration, averaging, drift correction). In general, it is necessary to find and use different setting accordingly to the type of investigated sample and chosen imaging or analytical technique.

Pros: The SEM provides many types of analyses for a huge variety of samples, which can be in sizes from nanoparticles mounted on TEM grid up to samples with a size of tens of centimetres (depending on the type of specimen chamber and stage). The imaging is fast and with high focus depth (the probe semiangle is very small), which allows big area imaging (in case of using post-acquisition images merging). The maximum resolution can be in tenths of nanometers but strongly depends on sample and imaging conditions. The samples may be studied at different conditions such as temperature (from few tens of K up to more than $1,000 \text{ K}$), pressure and atmosphere (targeted gas admission in case of environmental SEM) or mechanic stress. The samples can be dry for investigation in a standard vacuum chamber, wet in case of environmental SEM or frozen in cryo-SEM. It is possible to use a variety of analytical detectors. It may be supplemented by other techniques, such as Raman spectroscopy or atomic force microscopy (AFM), to perform correlative measurements.

Cons: The main limitations are the need for solid samples because of vacuum in a specimen chamber and problems with imaging of non-conductive samples (can be solved by conductive coating, beam energy lowering or using of environmental SEM).

2 Types of information in electron microscope

During the interaction of the primary electron beam with a sample huge amount of different signals are emitted from the sample. Those signals carry information about different physical and chemical properties of the investigated sample. Schematic drawing of the signal "ZOO" of electrons, photons, and plasmons is shown in Fig. 2.1 A. The imaging has to be understood in case of SEM as assessing of information from a detector to the position of a primary electron beam impact on a sample (interaction volume is schematically drawn in Fig. 2.1 B). Such 2D distribution of the captured signal is in the most cases modulated by grey levels from black to white. For easier interpretation and enhancement of the results, a pseudo-colouring can be applied. An image, where modulation of the signal does not have exact information about the physics or chemical property, is called qualitative.

For example, the most common imaging technique in SEM gives information about the yield of secondary electrons compared to the position of the scanned sample's surface, although without the amount in SI units. Compared to that, the quantitative imaging brings well-defined physical/chemical information about investigated sample: BSE – Z contrast, CL – wavelength of emitted light, polarisation or its angular distribution, EDX and WDX (wavelength dispersive X-ray spectroscopy) – the X-ray photon energy, Auger electron spectroscopy (AES) – the energy of emitted electrons or EELS (electron energy loss spectroscopy) – the energy loss of primary electrons.

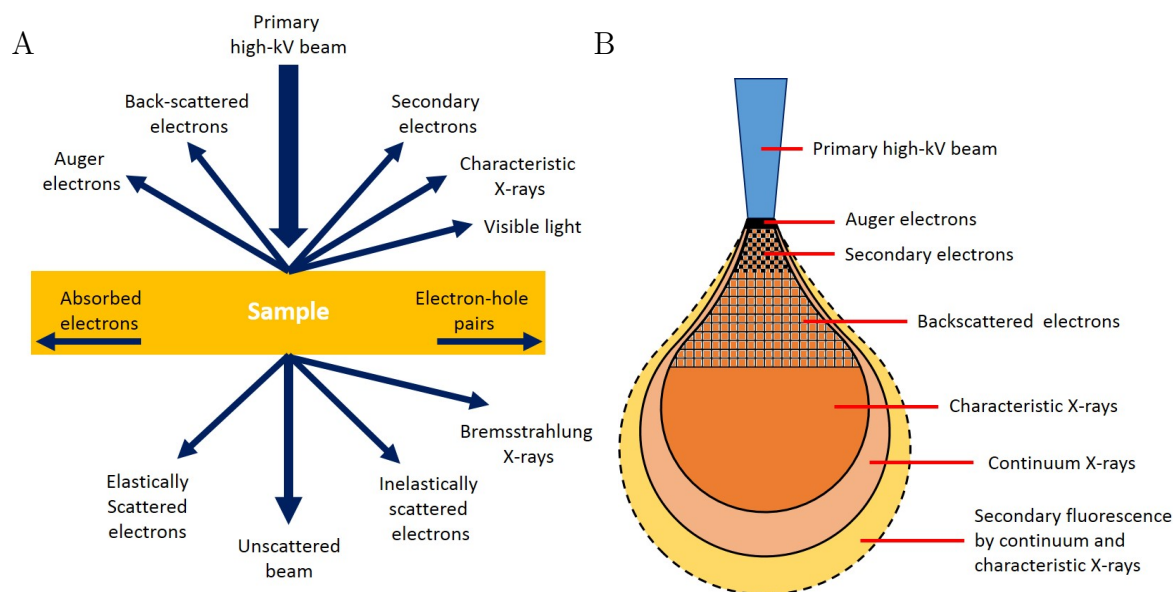


Fig. 2.1: (A) Signals generated in area of electron beam interaction with thin sample. (B) Schematic drawing of interaction volume. Redrawn from [2].

The penetration depth depends on sample thickness, elemental composition, density and beam energy. It is possible to catch transmitted electrons which go through the sample in case of electron transparent samples by different techniques:

- integral signal in detection range of angles (the angle depends on working distance – WD – and size of detector)
 - bright field (BF)

- annular bright field (ABF)
- dark field (DF)
- high-angle annular dark field (HAADF)
- diffraction/scattering pattern on 2D pixel detector
- electron energy loss spectroscopy

The information which is emitted from a sample is highly dependent on primary beam energy and its corresponding interaction volume. Most of the SEMs allow to adjust the beam energy from a few hundred eV up to 30 keV with a consequential change of its physical properties. The comparison of penetration depth for carbon is shown in Fig. 2.2. The change of penetrability plays an important role in high-quality surface imaging where the use of low-energy beam enhances the resolution – the signal is emitted from a smaller area. On the other hand, the variation in beam energy can be used for capturing BSE images from different depths under the sample surface as used in VolumeScope™, which is based on multi-energy deconvolution of BSE images taken at different beam energies [20].

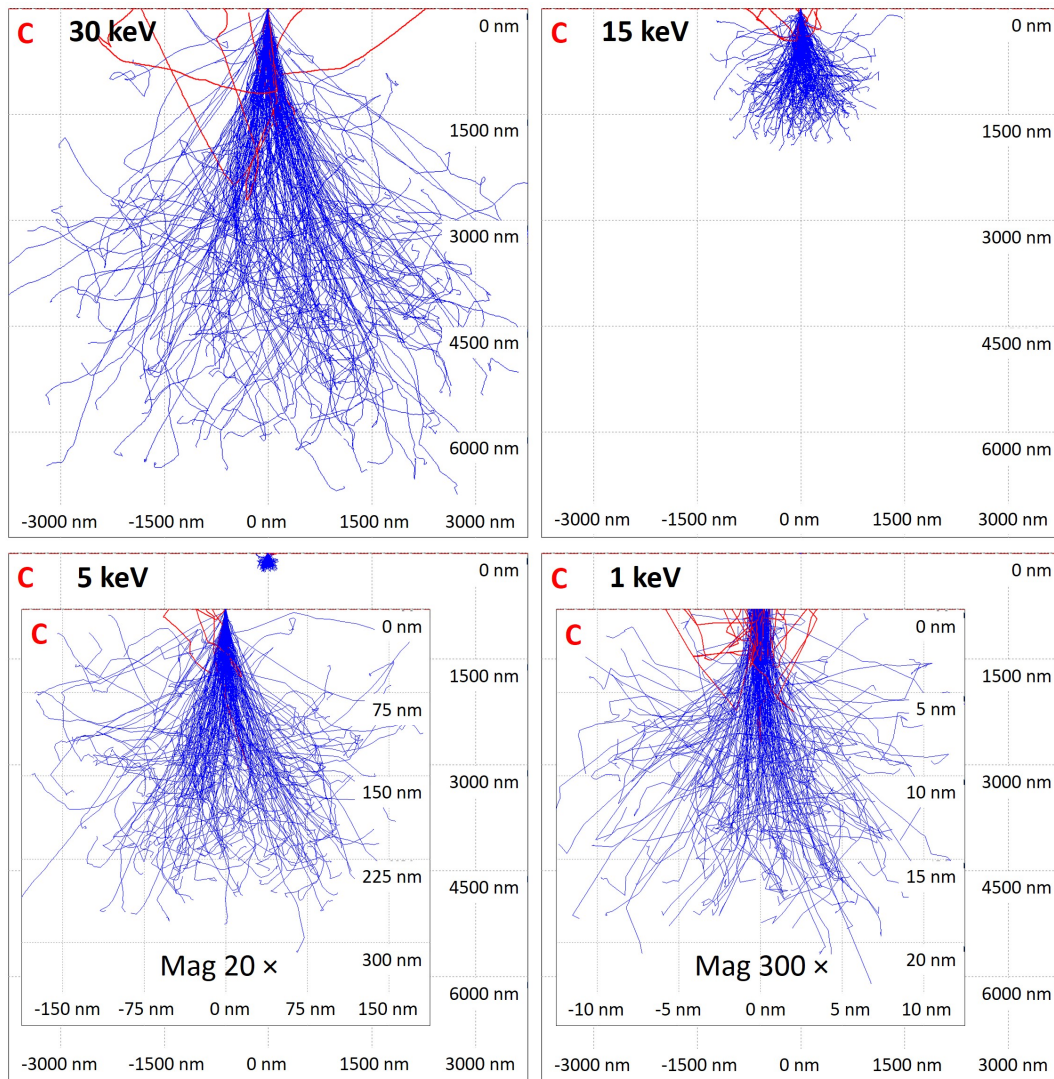


Fig. 2.2: Monte Carlo simulations of electron trajectories in carbon sample with a density of 2.6 g/cm^3 for primary electron energies of 30, 15, 5 and 1 keV, respectively. Computed in CASINO 2.4.8.1 [3].

The following sections bring an overview of signals emitted in an SEM, highlighting important features used in the next parts of the thesis. The detailed description of physics behind the signals, their generation, properties, propagation and detection can be found in general books about electron microscopy like [4, 21, 22], partially focused on X-rays [1, 23] or cathodoluminescence [24] or specialised books about cathodoluminescence [25], Auger electron spectroscopy [26], STEM and electron energy loss spectroscopy [27] or electron back-scatter diffraction [28].

2.1 Emitted and deflected electrons

The signal electrons which are emitted from sample during interaction of primary electron beam with sample can be divided into several types according to their energy and physical principle of generation. The possible energy range is theoretically from 0 up to the primary beam energy (schematic energy spectrum is shown in Fig. 2.3). There is no exact dividing border between the SE and BSE. By convention is given that electrons with energy lower than 50 eV are SE and electrons with higher energy are BSE. The subgroup of Auger electrons is described in more detail in Subsection 2.1.3: Auger electrons.

The broad spectrum of BSE between SE and the primary electron energy is caused by the deceleration of electrons that have suffered multiple energy losses and undergone multiple scattering through large angles [4]. Different types of electrons are captured by different types of detectors mounted both in the microscope chamber and inside the electron column. The universal energy analyser attachment for all emitted electrons is described in the work of Khursheed [29].

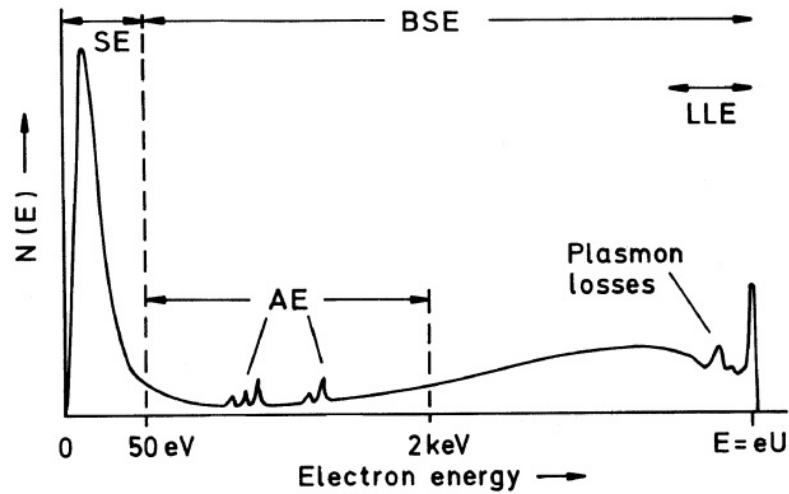


Fig. 2.3: Schematic energy spectrum of emitted electrons consisting of secondary electrons (SE) with energy ≤ 50 eV, back-scattered electrons (BSE) with energy > 50 eV, peaks of Auger electrons (AE) and low-loss electrons (LLE) with primary beam energy minus losses of a few hundreds of eV. Taken from [4].

2.1.1 Secondary electrons (SE)

The energy of impacting primary electron beam is changed to the potential and kinetic energy of valence electrons which enables the weakly bounded electrons to leave a sample. The electrons are moving through a sample, interacting with other electrons and decreasing their energy.

The mean free path is in range from several to tens of nm. Thanks to that only electrons from the surface area of the sample are emitted and so provide excellent surface topography resolution [5, 30]. The most probable energy is in the range from 2 to 5 eV [4].

The final resolution is lowered by generation of parasitic SE (after impact of BSE) in other areas than the area of the impact of the primary electron beam (Fig. 2.4 A) – that results in higher background signal and noise (Fig. 2.4 B). The SE signal is dependent on the volume of a sample which is in lesser distance from the surface than escape depth d . It is called "the edge effect", where edges of the sample generate a much higher signal. The effect is demonstrated in graphical form in Fig. 2.4 C.

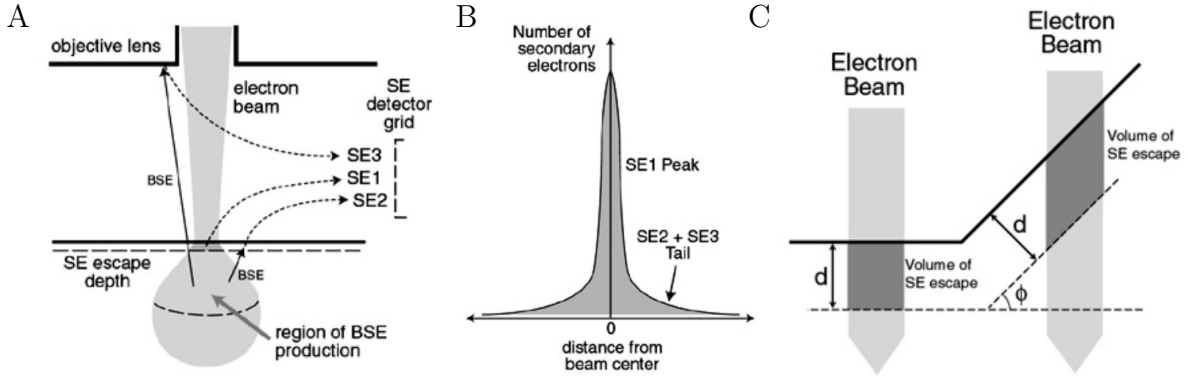


Fig. 2.4: (A) Different sources of SE in a vacuum chamber. (B) Distribution of different SE and their blurring effect. (C) Escape volume of SE is higher at the edges – they are brighter. Taken from [5].

2.1.2 Back-scattered electrons (BSE)

BSE are originally primary electrons more or less elastically scattered back towards the electron column (they are emitted from a sample with a scattering angle higher than $\pi/2$ rad). This change of trajectory can be caused by single or multiple scattering events which may be individually lower than $\pi/2$ rad. The small interchange of energy among interacting particles in case of electron – atomic nucleus interaction (described in detail in Section 2.2.1.) causes that the most of BSE have energy just slightly lower than the energy of the primary beam [5].

The back-scattering coefficient (ratio of the number of the back-scattered electrons to the total number of the incident electrons) increases monotonously with increasing atomic number Z for primary electron energies $E > 5$ keV. The dependency of BSE coefficient on Z for energy below 5 keV is more complicated and it depends on both beam energy and Z as shown in Fig. 2.5 A, B. For example, the BSE coefficient is decreasing with increasing beam energy for Al, nearly constant in case of Cu and increasing in case of Au [31]. The dependency on Z carries information about the elemental composition of a sample. Thanks to higher energy, the BSE can be emitted from a deeper part of a sample compared to SE and the larger interaction volume implies lower spatial resolution in resulting image. However, low-loss electrons (LLE) from the elastic peak within an energy window around 10-100 eV below the primary energy can leave the specimen only from a thin surface layer, comparable with that of SE and AE [4].

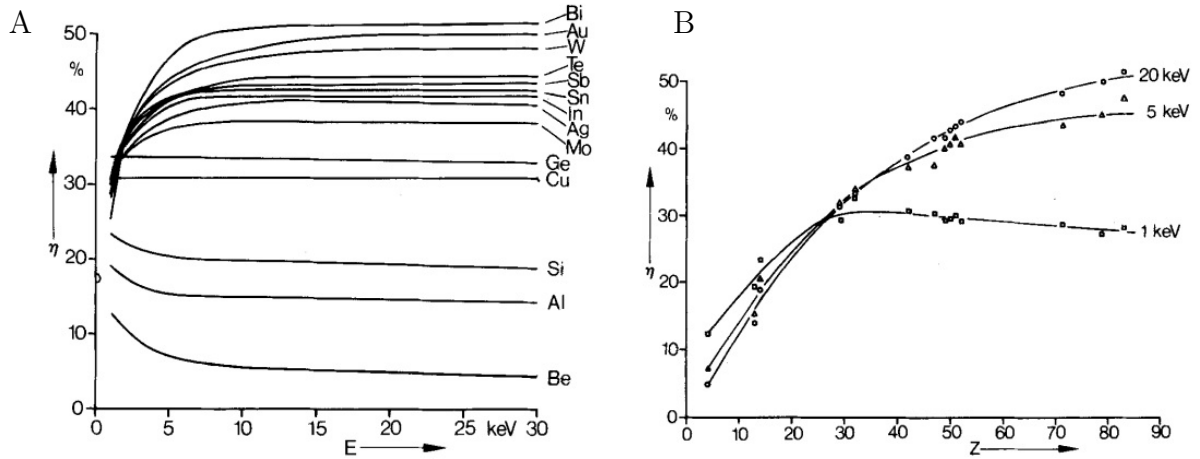


Fig. 2.5: Back-scattering coefficient η as a function of electron energy E for different elements (A) and atomic number Z for $E = 1, 5$ and 20 keV (B). Taken from [6].

"The BSE coefficient also depends on the relative orientation of the incident electron beam and the lattice planes. A plane incident electron wave propagates inside the crystal as a Bloch-wave field, which shows anomalous absorption or transmission depending on the angle of incidence relative to the lattice planes. The resulting orientation anisotropy of the back-scattering coefficient is very sensitive to small crystal tilts and causes differences in the back-scattering coefficient of the order of 1 - 10 %. This allows differently oriented grains in polycrystalline material to be imaged by crystal orientation or channelling contrast [4]."

Back-scatter electron imaging

BSE image is a combination of topographic and chemical contrast. In case of the flat specimen where the topographic contrast is minimised, the regions of higher average Z emit more BSE compared to areas with lower average Z . The change of contrast may be used for distribution estimation of phases with different average Z and can be considered as chemical contrast [32].

Electron back-scatter diffraction (EBSD)

EBSD is a technique for visualisation of the local crystal structure and orientation on the specimen surface. The elastically scattered BSE (reflected by coherent Bragg scattering) are collected on dedicated EBSD detector where electron back-scatter diffraction patterns made up of Kikuchi bands are formed [28].

2.1.3 Auger electrons (AE)

Auger electrons are very similar to characteristic X-rays. Emission of AE occurs when an electron from the inner atomic shell is ionised and the corresponding amount of energy is released when the vacancy is filled by an electron from outer shell. The amount of released energy can be emitted as X-ray photon or it can be transferred to another electron which leaves the specimen with appropriate kinetic energy – the Auger electron [4].

Auger electron spectroscopy (AES)

AES is a surface sensitive analytical method where an electron beam is used to excite the electronic states of a solid. When the atoms decay from the excited electronic state, Auger electrons with characteristic energies are emitted, carrying band structure information [33]. The AE energy varies from a few tens of eV for light element KLL electrons to 2,000 eV for heavy element MNN electrons. The captured electron energy spectrum is a superposition of AE peaks with a continuum electron energy spectrum (AE peaks can be resolved by double differentiation). The AE lose their energy during their path through a solid so the characteristic energy of the AE is preserved only from the first few monolayers ($\sim 10 \text{ \AA}$) of a sample. The sensitivity of the method increases with the atomic number from about 10 at% (atomic percent) for lithium to 0.01 at% for uranium (AE are not emitted by helium and hydrogen thanks to their electron structure). AES can detect the presence of specific atoms but for quantification of the results it needs calibration standards with a composition close to the investigated sample. The accuracy is then $\sim 10 \%$ [34].

2.2 Transmitted electrons

Transmitted electrons are primary beam electrons which have passed through a sample. The amount of transmitted electrons is dependent on the sample (thickness, density, composition) and beam energy (electrons with higher energy have higher penetrability). During travel of an electron through a sample, different scattering events may occur.

2.2.1 Elastically scattered electrons

Elastic scattering is caused by electrical interaction of a negatively charged electron with a positively charged nucleus. From definition of the elastic scattering the energy transfer between electron and nucleus should be zero (provided that the much heavier nucleus remains at rest). Unfortunately, each interaction of an electron with atomic nucleus causes an energy loss of the electron. It is possible to determine the amount of transferred energy as

$$\Delta E = \frac{4mM}{(m+M)^2} \cdot E \approx \frac{4m}{M} \cdot E$$

where m is mass of electron, M the mass of nucleus ($M \approx 1836 \cdot m \cdot A$), A the atomic mass number and E is initial electron energy. Results for chosen elements are shown in Tab. 2.1. As follows from the table, the energy transfer is a few tenth of percent with the highest values in case of collisions with hydrogen atoms.

This type of electron scattering is used in several imaging modes like STEM, quantitative STEM and ptychography (reconstruction using pixelated STEM detectors; the method is commercially available in π box the Phasefocus Virtual Lens[®] Reconstruction Engine (Phasefocus, UK) [35]).

Tab. 2.1: Energy loss of electron after collision with different atoms. Computed in MONCA [16].

Element	A	Beam energy [keV]					Change [%]
		30	10	5	2	0.5	
Change [eV]						Change [%]	
H	1.008	64.841	21.614	10.807	4.323	1.081	0.2162
C	12.01	5.442	1.814	0.907	0.363	0.091	0.0182
Si	28.09	2.327	0.776	0.388	0.155	0.039	0.0078
Fe	55.85	1.170	0.390	0.195	0.078	0.020	0.0039
Sn	118.71	0.551	0.184	0.092	0.037	0.009	0.0018
Au	196.97	0.332	0.111	0.055	0.022	0.006	0.0012
Pb	207.20	0.315	0.105	0.053	0.021	0.005	0.0011

2.2.2 Inelastically scattered electrons

Inelastic scattering of electrons inside a sample changes their energy. This loss of energy is associated with an energy transfer to the electron cloud of atoms in the sample. This can be detected by energy filters used for separation of electrons according to their energy.

Electron energy loss spectroscopy

The method is developed in TEM much more than in SEM. Transmission EELS attachment for SEM is described in [36] and commercially available in SEM SU9000 (Hitachi, Japan) [37, 38]. The classical methodology uses a post-column EELS spectrometer after the normal electron optics, which uses a magnetic prism to deflect the electrons according to their energy. It allows capturing a spectrum with typical energy resolution of 0.5-1 eV. For high spatial resolution, a STEM mode is used for the creation of 4D datasets consisting of individual spectra in all pixels. Section of such hyperspectral data is the image of a sample at selected electron energy / energy loss. Energy resolution < 0.1 eV can be achieved by the use of monochromators, which reduce the impact of primary beam energy variation. Energy losses of a full range of inelastic scattering mechanisms (plasmon and phonon scattering, SE emission, fine details of an atomic bonding in different crystal structures) are linked to specific values [32]. Electron energy loss spectroscopy is analytical method showing spectrum of unoccupied density of electron states and provides information about wide range of sample properties:

- chemical composition – especially for light elements including B, C, N and O (in case of EDX the X-ray absorption is problematic)
- element specific atomic density (nm^{-3})
- chemical phases (via MLLS*-fit)
- oxidation states, Valence states
- electronic structure (band-structure)
- optical properties
- magnetic properties
- sample thickness. [17]

2.2.3 Multiply scattered electrons

Even in very thin samples, multiple scattering occurs, when elastic and inelastic scattering events are chained behind each other. Distance between the individual events is given by mean free path of an electron in a matter. Electron energy is decreasing by undergoing the inelastic scattering and full cascade of events is running. Detailed description of individual events, empiric equations and Monte Carlo simulation principle can be found in Chapter 3 and Section 4.4.

2.3 Emitted photons

As a result of inelastic electron scattering absorbed energy may be emitted in the form of photons with a specific energy. It is possible to divide them according to their energy and place of origin into two groups which differ in carried information and principle of detection.

2.3.1 Cathodoluminescence (CL)

Cathodoluminescence is an emission of ultraviolet, visible or infrared light from a sample during an impact of a primary electron beam. The light is usually collected by a detector with a high capturing angle (optical fibres or mirror of ellipsoidal or parabolic shape). Then the light is transferred through light guide outside the microscopy chamber through a monochromator to photomultiplier, CCD (charge-coupled device) or CMOS (complementary metal-oxide semiconductor) camera. The parallel acquisition of spectrum significantly reduces time when a sample is irradiated by the electron beam – it is highly important for beam sensitive samples. The crucial point is the setting of a sample into a focal point of the collecting mirror with given focal distance. Even small deviation can, in case of low yield samples, significantly suppress the captured signal.

The lateral resolution of CL is strongly influenced by interaction volume of electrons in a sample, which means that it is beam energy dependent. This applies to SEM, the CL-STEM has higher lateral resolution caused by the reduced thickness of a sample combined with the high energy of electrons. The electrons focused to small probe go through the sample before their spreading. The resulting resolution is about one order of magnitude better than in SEM. Another possibility, how to overcome intrinsic resolution limitation, is a combination of AFM and SEM. The scanning near-field cathodoluminescence microscopy (SNCLM) use light excitation by electron beam but it is collected directly above the recombination centres by the scanning near-field optical microscopy (SNOM) probe with a probe-sample distance of a few nanometers [39].

2.3.2 Characteristic X-rays

The primary electron beam energy has to be high enough for excitation of the elements of interest. The basic rule is $E_{\text{beam}} > 2E_{\text{X-ray}}$. It brings complication in high-resolution analysis because the spatial resolution of the method is limited by interaction volume of primary electrons. This limitation may be overcome by analysis of thin samples, where most of the electrons are transmitted through the sample without creating full interaction volume pear. Characteristic X-rays can be emitted only from the depth where the energy of electron beam is still higher than the ionisation energy of electrons in the inner shell of surrounding atoms. The emitted X-ray can be absorbed by another element with following secondary X-ray emission or X-ray fluorescence. Thanks to that, the X-ray fluorescence range can exceed the electron range [4].

Energy-dispersive X-ray spectroscopy (EDX)

EDX or EDS is an analytical technique with the parallel acquisition of characteristic X-ray photons. This method is appropriate for elements in a concentration higher than 0.1 % (detection limit is around 500 ppm) and in middle Z region.

Wavelength-dispersive X-ray spectroscopy (WDX)

WDX or WDS is an analytical technique with the serial acquisition of characteristic X-ray photons with chosen wavelength. WDX compared to EDX has much higher spectral resolution but much slower acquisition speed. It is suitable for light elements and low concentrations down to 10 ppm.

Micro X-ray Fluorescence (μ XRF)

μ XRF is an analytical technique with its X-ray source, but it can be mounted on an SEM chamber and used for sample characterisation. μ XRF is suitable for heavy elements with very good detection limit around 10 ppm. The disadvantage is higher interaction volume (compared to electron primary beam interaction volume) and corresponding lower spacial resolution.

It is impossible to decide which method of EDX, WDS, EELS and CL is the best. They have a different spectral range that they can capture, different energy resolution, sample requirements and application areas. The main characteristics are compared in Tab. 2.2.

Tab. 2.2: Comparison of analytical techniques. Adapted from [17].

	Spectral range [eV]	Energy resolution [eV]
EDX	300 - 40,000	125.0 ^a
WDS	1.47 - 17,900	2.0 ^b
EELS	0 - 2,500	0.7 ^c
CL	1.55 - 3.1	0.002

^a Energy resolution of windowless detector is around 30 eV [40].

^b Energy range depends on used diffractor; maximum range of two different types is shown [41].

^c Energy resolution of HERMES microscope (Nion, USA) is 0.0062 eV [42, 43].

2.4 Generation of electron-hole pairs

Impacting electrons in semiconductors can generate electron-hole pairs in the amount of a few thousand per incident electron and as consequence, the resulting electrical current may be measured after applying external voltage [4].

Electron beam-induced current (EBIC)

"In the depletion layer of a p-n junction, the strong electric field separates the charge carriers and minority carriers can hence reach the junction by diffusion. This results in a charge-collection current or electron beam-induced current, which can be amplified and used in a quantitative manner to measure the width of the junction and its depth below the surface, the diffusion length and the surface recombination rate of minority carriers, for example. The EBIC signal can also be used to image p-n junctions below the surface, to localize avalanche breakdowns and to image active lattice defects, which influence the recombination rate of minority carriers. The use of Schottky barriers, formed by evaporating a metal layer that forms a non-ohmic contact, allows semiconductor parameters and lattice defects in materials that do not contain a p-n junction to be investigated [4]."

Outside the above mentioned signals, some radiation losses are generated. It can be incoherent radiation caused by recombination process of electron-hole pairs or coherent radiation in form of Čerenkov radiation (it is deceleration radiation of charged particle which occurs when $v_e > \frac{c}{n}$ where v_e is speed of electron, c is speed of light and n the refractive index of a sample), transition radiation on interface of two media of different dielectric constants (it is coming, when dipole flips) or diffraction radiation (Smith-Purcell effect occurs, when electrons travel very closely parallel to the surface of a ruled optical diffraction grating).

3 Monte Carlo simulation of electron / sample interaction

Precise simulation of the interaction of an electron beam with a sample is the essential part of both qSTEM and qBSE imaging techniques. This chapter describes briefly the principle of Monte Carlo simulation of electron scattering (the name is based on using of coincidence as in hazard) for transmitted and back-scattered electrons. Detail description, including correct maths and references to individual physical phenomenons, is the main subject of many books such as [23, 44, 45, 46]. Even in very thin samples, multiple scattering occurs when elastic and inelastic scattering events are chained behind each other. This cascade of events is shown in Fig. 3.1, where the actual electron positions x_n, y_n, z_n , the paths between individual scattering events s_n , the scattering angle Θ_n and azimuth angle X_n are introduced.

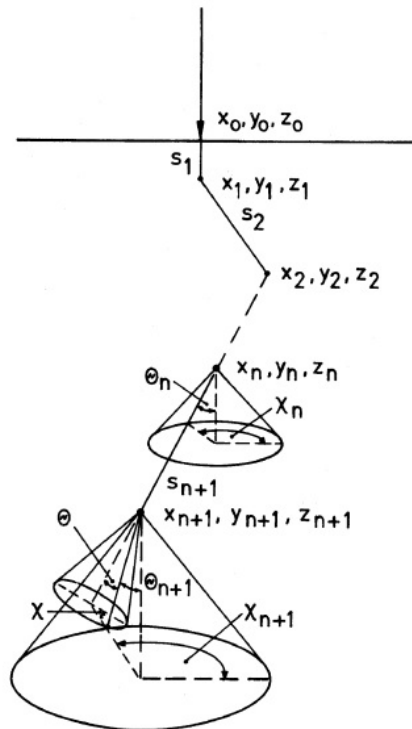


Fig. 3.1: Sequence of scattering processes in a Monte Carlo simulation with $s_n =$ free path lengths, $x_n, y_n, z_n =$ coordinates of electron at the n th collision, Θ_n and $X_n =$ scattering and azimuth angles after the n th collision. Taken from [4].

3.1 Principle

Monte Carlo electron trajectory simulation is based on step-wise simulation of the electron's behaviour after repeated inelastic and elastic scattering events. The individual phenomena are selected during the simulation by random numbers generation and its comparison with probability of each phenomenon.

In its simplest form, several simplifications are introduced:

1. All angular deviations of the electron are caused by elastic scattering. The angles Θ and X have to be determined after each elastic interaction.
2. The mean distance between scattering events is given by mean free path, which can be calculated for homogeneous, isotropic and amorphous samples as

$$\lambda = \frac{A}{N_A \rho \sigma}$$

where N_A is Avogadro's number, ρ the density, σ the total cross section and A the atomic weight of the target. If we take into account other types of interaction outside the elastic scattering, like inelastic scattering, phonon excitation or polaronic effect, the resulting mean free path λ is given by combination of individual mean free paths

$$\frac{1}{\lambda} = \frac{1}{\lambda_{\text{el}}} + \frac{1}{\lambda_{\text{inel}}} + \frac{1}{\lambda_{\text{phonon}}} + \frac{1}{\lambda_{\text{pol}}}$$

The step length between two individual scattering events is then computed as $\text{step} = -\lambda \ln(R)$ where R is a uniformly distributed random number in the range from 0 to 1.

3. Energy loss caused by inelastic scattering is calculated with the Bethe continuous energy loss expression described in 1930 [47]. It gives information about distance travelled by an electron in the matter because it estimates a decrease in electron energy accordingly to travel distance (dE/ds). It is usable for electron energies above 10 keV [44] and it may be found by integrating of Bethe continuous energy loss expression from the incident beam energy down to a low energy limit with the result

$$\frac{dE}{ds} = -7850 \left(\frac{Z\rho}{AE} \right) \ln \left(\frac{1.166E}{J} \right) \quad [\text{eV/nm}]$$

where E is the beam energy, Z the atomic number, ρ the density, A the atomic weight, and J the mean ionisation potential given by

$$J = \left(9.76Z + 58.5Z^{-0.19} \times 10^{-3} \right) \quad [\text{keV}].$$

The modification of Bethe expression for low electron energies was published by Joy and Luo in 1990 [48] in form

$$\frac{dE}{ds} = -7850\rho \frac{Z}{AE} \ln \left(\frac{1.166(E + KJ)}{J} \right) \quad [\text{eV/nm}]$$

where K is a material-dependent constant (e.g. 0.851 for Au, 0.83 for Cu, 0.815 for Al and 0.77 for C). This semi-empirical equation should be working at beam energy above 50 eV.

This very simple simulation block is repeated until electron energy is higher than the chosen limit or the primary electron is transmitted through a sample or back-scattered. In the above-introduced simulation, only transmitted and back-scattered electrons are simulated. In real software dealing with MC simulation of electron scattering is incorporated much more complex physics and the corresponding spectrum of simulated signals is wider (SE, X-ray, CL, AE etc).

The probability of elastic scattering depends strongly on the nuclear charge (atomic number Z) and electron energy E . It is expressed mathematically as a cross-section σ . There can be found several approximations or models differing from each other in its accuracy at different conditions like beam energy or low / high Z .

3.1.1 Rutherford cross-section

The simplest one is based on the scattering of alpha particles on gold nuclei and was originally described by Rutherford in 1911 [49]. Pure Rutherford cross-section neglects the fact, that positively charged atomic nucleus is screened by a negative charge of inner shell electrons, and so modified versions have been published. The Screened Rutherford cross-section together with relativistic correction was presented by Newbury in 1986 and Joy in 1995 [50, 51] as

$$\sigma = 5.21 \times 10^{-21} \frac{Z^2}{E^2} \left(\frac{E + mc^2}{E + 2mc^2} \right)^2 \frac{4\pi}{\alpha(1 + \alpha)} \quad [\text{cm}^2]$$

where E is electron energy, α the screening parameter which can be accordingly to [52] computed as

$$\alpha = \frac{me^4\pi^2}{h^2} \frac{Z^{2/3}}{E} = \frac{3.4 \times 10^{-3} Z^{2/3}}{E}$$

where m is the electron mass, e the electron charge, h the Planck constant, Z the atomic number and E the electron energy. The polar scattering angle Θ for an individual elastic collision can be computed by

$$\cos(\Theta) = 1 - \frac{2\alpha R}{1 + \alpha - R}$$

where R is a uniformly distributed random number in the range from 0 to 1. The azimuthal angle X is generated randomly as $X = 2\pi R$. Accuracy of Rutherford cross-sections is given by the first Born approximation

$$E \gg \frac{e^2}{2a_0} Z^2$$

where a_0 is the Bohr radius. The greater is electron energy than atomic potential, the greater the accuracy of the Rutherford theory.

3.1.2 Mott cross-section

Mott (unscreened) differential cross-section was expressed by Mott in 1929 and 1932 [53, 54] as two conditionally convergent infinite series in terms of Legendre expansions. It was computed many times as shown in [55] and tabulated values are available. The values located between tabulated values are then interpolated. Another possibility is using an empirical equation describing the total Mott cross-section, which can be found in Gauvin and Drouin (1993) [56] in the following form

$$\sigma = 5.21 \times 10^{-21} \frac{Z^2}{E^2} \frac{4\pi\lambda[1 - e^{-\beta\sqrt{E}}]}{\alpha(1 + \alpha)} \left[\frac{E + 511}{E + 1022} \right]^2 \quad [\text{cm}^2]$$

where λ and β are constants for a given element and can be found in the paper or computed by equations

$$\lambda = 1.162 + 1.28 \times 10^{-2} Z; \quad \beta = \frac{26.42}{Z^{1.24}}$$

and in Browning et al (1994) [57] in the form

$$\sigma = \frac{3 \times 10^{-18} Z^{1.7}}{E + 0.005 Z^{1.7} E^{0.5} + 0.0007 Z^2 / E^{0.5}} \quad [\text{cm}^2].$$

The cross-section should be valid for atomic numbers up to 92 and for energies from 100 eV to 30 keV.

3.1.3 ELSEPA based cross-section

Cross-sections with the name ELSEPA are the result of FORTRAN 77 code system, which performs relativistic (Dirac) partial-wave calculations for scattering by a local central interaction potential. It computes elastic scattering of electrons and positrons by neutral atoms, positive ions and molecules for projectiles with kinetic energy in the range from tens of eV up to 1 GeV. These codes deliver information including phase shifts, scattering amplitudes, differential cross-sections, total cross-sections and transport cross-sections. Full description of used models and approximations used for different projectiles and energies can be found together with program structure in a very detailed paper of Salvat et al (2005) [58].

3.2 Simulation software

Nowadays, a variety of Monte Carlo programs are available. They differ in their complexity, control interface, types of samples they can be used for, incorporated physical models, possible results and also cost (comparison in Tab. 3.1). In this section, some of often used Monte Carlo programs, which can be used for simulation of the interaction of the primary electron beam with a sample, are presented. All further mentioned programs work with amorphous samples. The interaction of an electron beam with crystalline samples depends highly on the orientation of individual crystals inside the sample and brings specific issues [59].

Tab. 3.1: Comparison of main features of MC software. Redrawn from [18] and actualised.

Name	Source Avail- able?	Bulk	Layers	GUI	Complex sample	X-ray spec. simul.	Program- mable
Casino	×	✓	✓	✓	✓ - ver. 3	×	✓ - PyPI
Win X-Ray	×	✓	✓	✓	×	✓	×
MC X-Ray	×	✓	✓	✓	✓	✓	×
NISTMonte	✓ - Java	✓	✓	×	✓	✓	✓
Penelope	✓ - Fortran	✓	✓	×	✓	✓	✓
LMS-MC	✓ - Fortran	✓	✓	×	×	×	×
NBSMonte	✓ - Fortran	✓	×	×	×	×	×
EFS*	✓	✓	✓	×	×	×	×
MC-SET	✓ - C++	✓	✓	✓	×	✓	✓
MONCA2	✓ - Matlab	✓	✓	✓	×	×	✓
MONCA	✓ - Matlab	✓	×	✓	×	×	✓
CHARIOT	×	✓	✓	✓	✓	×	×
GEANT4	✓ - C++	✓	✓	×	✓	✓	✓
EISS	✓ - Java	✓	✓	✓	×	×	×
MCSEM	✓ - C++	✓	✓	✓ ⁺	✓	×	✓

*Electron Flight Simulator [60] is not available on its webpage.

⁺It runs under Matlab or Octave.

CASINO program group

The word **CASINO** is an acronym which has been derived from the words "monte CARlo SImulation of electroN trajectory in sOlids". The CASINO 1 (described in [61]) was created in 1996 and actualised in 1999. After some time, the DOS interface became archaic and so the next version **CASINO 2** (described in [3]) was programmed for Windows with an easier graphical interface. The program was originally designed for low-energy beam interaction in a bulk and thin foil. It simulates transmitted and back-scattered electrons and X-rays with beam energy in the range from 0.1 to 30 keV [62]. The program can be controlled by a python interface **PyMonteCarlo** (described in [63]), which is characterised as "a programming interface to run identical simulations using different Monte Carlo programs. The interface was designed to have common input and output that are independent of any Monte Carlo code. This allows users to combine the advantages of different codes and to compare the effect of different physical models without manually creating and running new simulations for each Monte Carlo program. The analysis of the results is also simplified by the common output format where results are expressed in the same units [64]." **CASINO 3** (described in [65]) provides complex possibilities of sample geometry in 3D including 2D simulation of STEM signal [66]. It is possible to use the python interface **PyPI – pycasinotools** (described in [67]), which works with CASINO versions 2 and 3. **Win X-Ray** (described in [68]) is an extension of the CASINO, which includes statistical distributions for the back-scattered electrons, trapped electrons, energy loss and ϕ - ρ - Z curves for X-ray. The newly added features in Win X-Ray are the complete simulation of the X-ray spectrum and the charging effect for insulating specimen [69]. **MC X-Ray** (described in [70]) is an extension of the CASINO and Win X-Ray and it computes the complete X-ray spectra from the simulation of electron scattering in solids of various types of geometries. The MC X-Ray allows simulation up to 256 regions with different composition in a sample consisting of spheres, cylinders and combinations of horizontal and vertical planes [69].

NIST program group

DTSA-II is a software package for quantitative X-ray microanalysis, which is inspired by the popular Desktop Spectrum Analyzer (**DTSA**) package, developed by Chuck Fiori, Carol Swyt-Thomas, and Bob Myklebust at NIST (National Institute of Standards and Technology, USA) and NIH (National Institutes of Health, USA) in the '80s and early '90s. It is based on a code written by Nicholas W. M. Ritchie. DTSA-II was designed to make standards-based microanalysis more accessible for the novices because many operations, which previously needed user intervention under DTSA, are now performed automatically by the software [71]. It replaced the **NISTMonte** (described in [72]), because it provides all the same electron trajectory algorithms as NISTMonte, plus updated X-ray generation algorithms including primary and secondary fluorescence generation [18]. Another program originally designed for examination of X-ray masks using transmitted and backscattered electrons, **MONSEL** (versions **MONSEL I** described in [73], **MONSEL II** described in [74] and **MONSEL III** described in [75]), was merged with NISTMonte in 2005.

PENELOPE

PENELOPE (Penetration and ENergy LOss of Positrons and Electrons) is a general-purpose Monte Carlo code system for the simulation of coupled electron-photon transport in materials.

It is usable in the energy range from 50 eV to 1 GeV. Unfortunately, the interaction cross-sections for energies below 1 keV may be affected by sizeable uncertainties and the results for these energies should be considered as semi-quantitative. The incorporated physics is there in the form of a combination of first-principles calculations, semi-empirical models and evaluated databases [76]. More information about the software can be found on its web page [77] or in very detailed report [78] including used physical models, random sampling algorithms and much more. Batch simulation and data interpretation can be performed in an open-source software **pyPENELOPE** in an application programming interface, which is in the form of object-oriented programming. Other possibility is the use of a graphical user interface to setup materials, geometry, simulation parameters and position of the detectors as well as to display the results of simulation [76].

MONCA

MONCA is an add-on package for MATLAB environment. The program offers a graphical interface for the input of elemental composition, density and thickness of the specimen as well as the properties of the electron beam such as electron energy, the diameter and the divergence of the beam and the number of incident electrons. The output gives the characteristic scattering parameters like the mean free elastic and inelastic electron path. The simulated energy loss and scattering angle from each transmitted electron are stored in a 2D intensity matrix. Additionally, the radial intensity distribution at the bottom of the sample is available, providing a measurement for beam broadening. From the data stored in the 2D intensity matrix, e.g., the electron energy loss spectrum of the electron scattering angle and radial intensity distribution, can be displayed and detector signals can be determined according to the selected detection geometries. An important part is the calculation of the fraction of scattered electrons vs. sample thickness. The 2D matrix is subdivided into 10 variable “detection areas” and the related signals can be calculated and mixed. Three commonly used signals are predefined: annular dark field (ADF), inelastic dark field and zero loss. For the ADF, the program can automatically generate a nonlinear fit of its signal vs. thickness used for mass determination [16].

GEANT4

GEANT4 is a toolkit for simulation of passage of a particle through matter. The incorporated physics cover a wide range of processes including electromagnetic, hadronic and optical processes, a large set of long-lived particles, materials and elements, over a wide energy range starting, in some cases, from 250 eV and extending in others to the TeV energy (an extension for beam energies below 50 eV is described in [79]). It can handle also complex geometries. It is written in C++ language. It has been used in applications in particle physics, nuclear physics, accelerator design, space engineering and medical physics [80]. More information can be found in reference papers [81, 82, 83] or on the website [84].

CHARIOT

CHARIOT software can be used for simulation of processes in an SEM (signals, charging, complex electromagnetic fields and detectors) and electron beam lithography (energy and charge deposition) with the main emphasis on the accurate simulation of slow secondary electrons and charging. It uses an advanced physical model of electron scattering, called the discrete

loss approximation (DLA) model, which makes the software incomparably more accurate than the typical slowing down approximation (SDA) model. SDA models, based on the Bethe formula, lump all the scattering events into one number, depending on the electron energy and travelled distance (it works properly with beam energies over 8 keV). The DLA model considers all scattering events separately, simulating electron interactions with inner and outer shells of specific atoms, generation of plasmons, Auger electrons, modelling of all generations of secondary electrons until they stop. It includes Mott or Rutherford elastic cross-sections and semi-empirical model which is used for electrons with energy lower than 50 eV considering multiple generations of secondary electrons with electron propagation between sample layers. It computes the charge and discharge transfer functions, the local electrical fields and potentials [85]. More information can be found in descriptive articles [86, 87].

MC-SET

MC-SET (Monte Carlo Simulation of Electron Trajectories) is an electron trajectories simulation program written in C++ language. The program enables estimation of various parameters like electron back-scattering coefficient, energy, angular / energy spectral distribution, generation of secondary electrons, X-rays generation, electron beam depth dose etc. [88].

NBS Monte Carlo Program

The program was developed in '70s for studying magnetic contrast in an SEM, X-ray emission from particles and problems of quantitative X-ray microanalysis of tilted specimens. Detailed description can be found in [89].

EISS

EISS (Electron Interaction with solids — Single Scattering Monte Carlo simulation software) is a simulation program of the interactions between energetic electrons and solids. The electron-solid interactions are approximated by a model in which the electron-atom interactions are elastic, and the electron energy loss is continuous between elastic processes. The elastic interactions are described by the relativistic Mott cross-section, which includes spin-orbit coupling and remains accurate for low beam energies and high-atomic-number targets. Secondary electrons are generated and tracked within the "fast secondary" model. The program can work with planar samples with up to three layers with arbitrary thicknesses [90]. The program is written in Java and its physical content is mainly based in the approximations and algorithms described in the book written by David C. Joy [50].

LMS-MC

LMS-MC program is an introduction to Monte Carlo simulation of electron transport in solids and provides four options: a guide how to use Monte Carlo simulation, a single scattering simulation for thin foils, a plural scattering simulation for bulk samples and a plural scattering simulation of X-ray generation in a bulk sample [91].

MCSEM

MCSEM is a simulation program, written in C++, for the modelling of image formation in SEM. It consists of different modules for individual aspects of the image formation process like the probe forming, the geometric specimen model, the electron-specimen interaction, and the electron detection. It is possible to enhance the program with new modules. The electron-specimen-interaction module simulates the electron diffusion in solid-state and the generation and emission of secondary electrons. Elastic scattering is based on tabulated Mott scattering cross-sections and inelastic scattering is modelled by the Bethe formula. The specimen may be in the form ranging from simple 2D sample to complex 3D structures. The detector module enables the detection of back-scattered, transmitted and secondary electrons [92]. More information can be found in [93].

3.3 Processing software for quantitative STEM

qSTEM data can be processed by user prepared scripts in any programming language providing appropriate functions, toolboxes or libraries. It is not necessary to prepare own solution in every case and it is possible to choose one of the software or packages specially designed for qSTEM data processing. The software is arranged in chronological order.

IMPSYS

It is a specialised software package which allows the selection and integration over regions of interest on the images. It is coded in FORTRAN 77 and it allows calculation of characteristics like mass-per-box, mass-per-length and mass-per-area [94]. More information can be found in [95].

Application reference: The analysis of the major sources of systematic errors in qSTEM (like changes in magnification, operating conditions of the detector, sample purity, mass-loss kinetics or glutaraldehyde fixation) are investigated on tobacco mosaic virus [94]. The IMPSYS software is not available since the year 2012.

PCMass

It is a program for rapid viewing of STEM images, with the ability to perform accurate mass measurements. The program offers manual mass measurements which require the user to position a measuring circle or rectangle around particles of interest, or automated mass measurements which use a set of simple comparison models to align and categorise particles, providing size and shape information as well as mass [96]. For a detailed description see [97]. **Application reference:** The program was used for mass determination of DNA complexes in [96].

MASDET

MATLAB package **MASDET** provides user-friendly environment for analysis of qSTEM measurements. The package uses a linear relationship between the fraction of incident electrons scattered by a thin sample and its molecular mass. Thus the maximum thickness of an investigated sample is limited to approximately $2 \times$ mean free path length [98]. The package provides three types of measurements. It is mass-per-area for sheet-like structures (e.g., protein S-layers, thin organic films), the particle mass-per-box for globular structures (e.g., single

macromolecules, globular assemblies) – program-mode AREA and the particle mass-per-length for filamentous structures (e.g., intermediate filaments, tobacco mosaic virus) using the program-mode FILAMENT [99]. The improved version **MASDET2** avoids the limitations of the linear approximation by the nonlinear relation between signal and mass using MC simulations software. This approach may reach thicknesses approximately to $7\times$ mean free path length [98]. **Application reference:** The package was used for characterisation of hollow polymeric capsules [100] or mass measurement of tobacco mosaic virus [101].

Part II

Quantitative imaging

4 Quantitative STEM imaging

The field of electron microscopy offers many types of imaging techniques. In general, it is possible to divide all imaging techniques into two groups by dimensionality of the provided information. The first group gives 3D information about the investigated sample. Scanning electron microscopy is represented by techniques using repeated scheme "remove sample and take image", where the remove of sample parts is used in order to expose next parts of a sample. The remove of sample may be performed by focused ion beam milling (FIB-SEM; the technique provides high resolution in z direction which enables creation of isotropic voxels, but it takes long time and due to that it is suitable for lower sample volumes) or by repeated cutting of a sample by ultramicrotome mounted inside of the microscope chamber (serial block-face imaging; SBF-SEM offers higher investigated volumes but with anisotropic voxels – the size of z is given by lowest slice thickness possible to cut). In the case of transmission electron microscopy, it is possible to use array tomography, where a sample is cut to series of thin sections and than imaged, stage tilt tomography using the subsequent sample reconstruction from its projections at different angles or single-particle analysis, where identical copies of sample in different orientations are imaged and its 3D structure is computed.

The second group is imaging in 2D. This big group contains a conventional imaging in SEM using a variety of detectors and signals or a planar projection of a sample in TEM and STEM. Quantitative scanning transmission electron microscopy imaging comes up with a way how to get more quantitative information about the thickness of a sample at each pixel from a single image, but also offers other information about the sample such as a mass per length of filamentous structures, mass per area of sheets, or mass of particles. qSTEM is not the only possibility how to measure the thickness of a sample using transmitted electrons – EELS can be used as well. The difference is in the use of mainly inelastic scattering instead of elastic scattering used in qSTEM [102].

There are three types of STEMs accordingly to their beam energy. The first one is TEM with the possibility of probe scanning across the sample with beam energy in the range from 80 to 300 kV. The second one is STEM microscope with lower beam energy which may be represented by dedicated STEM (for example NION HERMES has beam energy range from 30 to 200 keV [43]) or (S)TEM (for example ThermoFisher Scientific Talos L120C which has beam energy in the range from 20 to 120 keV [103]). Interesting option is aberration corrected (S)TEM, which is the result of SALVE project (Sub-Angström Low Voltage Electron microscope) operating in range of energies from 20 to 80 keV [104]. The third is SEM with retractable STEM detector inside the microscope chamber. This type is often called low-voltage STEM and provides beam energies from hundreds of eV up to 30 keV. The special case of low-voltage STEM are LVEM 5 and LVEM 25 (DeLong Instruments, Czech Republic) operating around 5 and 25 keV [105, 106]. The microscopes have lenses made of permanent magnets and focusing is done by changing the sample position in z -axis and variation of beam energy.

In the conventional TEM with high acceleration voltage is the image contrast enhanced by staining using salts of heavy metals like uranyl acetate or lead citrate [107]. It brings problems with changes of the internal structure of the sample and limits the best reachable resolution. The solution is to image the sample without staining. This is possible in case of TEM with a use of modern direct electron detectors [108, 109], which offers imaging with a lower electron dose and with higher detective quantum efficiency (DQE). The second possibility, how to increase

the image contrast, are phase plates for using phase-contrast, but those are located in the back focal plane of the objective lens and so it is not possible to use it in STEM, where there are no lenses behind the sample.

Contrast enhancement is not necessary in case of low-voltage STEM (beam energy ≤ 30 keV), where image contrast is much higher even for light elements. It is caused by higher electron scattering coefficients at lower beam energies [110]. Imaging without staining brings the advantage of observing samples closer to a native state if the preparation is done by sophisticated cryo methods. Low-voltage STEM is an appropriate method for many types of structural studies of thin biological samples, ultra-thin sections, viruses etc. as used in [111, 112]. Due to the small mean free path of electrons in solids (example in Tab. 4.1) it is necessary to prepare very thin samples with maximum thickness in tens of nanometers. For such thin samples, the background in the image has to be minimised using very thin supporting layers.

Tab. 4.1: Mean free path dependency on beam energy and type of a sample. Calculated in software MONCA [16].

	λ [nm]	Density [g/cm ³]	Beam energy [keV]			
			15	30	100	200
Sample	C	2.0	14.6	25.8	64.8	102.1
	Au	19.3	2.0	3.2	7.5	12.0
	EMbed 812	1.25	19.6	30.8	82.3	129.1
	Protein	1.35	19.1	33.1	80.6	126.5

4.1 History

Origins of molecular weight determination by TEM are in the '60s, around 30 years after the construction of the first TEM by Max Knoll and Ernst Ruska in 1930. Commercial production of TEMs began by the company Siemens and Halske in 1939 with an image resolution of 10 nm. Development of SEM was slower. The essential parts were the development of scanning beam in 1938 by Manfred von Ardenne and the discovery of photomultiplier by an American scientist of Russian origin Vladimir Kozmič Zworykin.

The method of measuring the thickness of isolated specimens in the electron microscope with the implementation of measurement of its mass and density was described at first in the work of Marton and Schiff in 1941 [113]. The very useful point was introduction of cold trap for carbon contamination reduction in 1953 [114]. The first application of the method was measurement of a relative increase in mass-thickness of tomato bushy stunt (BSV) and tobacco mosaic (TMV) viruses after staining by Hall in 1955 [115]. The theoretical background of quantitative electron microscopy was in general discussed in [116, 117] and focused on mass-scattering cross-sections of different test samples in [118, 119]. The initial studies were followed by rapidly increasing number of applications, for example, analysis of electron staining [120], measurement of mass-thickness of disrupted cell membranes [121], density measurement of thin sections [122], mass measuring of spermatozoa with weight 7×10^{-12} g and T2 bacteriophages with weight 3×10^{-16} g [123]. Two years later in 1962 the particles with a diameter around 200 Å and weight of 10^{-18} g were measured with an error lower than 10 % [124]. The first electron beam induced

mass-loss study was done in 1978 on a protein sample with weight of 10^{-17} g [125]. An important improvement was using sample cooling for increase of accuracy of determining length mass of tobacco mosaic virus in 1981 [126].

The basic scheme of qSTEM experiment published by Engel et al [127] is in the main features – using scattering theory as simulation and known detector geometry as image normalisation – used in this thesis. The advantages of the method are: wide range of measurable mass from a few thousand up to several hundreds of million Daltons¹, relatively low amount of sample which is needed for the analysis (< 1 μg) and the possibility of sample characterisation where total mass does not make sense – mass per length for filaments or mass per area for flat structures [96].

Compared to other analytical techniques, which give mean value of many particles as the result, the qSTEM gives information about mass/thickness of a particle together with high-resolution image. It offers a possibility to relate the obtained characteristics to each single nanoparticle. The method of qSTEM may be used in any microscope allowing STEM mode. It can be high-energy TEM (300 keV) as used in [128] or its implementation into commercial high-resolution SEM, where some specific changes of hardware and software may be needed for precise system calibration [129, 130].

4.2 Principle

In a nutshell, the method compares the captured electron intensity normalised between 0 (mean pixel value of the “dark” image) and 1 (mean pixel value of the “bright” image) with a simulated intensity calculated from the number of electrons captured by the detector at a known detection angle and the total number of simulated electrons. qSTEM measurement can be done using commercially available detectors. The disadvantage is neglecting of electron beam current changes and the corresponding change of the captured signal.

The main assumptions of the method are:

1. Known geometry of the detection system that usually contains the geometry and position of the detector, the sample holder and the pole piece of the final demagnifying lens.
2. Known density and composition of an investigated sample.
3. Linear response of the detector to the electron beam.²

For quantitative measurement, it is necessary to calibrate data before processing them. We used two images captured during each imaging session (Fig. 4.1), one of them for no electrons impacting on the STEM detector, which is shaded by a grid holder (signal in the image is given by brightness settings), and the other for all primary electrons impacting on the STEM detector (which has to be under saturation level).

All measured images of real samples are somewhere between those extreme values. Using this calibration and normalisation of all data to the real probe current in each imaging session, the influence of fluctuations in measurement conditions among individual measurements are eliminated. There are of course other calibration options like a comparison of image intensity

¹Relative molecular weight unit used in biochemistry and biology. 1 Da is equal to 1 atomic mass unit, which is equal to 1/12 mass of the C12 carbon atom. $1 \text{ Da} = 1 \text{ u} = 1.66 \times 10^{-27} \text{ kg}$.

²In case, that this assumption is not met, a precise calibration of STEM detector accordingly to a wide range of impacted probe currents has to be done and taken into account during the data processing.

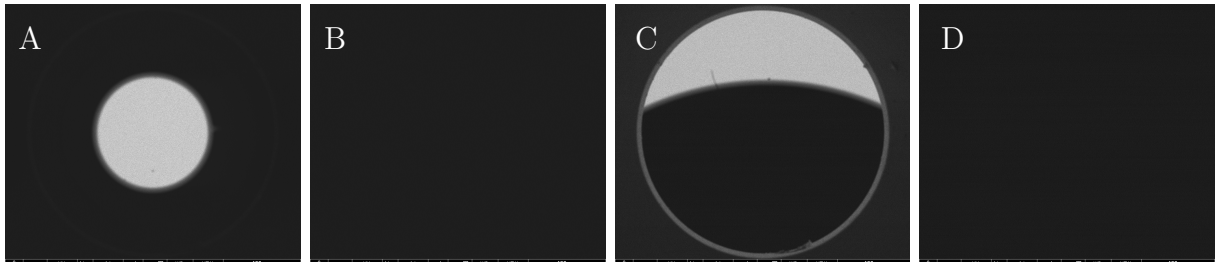


Fig. 4.1: STEM detector calibration images. (A-B) Full and blanked beam image of the BF segment. (C-D) Full and blanked beam image of part of the HAADF segment. All images are taken with the same imaging conditions as a sample. One single change is in magnification (high $\rightarrow 48\times$).

at standard samples as used in [131]. As clear from the principle of STEM imaging, shown in Fig. 4.2, the samples are mounted on TEM grids. It depends on the type of the sample if the supporting film is used. It is necessary e.g. for imaging of individual nanoparticles or clusters. On the other hand, standalone sheets may not need any support. It is desirable to use a film as thin as possible with sufficient endurance to the electron beam.

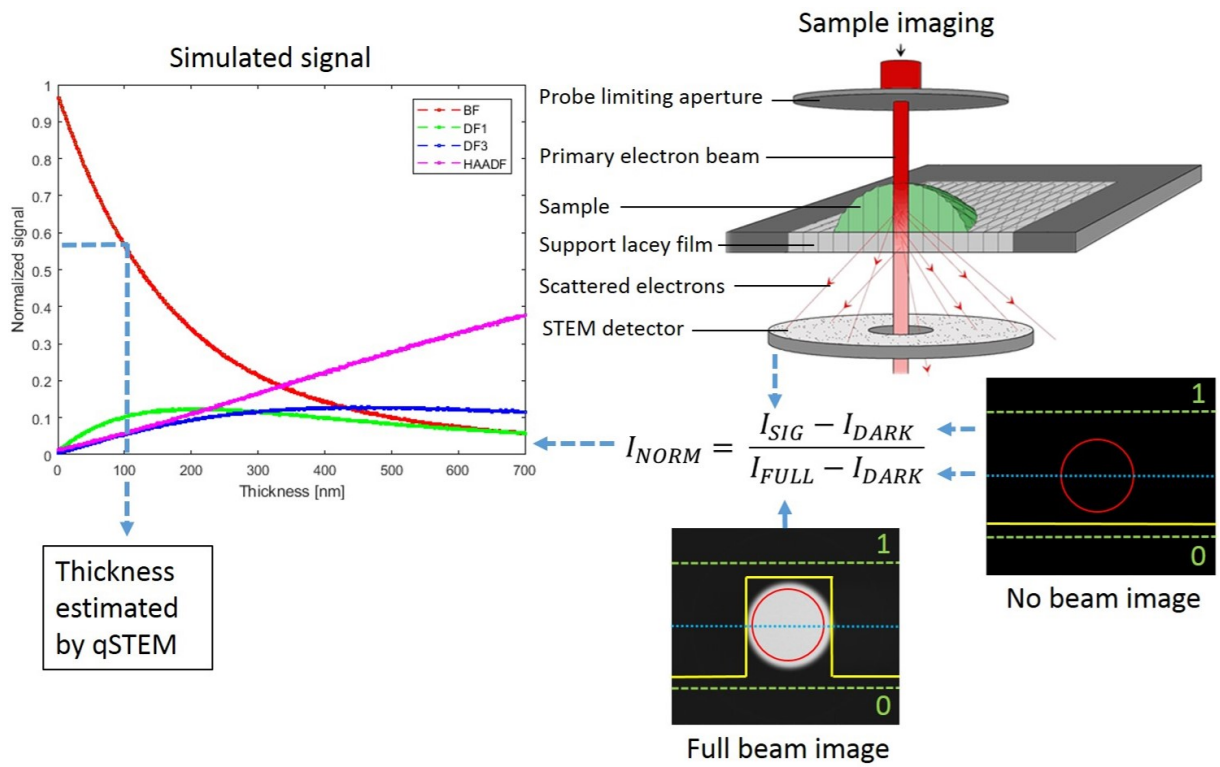


Fig. 4.2: Principle of qSTEM. Electrons scattered by a sample are captured by the detector with known detection angles. The intensity of detected signal normalised accordingly to calibration images (yellow scan shows signal in blue line due to the signal range in green) carries information about mass/thickness of a sample. The resulting thickness is determined by the MC simulation.

4.3 Application area

The application area of qSTEM is very wide and consists of different types of samples, imaging strategies and studied features. It can be divided accordingly to the detector type. The annular detector gives information about the amount of electrons impacting the detector in given scattering angle ranges (schematically shown in Fig. 4.3 A). In opposite, the pixelated STEM detector gives a full scattering pattern captured by the rectangular matrix of pixels (shown in Fig. 4.3 B; classical STEM segments like BF, DF and HAADF can be calculated from individual pixelated data).

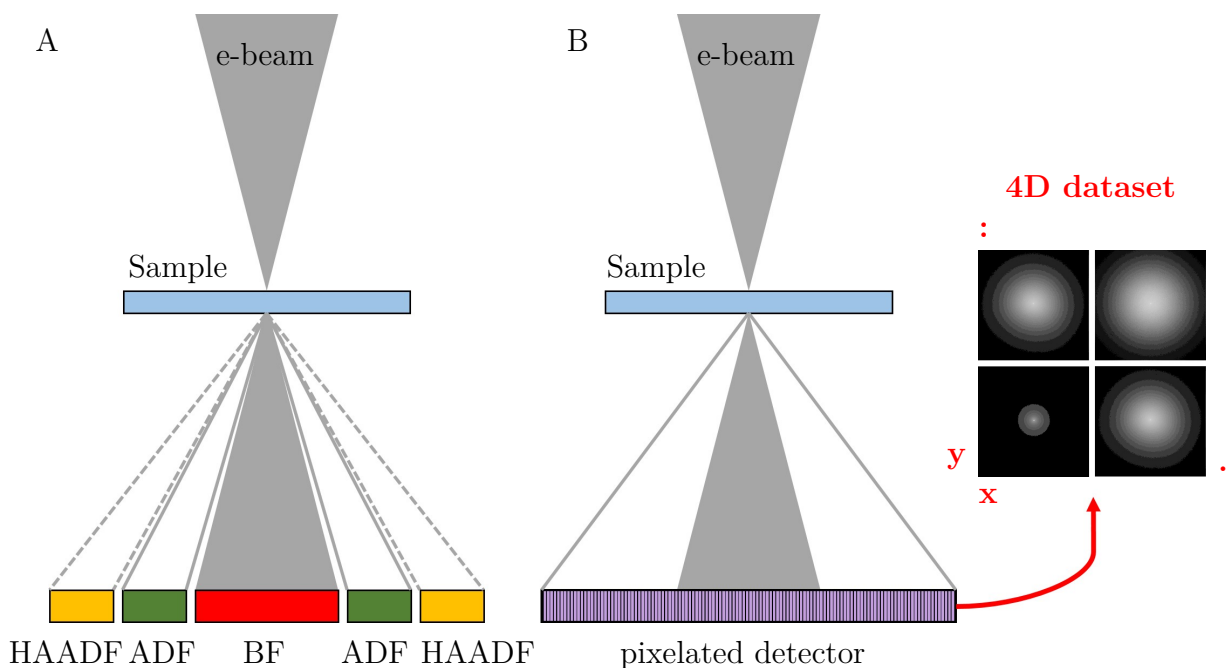


Fig. 4.3: Comparison of annular and pixelated STEM detector. (A) The shown annular STEM detector can capture simultaneously up to three images, with given detection angles, describing electron scattering in a sample (BF, ADF, HAADF). (B) 2D-STEM detector captures full scattering pattern for each beam position and creates 4D dataset for further processing.

4.3.1 Annular STEM detector

Application area can be divided into several groups:

- **measuring of molecular weight and mass distribution per length or area (for filamentous and sheet-like structures)**
 - hemocyanin assemblies with accuracy higher than 3% [128]
 - HET-s fibrils (fungal prions – infectious filamentous polymers of proteins) [132]
- **electron beam induced mass-loss**
 - variety of biological samples like TMV or GroEL chaperonin [133]
 - embedding resins – more details and applications in Section 8.4
- **geometrical properties**
 - lateral and vertical size of silica nanoparticles with size 10–100 nm [134]
 - 3D characterisation of drug-encapsulating polymer particles [135]

- thickness of fluorenyl hexa-peri-hexabenzocoronene films and C, Si, GaN and W wedges [136]
- thickness and particle boundary determination of Si, Au and latex nanoparticles [137]
- **physical phenomena**
 - electron scattering in amorphous carbon and carbon-based materials like a-carbon, P3HT or EPON [130]
 - STEM-ADF contrast formation at images of gold nanoparticles on silicon nitride (SiN) substrates of various thicknesses [138]
 - beam broadening and contrast/resolution dependency on specimen thickness studied on semiconductor multilayers and Sb precipitates in a Si implanted specimens [131]
 - screening parameter in differential screened Rutherford cross-sections for MC simulations under 30 keV [139]
- **local composition**
 - concentration of In in $\text{In}_x\text{Ga}_{1-x}\text{As}$ quantum wells (density of areas with different composition is calculated by linear interpolation of known densities of pure InAs to GaAs) [140]

4.3.2 Pixelated STEM detector

Pixelated or 2D STEM detectors found a great application potential in the field of material science and diffracting samples in general. A comprehensive review of available techniques based on 4D-STEM (2D diffraction patterns in 2D scanning matrix) can be found in review article [141] and py4DSTEM software package introduction [142].

Sample thickness estimation

2D-STEM detector was used for thickness fitting of PbWO_4 crystals using PACBED method (Position-Averaged Convergent Beam Electron Diffraction) where captured and simulated diffraction pattern was compared by eye with accuracy better than 10 % for thickness and better than 1 mrad for specimen tilts [143].

Organic/soft samples

2D-STEM detector use for organic/soft samples is much rarer. It can be found an analysis of short and medium-range order in aperiodically packed organic molecules using electron diffraction based PDF (Pair Distribution Function) analysis [144], grain orientation in organic semiconductor nanocrystals [145] or size and distribution of nanoscale crystalline regions mapping in polymer blend (the model polymer blend is a 50:50 w/w mixture of semicrystalline poly(3-hexylthiophene-2,5-diyl) (P3HT) and amorphous polystyrene) [146].

Amorphous samples

In case of using 2D-STEM on amorphous samples the main advantage of such detector – capturing of full diffraction pattern – is lost when the sample does not produce diffraction. The use on amorphous samples is limited to two methods:

- **Amorphous strain mapping** – scattering patterns of samples with a high content of amorphous phase include ring-like features with a radius given by a characteristic scattering length. The local increase or decrease in the average atomic spacing will cause a decrease or increase respectively in the amorphous ring radius. This deviations caused by local strain may be measured by fitting of elliptical function to captured patterns [142].
- **Radial distribution functions** describes the relative density of atoms in some distance r from a given atomic position. It gives information about the distribution of distances between atoms in a sample which depends on the structure of material, chemistry and defect density [147].

As visible from application and method review above, there is a lack of 4D-STEM studies in the intersection of **sample thickness estimation** technique and investigation of **amorphous samples** together with Monte Carlo simulations as used in annular STEM detector based qSTEM. Method for thickness estimation of amorphous samples using 2D-STEM detector using Monte Carlo simulations is described in Part III: Results, Chapter 9.

4.4 From qualitative to quantitative imaging

Change from qualitative to quantitative imaging is done by comparison of captured and normalised signal with a simulation which is computed for different sample properties like local thickness, shape, composition or density. The simulation settings have to match the experimental conditions of the microscope.

There are theoretical formulas for a description of multiple electron scattering [148, 149]. The transport equation for electrons could be solved numerically [150], but it is still challenging and requires elastic and inelastic scattering cross-sections. For easier using, the semi-empirical equations were found for specific electron energies and atomic numbers [151, 152]. The angular distribution of the electrons after transmission through a thin sample is approximated by a Gaussian function. The normalised electron intensity is described in [152] as

$$\frac{I(\Theta)}{I_0} = \frac{d\Omega}{2\pi\overline{\Theta^2}} e^{-\frac{\Theta^2}{2\overline{\Theta^2}}}$$

where I_0 is the intensity of impacting electrons, Θ the scattering angle and $\overline{\Theta^2}$ the mean quadratic scattering angle. For the electron intensity scattered to the detector, the previous equation has to be integrated over the solid angle $d\Omega$. Another equation (based on the screened Rutherford cross-sections) was derived by Bothe in 1933 [151]

$$\overline{\Theta_B^2} = 10^9 \left(\frac{3.6Z}{E} \right)^2 \frac{\rho t}{A} \quad [\text{rad}^2] \quad (4.1)$$

where $\overline{\Theta^2}$ is the mean quadratic scattering angle, Z atomic number, E electron energy in eV, A atomic mass number and ρt the mass-thickness in kg m^{-2} . The factor of 3.6 was determined by comparison of theory and experiment by Crowther in 1910 [153] (unfortunately at beam energies in the range from 150 to 240 keV). The term is not accurate for light elements ($Z < 13$) and low energies according to findings in [152]. They modified the equation (4.1) for low energies by changing the factors as shown in (4.2).

$$\overline{\Theta_C^2} = 1.2 \times 10^6 \frac{Z^{1.3} \rho t}{E A} \quad [\text{rad}^2] \quad (4.2)$$

The equation (4.2) is, according to Cosslett [152], working for elements with $Z \geq 13$. Unfortunately the equations (4.1) and (4.2) have not been tested for light elements ($Z < 13$).

Fortunately, there is another way, how to get a theoretical description of electron scattering at defined sample and beam conditions. Nowadays, the Monte Carlo simulations are used in the absolute majority of published papers dealing with quantitative STEM. Example of the MC simulation results of latex ($[\text{C}_6\text{H}_6]_n$), which are shown in Fig. 4.4, were done in CASINO 3.3.0.4 [65] in range of thicknesses from 0 to 800 nm and in range of densities from 0.5 to 2.0 g/cm³. The influence of supporting carbon layer to thickness accuracy (described in [154]) was solved by adding such layer to the MC model. Correction to back-scattered electrons (described in [136]) and the resulting reduction in the number of electrons impacting the STEM detector was taken into account during MC simulation as well. Physical model ELSEPA [58] was used for partial and total cross-sections. The number of electrons in each point was 200,000 for suppression of the statistical error. A detailed description of available MC programs can be found in Section 3.2.

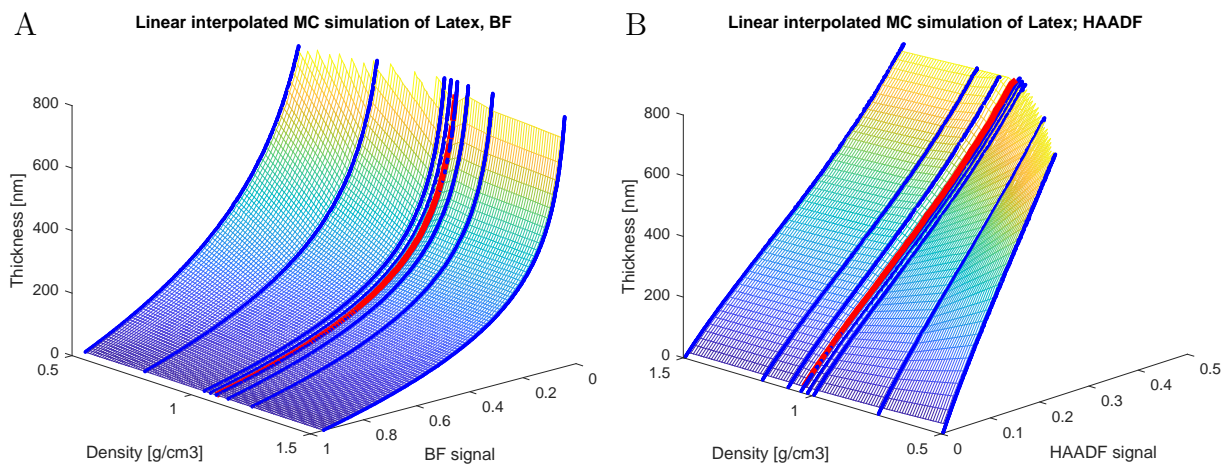


Fig. 4.4: Monte Carlo simulation signal space of latex in BF (A) and HAADF (B). Notice the inverted signal axes. The used density of 1.05 g/cm³ is highlighted in red. Capturing angles are 0-34 mrad for BF and 167-637 mrad for HAADF.

Two combinations of Monte Carlo simulation and a scripting language were used in the practical part of the thesis:

MATLAB/MONCA

This combination makes data analysis very simple because the MONCA simulation software is running under MATLAB – passing the simulation outputs to data-analysis script is then in the form of variables in the workspace.

MATLAB/CASINO 3

This combination enables the use of very sophisticated Monte Carlo simulation tool with all supported features. The simulation outputs were saved in a structured text file and loaded in MATLAB data analysis script. In opposite to the previous combination, the data export like saving and loading need to be done manually by the user.

For a simulation of many thicknesses in one simulation run in CASINO software, the wedge sample shape with an angle of 5° and a maximum thickness of 800 nm was used (shown in Fig. 4.5). Local thickness is computed from this angle and position of the beam relative to its projection into the plane of the base of the wedge. This shape enables to perform a multiple thickness simulation in one line scan across the body.

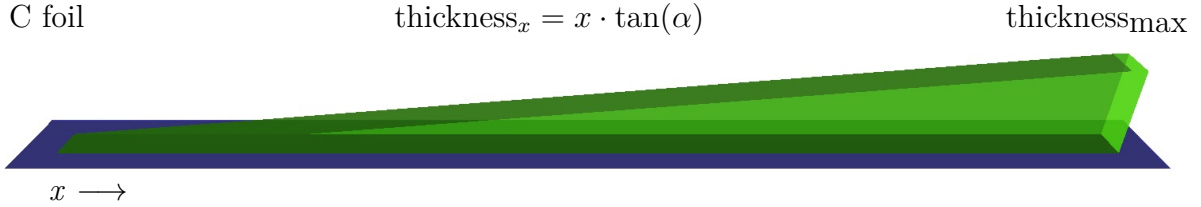


Fig. 4.5: Geometrical body used for MC simulation of different thicknesses by performing single line scan (CASINOv 3.3.0.4). Supporting carbon layer is blue and simulated sample is green. The wedge angle is $\alpha = 5^\circ$. Local sample thickness is computed from the known beam position and the angle.

4.5 Density-thickness dualism

By considering that a sample contains a number of N atoms in a unit volume, a total scattering interaction cross-section Σ is given as

$$\Sigma = N \cdot \sigma = N_A \cdot \sigma \cdot \frac{\rho}{A}$$

where N_A is Avogadro number, σ scattering cross-section, A atomic mass, ρ density. Introducing the sample thickness t results in

$$\Sigma \cdot t = N_A \cdot \sigma \cdot \frac{\rho \cdot t}{A}.$$

This equation gives the likelihood of a scattering event. The term $\rho \cdot t$ is called mass-thickness. Doubling ρ leads to the same Σ as doubling t [155]. As a result, we can measure the samples in two different modes:

- **Constant density** – in this mode the density of the sample is known and local thickness is measured (it is possible to estimate mass distribution across length or area). This mode is applied in Part III: Results, Sections 8.4 and 9.1.
- **Constant thickness** – it is usable in cases, where the sample has defined thickness with low variation (e.g. thin sections cut by ultramicrotome) and local density is changing.

5 Quantitative BSE imaging

Although qSTEM is an excellent method for measuring the thickness in the nanometer scale, it has one crucial limiting factor. The samples have to be thin enough for penetration by primary electrons. This limits the method for the use on thin films, nanoparticles distributed on the support layer, standalone lamellas etc. It would be appropriate to use a similar concept for thickness coating measurement on substrates. The principle of quantitative BSE imaging is the same as in the case of quantitative STEM (described in Section 4.2). There are papers dealing with physics of electron back-scattering in a theoretical way like [156, 157, 6], but in practice, the easiest solution is the Monte Carlo simulation as in the case of the qSTEM.

5.1 Principle

The signal captured by the BSE detector is dependent on several factors such as elemental composition and its corresponding back-scattering coefficient, the local thickness of individual layers or grains, the local density, the energy of the primary electron beam, the collecting angle of the BSE detector and the application of beam deceleration [158, 159, 100]. The maximum measurable layer thickness by qBSE imaging is given by the acceleration voltage and the corresponding penetrability into the sample [160]. Higher acceleration voltage brings a wider measurable range of thicknesses, but with lower modulation of the signal by unit thickness change. It follows that for high-precision with thin layers, the lower acceleration voltage is preferred and, for a high measurable range of thicknesses, higher beam energy should be used as we reported in [11]. The dependency of the measurable range of thicknesses is demonstrated in Fig. 5.1.

5.2 Calibration methods

Calibration of the BSE detector response to the primary electron beam plays a crucial role in the precise data acquisition and the corresponding data processing where the captured data are compared with simulated signal intensities. The limits or calibration points bring a connection between the experiment and simulation and thus allow assigning the correct covering layer thickness to the corresponding BSE signal. Several approaches for calibration of the BSE signal have recently been published:

One tail relative calibration – upper limit

This type of data calibration was used in [161], where the BSE images of thin Pd layers on a silicon wafer are normalized by the BSE signal of bulk Pd. The same detector settings for all samples were achieved by simultaneous imaging of all four samples (Pd bulk, Pd 10 nm, Pd 110 nm, and Pd 270 nm), and the BSE intensities are compared to each other. The same calibration was applied also in the case of measurement of Au layers on a Si substrate [162], where the upper limit is the measured BSE coefficient from bulk Au.

One tail relative calibration – bottom limit

It is based on image background measurement in the vacuum part of a “sample”. The upper limit is then floating just under the saturation limit of the detector. This detector calibration

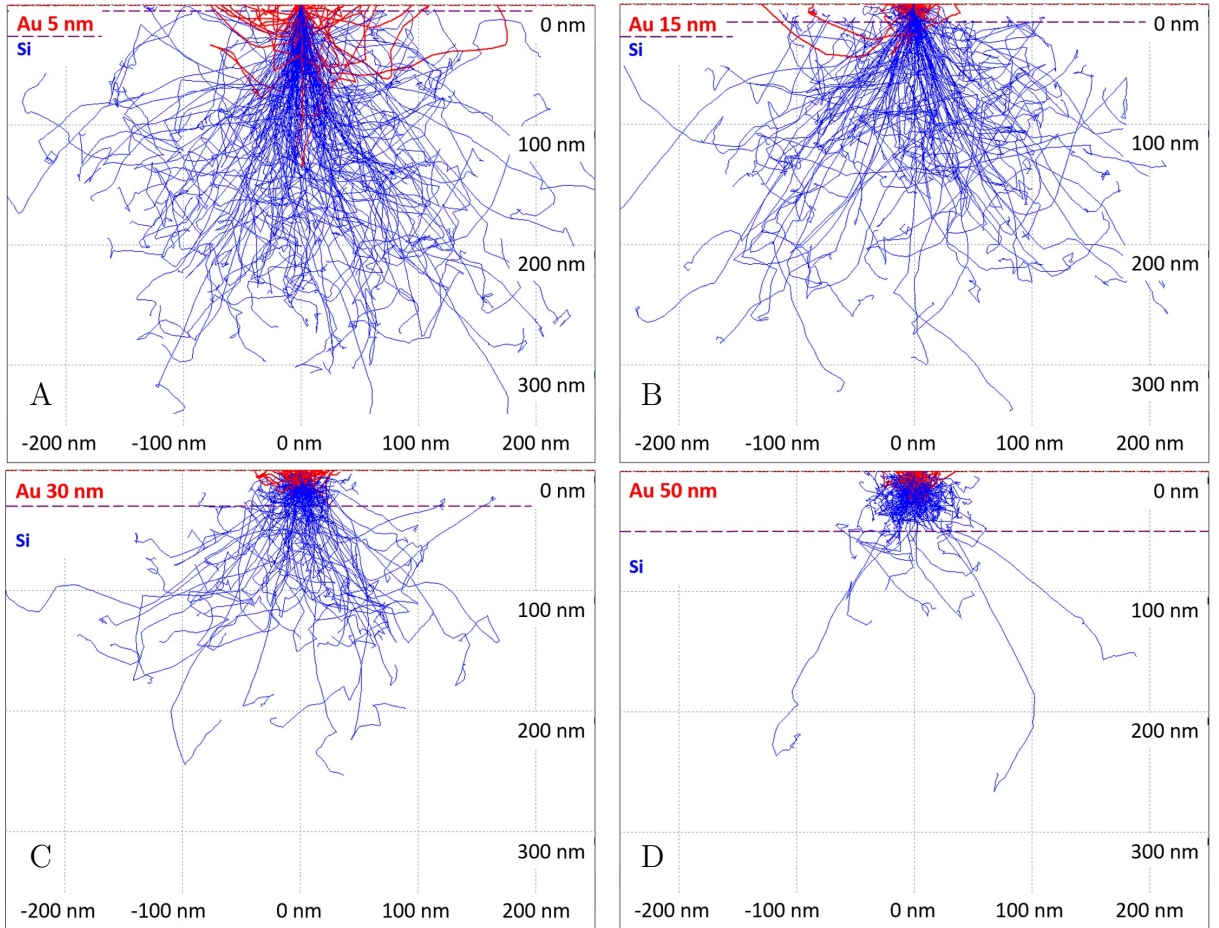


Fig. 5.1: Principle of signal change in qBSE imaging. (A) Gold 5 nm; nearly all electrons penetrate the layer and scatter in the substrate but BSE coefficient is higher than in the case of pure substrate. (B) Gold 15 nm; a significant part of the electrons is back-scattered in gold layer and do not penetrate into the substrate. (C) Gold 30 nm; nearly all BSE are emitted from the gold layer – the accuracy of the method is decreasing. (D) Gold 50 nm; all BSE are emitted from the gold layer, there is no difference between the thick layer and a bulk – it is upper detection limit. All simulations were computed in CASINOv 2.48 (beam energy 5 keV, Mott cross-section).

was applied for the determination of the $\text{In}_x\text{Ga}_{1-x}/\text{GaAs}$ ratio in the wedge-shape sample that was prepared by FIB-SEM in [163]. The density of a sample with changing composition was determined by linear interpolation of pure GaAs and InAs densities. The local thickness is calculated from the sample geometry of the wedge shape. Such measurements were analogically performed also for very thin samples using a STEM detector [140].

Two tail relative calibration

The captured signal is in this type of calibration normalized to the interval given by limiting values. In [164], the BSE signal of the Si substrate is used as the lower limit and the signal of the Au substrate is used as the upper limit. Another combination of limits is the detector response to the blanked beam as the lower limit and the BSE signal of the crystalline Si sample as the upper limit [165].

Multi-point relative calibration

The use of standard based calibration is shown in [166], where 26 mineral standards describing the correlation between the BSE signal and the changing atomic number Z in the range from 10.41 to 73.16 is used. The atomic number Z of an unknown sample can be determined with maintaining the imaging conditions from the measured BSE signal – Z dependency.

All of the above-mentioned methods for calibration of the BSE detector are relative to chosen limits and therefore dependent on the calibration sample. The disadvantage is the possible variation of those limits with the use of different calibration standard qualities, cleanliness, and homogeneity [11].

Electron mirror calibration

The absolute calibration method developed by the author of the thesis is described in detail in Part III: Results, Chapter 10.

5.3 Application area

The first comprehensive application of Monte Carlo simulations of back-scattered electrons for analysis of thin films on substrates is described in [167]. In this work, the thickness of Au layer on Al substrate and Al layer on Au substrate is measured using theoretical calibration curves. The asymptotic signal part in the area of high layer thicknesses was used as the connection to measured data. Other applications were done at different types of samples/systems in both theoretical and experimental way:

- measurement of mass and thickness of respirable dust particles [168]
- measurement of BSE coefficients on C, Al, Cu, Ag and Au samples [158]
- investigation of a semiconductor multilayer structure of AlAs in GaAs [169]
- carbon layer thickness measurement on Al substrate for possible replacement of the metallic coatings on plastic materials used for food packages [170]
- contrast formation investigation of SE and BSE images for nanosize Pt particles in a carbon matrix [171]
- looking for optimal beam energy to differentiate Au, Ag, Ge, Cu and Fe thin films on Si substrate at nanoscale [164]
- Pd and Au surface layer thickness measurement on a Si substrate [161]
- quantitative mean atomic number assessment in minerals and creation of Z maps [166]
- thickness determination of Au overlayers (25- 200 nm) on Si bulk substrates [162]
- BSE-SEM contrast optimisation of SiO₂ NPs on ITO/glass and ITO/glassy carbon substrates via beam energy and working distance setting [172]
- dependency of the back-scattering coefficient on the thickness of a thin C-layer on the top of a Au-substrate and the reverse of such geometry for a wide range of primary electron energies [173]
- C contamination layer influence to BSE energy distribution of Al and Au samples [174]
- prediction of material contrast for Al_{0.22}Ga_{0.78}N/GaN layer system which is used in high electron mobility transistors [165]

Part III

Results

6 Motivation & research strategy

Even established imaging techniques are not perfect and there is a plenty of room for other instrumental development and introduction of new methods, and this thesis would like to propose some solutions. Namely, the *Chapter 8: Quantitative imaging using semiconductor annular STEM detector* describes the accuracy of intensity-based qSTEM method together with detailed analysis of detector positioning error and its influence on the obtained results, the *Chapter 9: Quantitative imaging using pixelated STEM detector* brings new application area of this detector type in a field of amorphous samples and the *Chapter 10: Quantitative imaging using BSE detector* is looking for absolute calibration method for BSE detectors, which extrapolates the accuracy of thin-film thickness estimation on substrates to the new level.

Non-single imaging technique provides all the comprehensive information about investigated samples and it is necessary to combine different information from imaging techniques or detectors based on the detection of complementary signals. The thesis focuses on the combination of those techniques in *Chapter 11: Correlation of various signals in SEM*, in order to obtain comprehensive information about investigated samples and looking for ways how it can be done.

After individual issue identification, a possible solution has been proposed, designed and verified on appropriate test samples. The results were compared with state of the art results published in the available literature, summarised and submitted for publication in the peer-review process.

Used instrumentation

All main instrumentation used in this thesis is situated in Laboratories of Electron Microscopy at the Institute of Scientific Instruments of the Czech Academy of Sciences. In addition to the microscopes themselves, described in the following subsections, the auxiliary devices have been used. For surface plating and thin-film preparation, the **sputter coater Q150T ES** (Quorum Technologies, United Kingdom) and **high vacuum sputter coater ACE600** (Leica Microsystems, Austria) were used. The ACE600 can be operated at room or cryo temperatures including freeze fracturing, carbon and metals coating and transfer of the sample under vacuum to the SEM chamber. Vitrified samples were frozen by **high pressure freezer EM ICE** (Leica Microsystems, Austria).

Scanning electron microscope Magellan 400L

The microscope was used in most of the work (shown in Fig. 6.1 A; FEI - ThermoFisher Scientific, USA). It is an SEM with excellent limit resolution under 1 nm, which is achievable in range of acceleration voltages from 1 to 30 kV. It is equipped with Schottky emission gun, Elstar column and UniColore mode. When the mode is on, the primary electron beam energy range is lower than 0.2 eV. It suppresses chromatic aberration significantly and enhances the imaging quality at low beam energy. Operational probe current is in the range from 1.6 pA (0.76 pA in case of UniColore mode) to 100 nA. It is equipped with liquid nitrogen-filled cold trap and plasma cleaner for reduction of the sample contamination. The stage can be biased in the range from +50 V to -4000 V, which is used for suppression of emission of secondary electrons or as cathode lens for deceleration of the primary electron before its impact on a sample (it is possible to go down with the landing energy below 50 eV). The microscope has three different modes of the final lens (field-free, immersion and EDX) accordingly to the amount of magnetic field in the vacuum chamber. For capturing of electrons, presented SEM is rig out with Everhart-Thornley Detector (ETD) of secondary electrons, Through The Lens Detector (TLD), which can be set up for capturing of SE or BSE, retractable segmented semiconductor Circular Backscatter Detector (CBS) and retractable segmented semiconductor detector of transmitted electrons – STEM III. For analysis of characteristic X-rays, the Energy Dispersive X-ray detector Octane Elect Super (EDAX, Ametek, USA) is mounted. Electron Backscatter Diffraction (EBSD) can be measured by Hikari camera (EDAX, Ametek, USA). Visible, near-infrared and ultraviolet light can be captured by cathodoluminescence detector Mono CL4 Plus (Gatan, USA). For examinations at lower than room temperature, the standard stage of the microscope can be changed to cryo-stage cooled down by liquid nitrogen (minimum temperature of a sample is $\sim -150^\circ\text{C}$). An anticontamination shield and vacuum cryo-transfer port (corresponding to the transfer shuttle VCT100, Leica Microsystems, Austria) is mounted on the microscope chamber permanently.

Focused ion beam/scanning electron microscope Helios G4 HP

The microscope (shown in Fig. 6.1 B; ThermoFisher Scientific, USA) has the SEM parameters similar to above mentioned SEM Magellan (chamber, Elstar Electron Column with UC+ Technology, in-column ICD and Mirror detectors) plus it has in-chamber ICE detector. It is equipped with gallium Tomahawk ion column with fast beam blanker and lift-out needle EasyLift EX

NanoManipulator. The sample may be covered by platinum by gas injection system of a platinum precursor. The transmitted electrons may be captured by retractable STEM III detector and pixelated T-Pix STEM detector. Chamber cleanliness is ensured by CryoCleaner and integrated plasma cleaner.

Scanning electron microscope JSM 6700F

The microscope (shown in Fig. 6.1 C; JEOL, Japan) is the oldest used microscope, but it still provides excellent resolution of 1 nm at the beam energy of 15 keV (2.2 nm at 1 keV). It is operating in low magnification mode, where no magnetic field is on the sample (max magnification 10,000 ×) and high magnification mode, where a sample is immersed in the magnetic field (max magnification up to 1,000,000 ×). The microscope is equipped with detectors of secondary electrons in the chamber and in electron column, scintillation BSE detectors TS6114 (AutraDet, Czech Republic) and Rebeka (Crytur, Czech Republic) and EDX detector Inca 350 (Oxford Instruments, United Kingdom). Home-made scintillation single electron counting STEM detector is mounted at this SEM. It was developed at ISI Brno in cooperation with Crytur company. It is based on plastic scintillator BC-404 (Saint-Gobain Crystals, Netherlands) with the peak full width at half maximum of 2.2 ns, the rise time of 0.7 ns, the decay time of 1.8 ns and emission maximum at the wavelength of 408 nm. The scintillator is supplemented by photomultiplier R1828-01 (Hamamatsu Photonics, Japan) with wavelength working range from 300 to 650 nm, amplification of 2×10^7 and time response 1.3 ns. For more details about the STEM detector see *Chapter 7: Quantitative imaging using scintillator based STEM detector*.

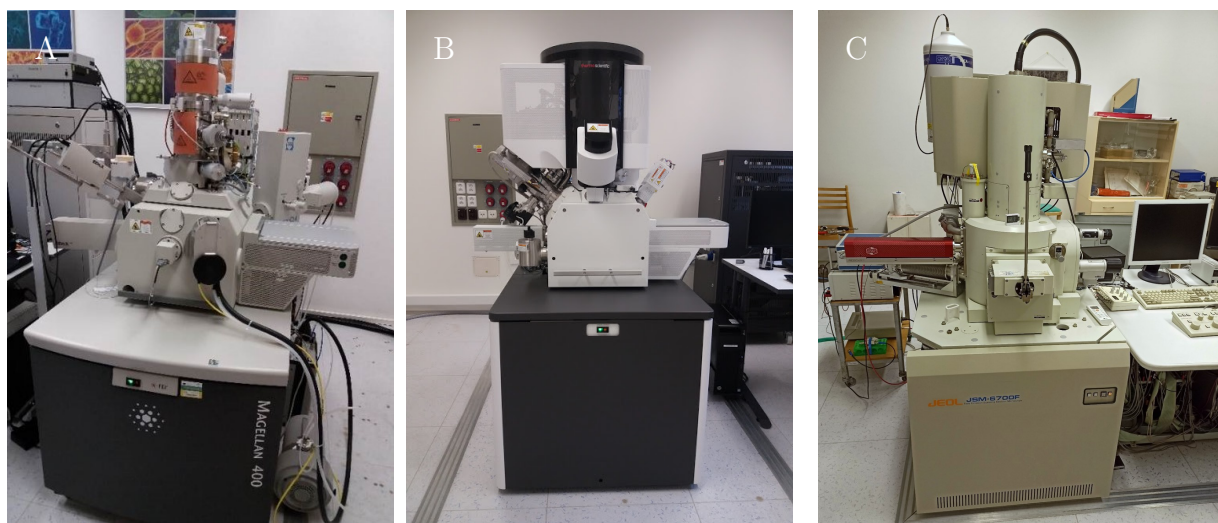


Fig. 6.1: The main instrumentation used in a project: (A) SEM Magellan 400L, FEI; (B) FIB-SEM Helios G4 HP, ThermoFisher Scientific; (C) SEM JSM 6700F, JEOL

7 Quantitative imaging using scintillator based STEM detector

The developed method of quantitative STEM imaging using home-made detector (model of the detector is shown in Fig. 7.1) is based on simultaneous capturing of an investigated sample image and information about actual probe current (primary beam current is changing by decreasing of emission current; Fig. 7.2 A – reset brings step changes).

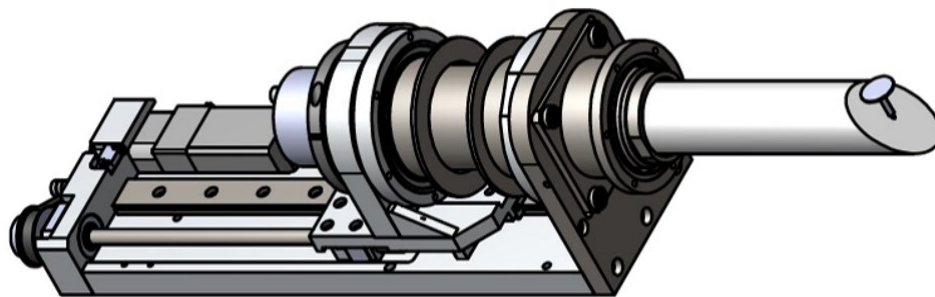


Fig. 7.1: Model of two inch scintillator based STEM detector.

This information can be used for normalisation of the captured data in postprocessing and elimination of the beam current drift caused systematic error. The detector is designed as single electron counting and so very fast and sensitive plastic scintillator was used. This approach has the limitation in the usable probe current range (< 2 pA), because the scintillator is highly beam current sensitive and it is necessary to separate individual light peaks from the scintillator. Construction and manufacturing of mechanical parts of the detector (for the SEM JSM 6700F, JEOL) were done in collaboration with Crytur company (Czech Republic). The calibration process starts with measurement of the actual probe current at different microscope settings (extraction voltage 2, 5 and 10 kV, beam size 1-15) by installed Faraday cup. Direct measurement is possible only when the electron probe is focused into the Faraday cup, but not in case of real sample imaging. The actual beam current is monitored by recording the current on the condenser aperture, which is in a constant ratio to the probe current (Fig. 7.2 B).

Two signals are simultaneously recorded by external scanning unit DISS 5 (Point Electronic, Germany) during the experiment. The first one is digital signal coming from the fast amplifier and discriminator giving the number of electrons in each pixel of the captured image (STEM image). The second one is recording current on the condenser aperture by using the analogue input of the external scanning unit. The signal is converted into the digital image with the same size as the image of investigated sample (the input is calibrated by gain and offset estimation for each analogue preamplifier/channel pair by capturing the signals with known properties provided by a signal generator). The digital intensity in the captured image can be also assigned to specific analogue signal levels and it gives information about time-resolved probe current.

The signal from the photomultiplier tube (R1828-01, Hamamatsu Photonics, Japan) is amplified by a preamplifier and processed using a discriminator. We found an optimal voltage on the photomultiplier as 1600 V, where the signal to noise ratio was measured and its maximum value was chosen (the result is the same for beam current of 70 fA and 0.95 pA). The threshold on the discriminator was estimated from the best signal to noise ratio (amount of counts on pixel

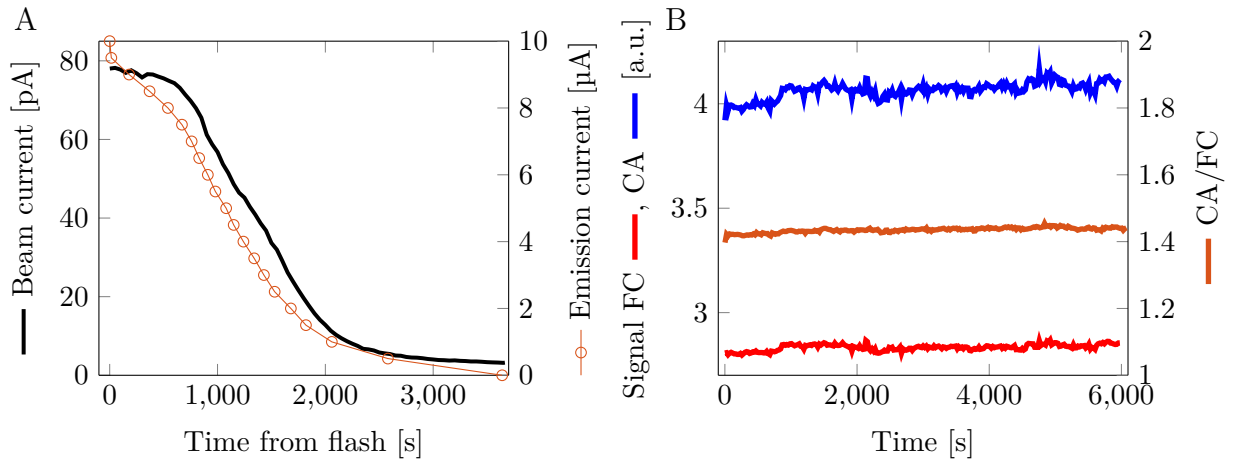


Fig. 7.2: (A) Time dependence of beam and emission current after flash. (B) Long term ratio of condenser aperture (CA) and Farraday cup (FC) measured currents.

while beam on divided by the amount of counts on pixel while beam off). The threshold was changed in the whole available range and the actual ratio was estimated. Maximum was found in case of 34.5 counts in $10 \mu\text{s}$ against 0.1 counts. By taking into account the beam current of 0.95 pA , the amount of 5.93×10^6 electrons is impacting the detector every second. The amount of electrons divided by the used dwell time gives 59.3 electrons per pixel. Detection efficiency is then given by ratio $(34.5 - 0.1) / 59.3 = 0.58$. The resulting efficiency of 58% is influenced by a shadow caused by the Farraday cup mounted in the middle of the detector (the detector was slightly pulled out from the optical axis). The resulting numbers given by the discriminator are then processed by the external scanning unit into an image. Due to the counting of individual electrons, the captured data does not need to be normalised to the detector response as it is necessary in the use of non-counting STEM detector. Our detector is in working state and gives satisfactory images at low magnification as demonstrated in Fig. 7.3.

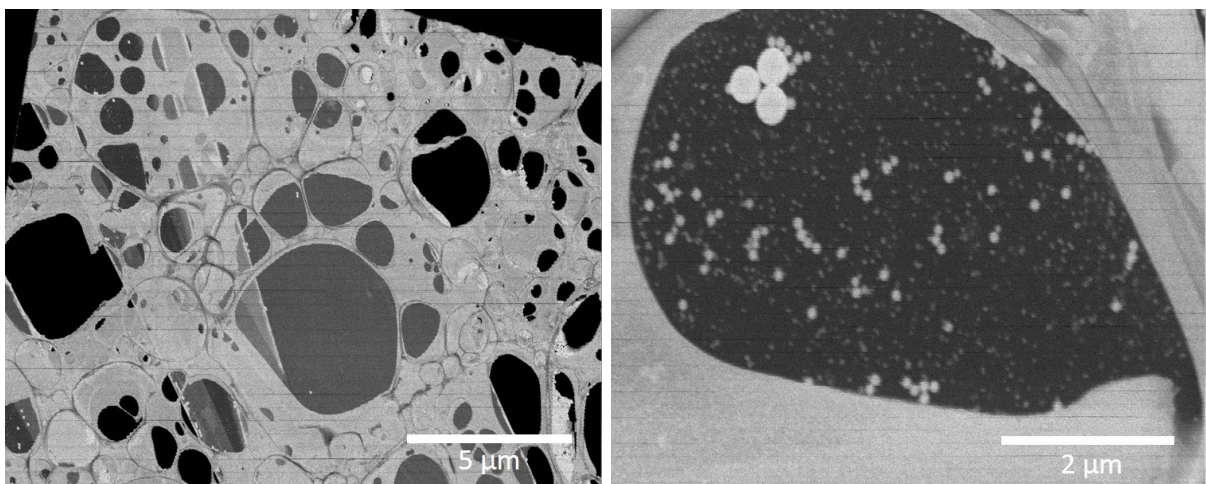


Fig. 7.3: Test sample of latex nanospheres with diameter from 10 up to 400 nm imaged by home-made STEM detector in low magnification mode.

The images are taken before geometrical calibration of an external scanning unit on a sample with known geometry – TEM grid. The image distortion is visible on a non-rectangular shape of the grid mesh. The use of the detector for a real sample investigation is limited due to complicated primary beam electron trajectories in a magnetic field (captured images are of high quality – Fig. 7.4 – but there occurs a problem with Monte Carlo simulations) and the impossibility of magnetic field closure at this type of microscope. We tried to overcome the problem with high magnification mode by using low magnification mode, where no magnetic field is around the sample. Unfortunately, the maximum magnification in this mode is $10,000\times$, which is not enough for most of the samples. We used an external scanning unit for finer scanning to obtain images at higher magnifications. The result is shown in Fig. 7.5. Unfortunately, focus control of the microscope is stepping and precise focusing is very time consuming and inaccurate. Due to the above-mentioned issues, the concept of fully calibrated qSTEM using SEM JEOL JSM 6700F was suspended until solving the problem (either by finding a way how perform alignments in the low-magnification or by closing the field above the sample). The experience gained through the development and testing of the detector is used in one-inch variant designed for its using in SEM Magellan 400L, which enables imaging in field-free mode with magnification up to $1,000,000\times$. This version of a fast scintillator home-made STEM detector is currently under construction.

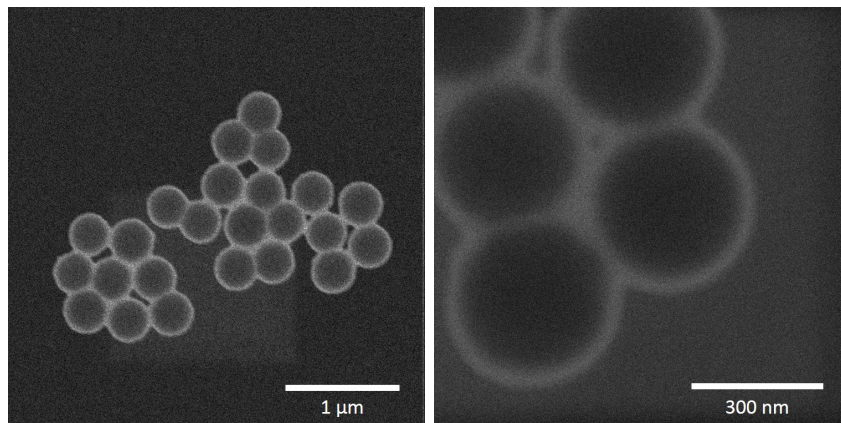


Fig. 7.4: Latex nanospheres with a diameter around 400 nm captured by the home-made STEM detector in high-magnification mode.

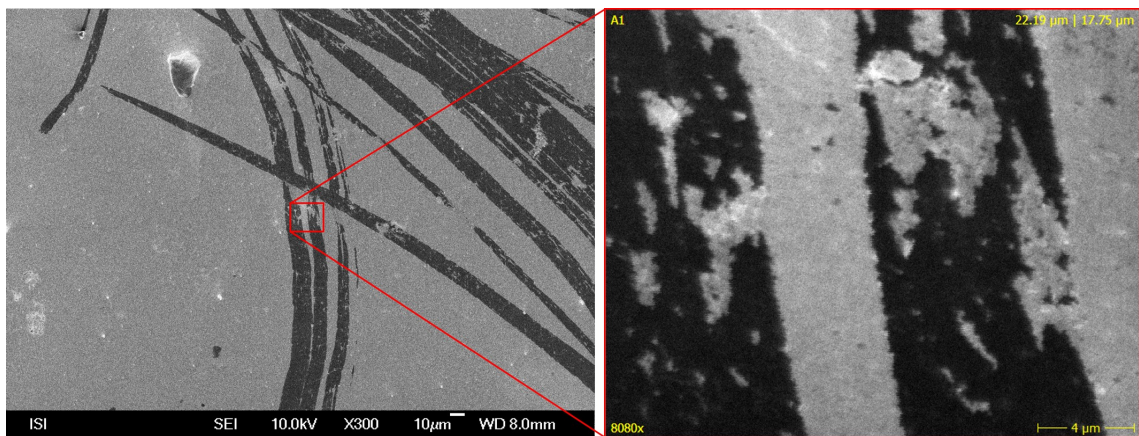


Fig. 7.5: Increasing of maximum magnification by external scanning unit.

8 Quantitative imaging using semiconductor annular STEM detector

All quantitative imaging using semiconductor annular STEM detector is done with the detector STEM III which is divided into seven independent segments (BF, DF1-DF4 and two HAADF parts as schematically shown in Fig. 8.1). Unfortunately, it is not possible to acquire images from all segments independently and simultaneously, because the SEM Magellan is equipped with six independent channels of multipliers and allows only four images to be recorded. The multipliers are not directly assigned to individual segments and they are changing in carousel. Although their characteristics are very similar, some small deviation may occur between them. As the result, the multiplier used for example with BF segment in experiment A can be different than the multiplier used for BF segment in experiment B. The captured signal would be than different even at the same detector and multiplier settings.

At the beginning of each imaging session, it is necessary to choose the segments which carries the most important information about an investigated sample (it is possible to combine individual segments in one window).

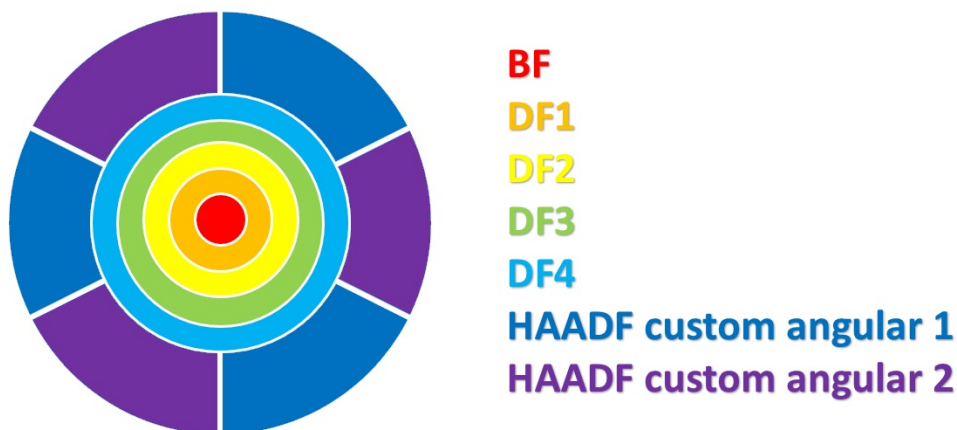


Fig. 8.1: Schematic drawing of individual STEM III detector segments layout.

8.1 Calibration of STEM detector and primary beam current stability

It is not necessary to know the exact value of primary beam current, but its fluctuation in time (drift of actual and set probe current is incorporated in calibration images as well), which is in our case measured by the Faraday cup mounted in microscope chamber and connected to picoammeter Keithley 6485 (Tektronix, USA). Time dependency of beam current in time window of 120 s (roughly the real measurement time of one imaging session) is shown in Fig. 8.2 A. The nominal beam current was set to 1.6 pA. The mean value 1.36 pA with a standard deviation of 0.04 pA was estimated. In the case of long term measurements (3000 s; Fig. 8.2 B), the mean value is the same (1.36 and standard deviation 0.05 pA). The results of short and long term measurements are very similar with no trend (increasing or decreasing in time) in comparison with the cold-field emission gun SEM (Fig. 7.2). The sampling frequency of 2.5 Hz was used in both cases.

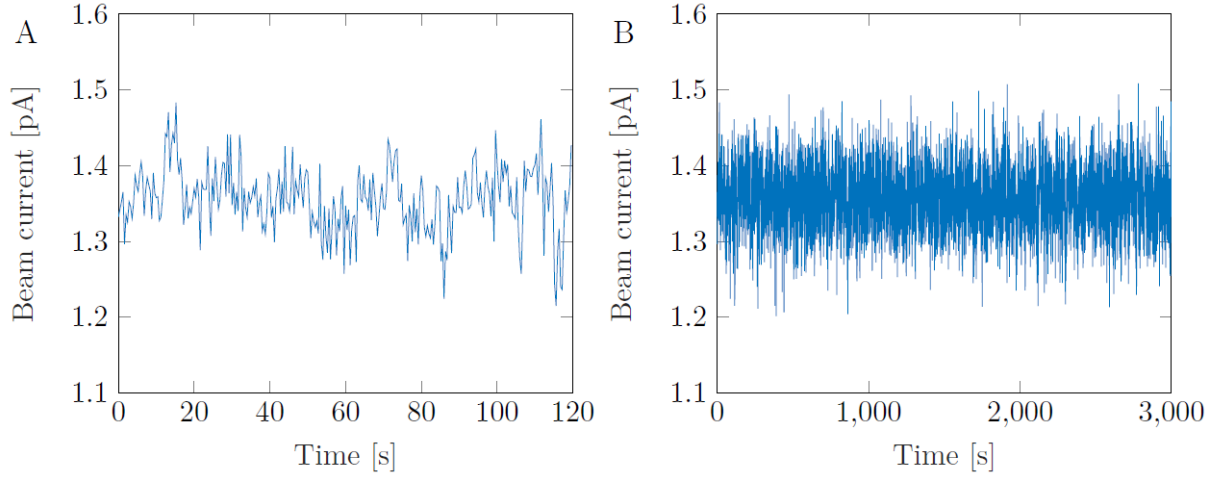


Fig. 8.2: Primary beam stability with a nominal probe current of 1.6 pA in the time range of (A) 120 s and (B) 3000 s.

8.2 Determining the accuracy of qSTEM

Appropriate calibration is one of the crucial parts of the method. Even a small error or inaccuracy in detector response to electron beam — either blanked or full — brings significant error into the thickness determination. To compare individual detector segments and their accuracy we used a sample with a known thickness in each point – a latex nanosphere (Fig. 8.3 A, B) with a nominal diameter of 616 nm (S130-6, Agar Scientific, United Kingdom). We measured the diameter of 583 nm in case of the particle shown in Fig. 8.3. The accurate diameter was detected at each particle during the image processing. The MC simulation was performed in CASINO software [65] with appropriate settings (energy 30 keV, 200,000 e per point, the total and partial cross-section taken from Elsepa database, supporting thin carbon layer was taken into account).

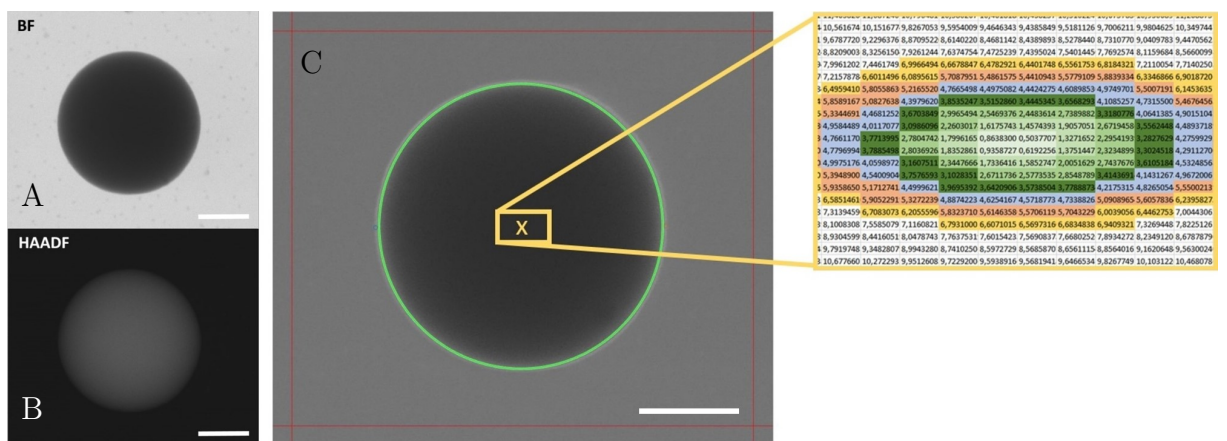


Fig. 8.3: Latex nanosphere images captured simultaneously in BF (A) and HAADF (B). (C) Calculation of the rotationally averaged signal (detected sphere – green, control of the integrity of the particle – red lines and detected centre – enlarged area; the distance of individual pixels from the detected nanosphere centre). Bar 200 nm.

For the noise limitation and easier comparison of the results, the centre of the nanoparticle is detected and then a rotation averaging is performed (Fig. 8.3 C). In this step, a distance of each pixel to the centre of the sphere is calculated. Then the pixels with distances in the chosen range are averaged. The advantage of this method is the absence of the interpolation error. However, a small amount of pixels in the middle of the particle causes significantly higher inaccuracy given by higher noise influence. Unfortunately, not all used segments gave us the same results. Both BF and HAADF segments brought results which corresponded very well with the character of the sample (Fig. 8.4) with maximum error around 10%. BF showed a little bit higher, and HAADF brought a little bit lower thicknesses than those given by the geometry of the sample.

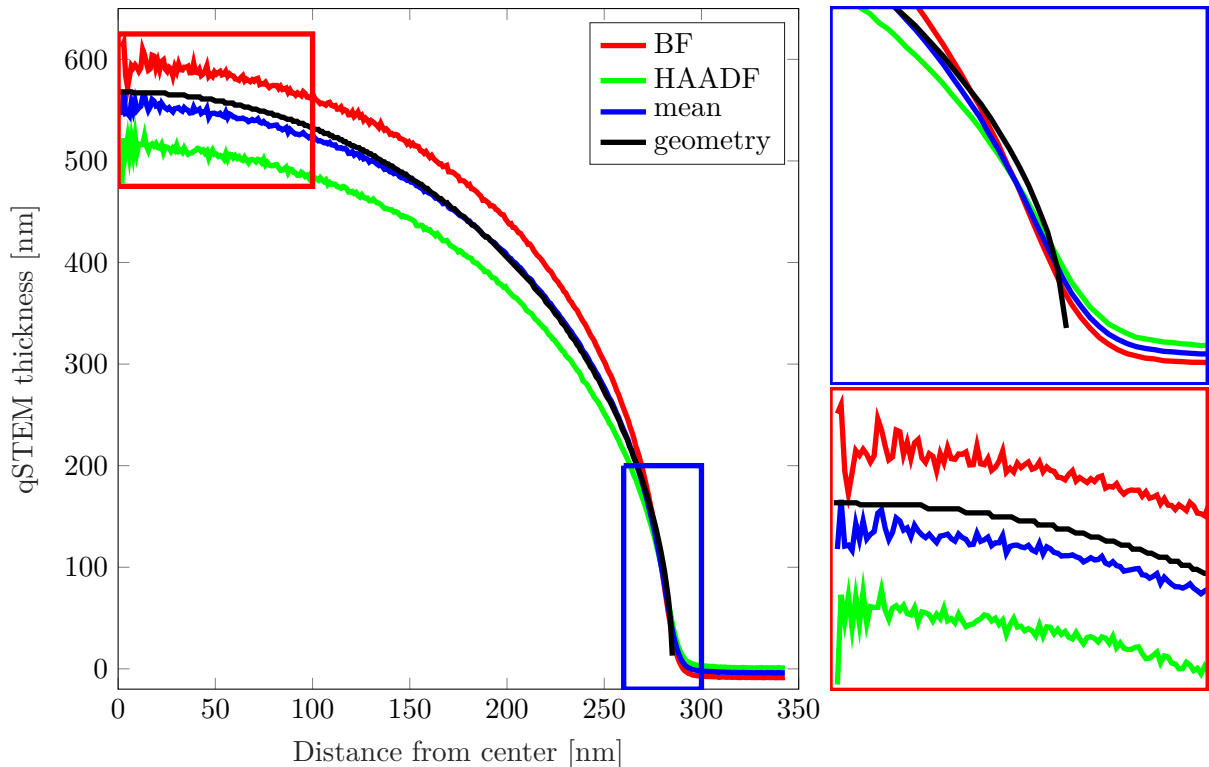


Fig. 8.4: Thickness of the sample estimated by quantitative STEM imaging in two different detector segments together with their mean and geometry. The problematic areas are highlighted in enlarged sections (low thickness region in blue and high thickness region in red).

However, it is possible to improve the accuracy of the method by averaging the curves. In case of the "mean" curve, the accuracy is better than 2% in nearly all examined range of thicknesses. High errors (shown in Fig. 8.5) in the range of thicknesses under 100 nm are caused by inaccurate detection of a nanosphere diameter, imperfect spherical shape and wedge shape MC simulation body.¹

¹The text and results described in this section are based on abstracts and posters presented at NANOCON 2018 Brno (extended abstract in [175]), Mikroskopie 2019 Lednice ([176]) and MCM 2019 Belgrade [177]).

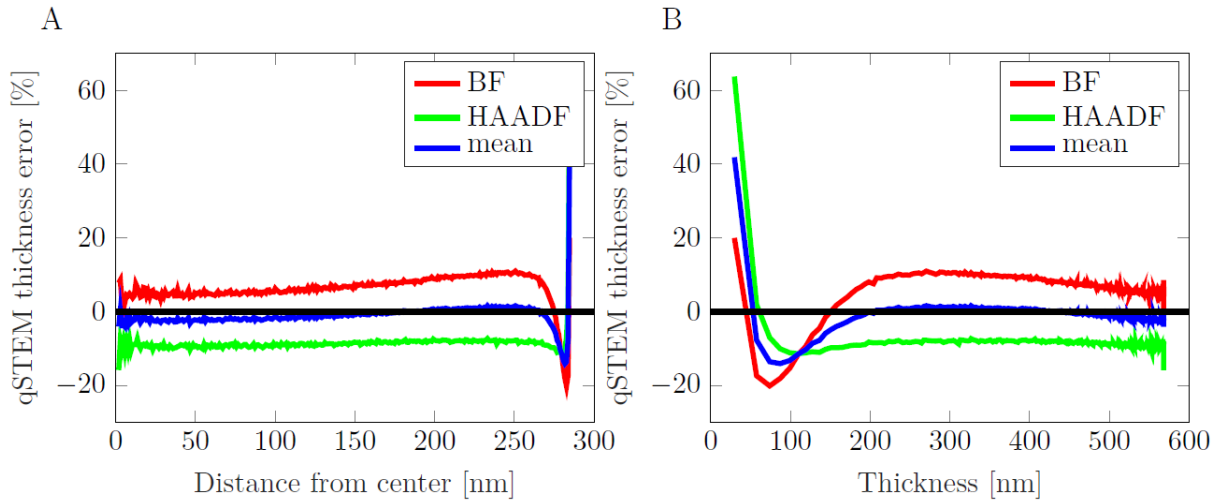


Fig. 8.5: Relative qSTEM thickness error dependency on the distance from the centre of the nanosphere (A) and on the local geometrical thickness (B).

8.3 Influence of out-of-axis-detector

The used STEM detector is a retractable device and because of this reason, the actual position is slightly different after each inserting and retracting. Even mechanical alignment of STEM detector to the optical axis cannot be done ideally. It is possible to determine the actual position of STEM detector from its image. In case of perfect position, the centre of the imaged area will be in the centre of the imaged BF segment of the detector. We estimated the distance of the STEM detector centre from the optical axis as 0.058 mm (estimation is based on the calibration image and known geometry of pole piece, sample plane and detector inside the SEM chamber). The aim of this section is the estimation of the influence of such deviation to the results of qSTEM thickness determination. The influence of such systematic error to final thickness is possible to estimate by detailed analysis of the Monte Carlo simulation results. We used MC software MONCA2 because of the fully open output design (start of the simulation with used parameters is shown in Lis. 8.1).

Listing 8.1: Start of simulation in software MONCA2

```

1 MONCA2_1('CH',1.05,30,1000,0.76,1,200000,'A')
2 % formula of latex
3 % density [kg/m3]
4 % energy of primary electrons [keV]
5 % simulated thickness [nm]
6 % electron probe semiangle [mrad]
7 % diameter of electron probe [nm]
8 % number of simulated electrons
9 % type of simulation

```

Results of the simulation are a data structure with information about properties of each scattering event (position in x , y , z , angles Θ and X , energy decay ΔE). For each simulated electron the distance from the optical axis (in detector plane) was calculated. The results of MC simulation (for parameters displayed in Lis. 8.1) are shown in Fig. 8.6 A – histogram of distances and Fig. 8.6 B – control of the azimuth angle X . The number of electrons captured by STEM detector segments of interest (BF and HAADF) was computed according to the distance misalignment range from 0 to 5 mm. As shown in Fig. 8.7 A,B, the measured deviation of 0.058 mm do not make a significant change in the simulated signal. High errors will be introduced at deviations higher than 0.2 mm.

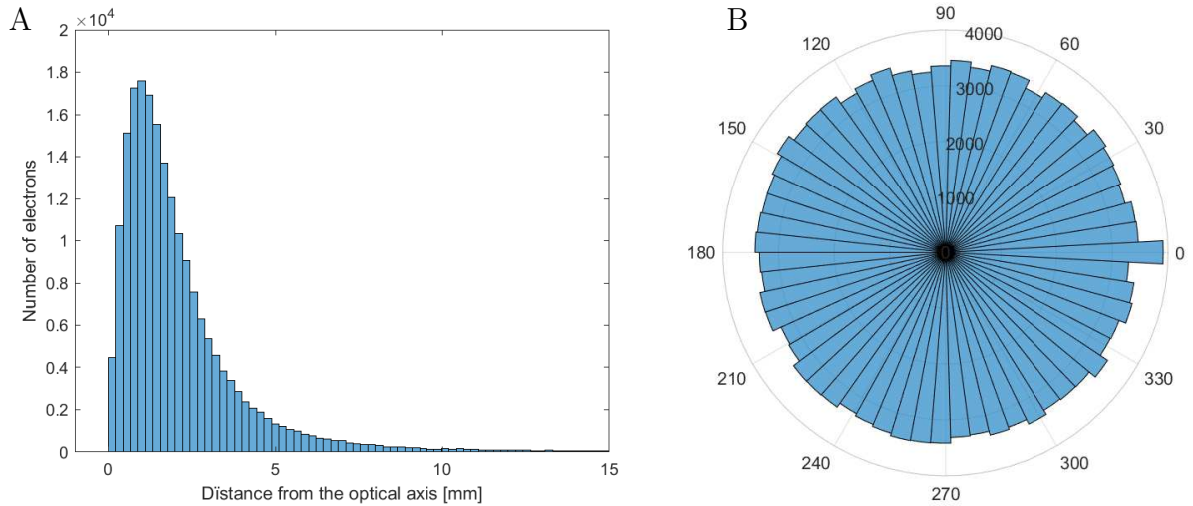


Fig. 8.6: The results of MC simulation. (A) Histogram of electrons impacted the STEM detector plane according to distance from the optical axis. (B) Control of the azimuth angle uniformity of simulated electrons.

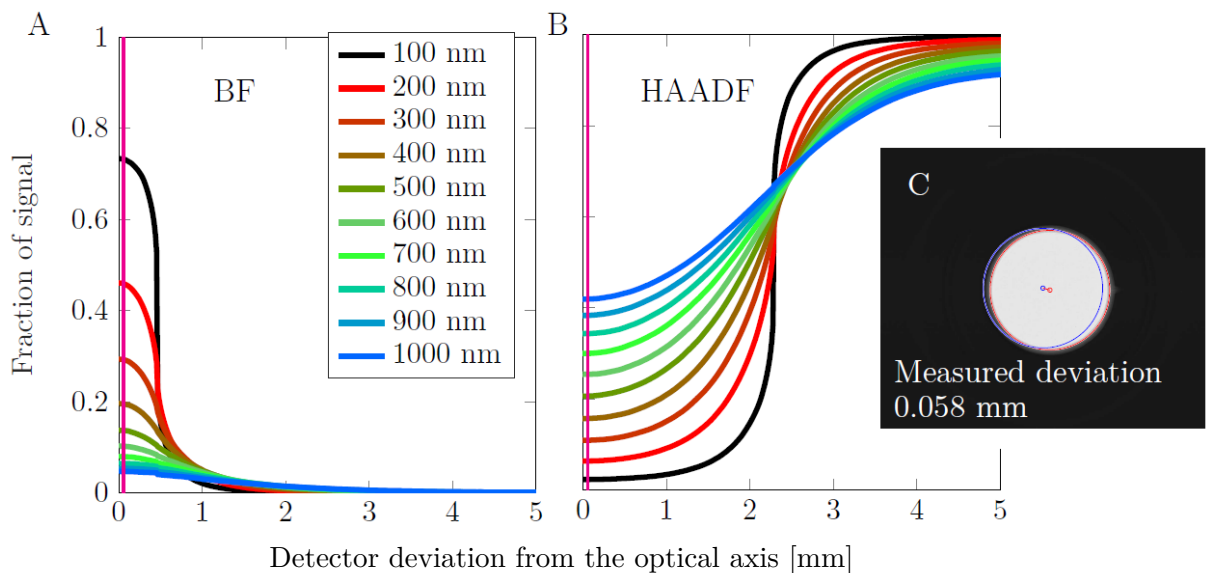


Fig. 8.7: Change of BF (A) and HAADF (B) signal in considering detector-axis deviation. (C) Analysis of STEM detector deviations from the optical axis. Circles show the position of BF segment in case of the STEM detector on the optical axis (blue) and actual position (red). The measured deviation is highlighted in graphs (A, B) by the magenta line.

8.4 Application: Beam induced mass-loss of embedding epoxy resin

In the presented paper R. Skoupy, J. Nebesarova, M. Slouf, and V. Krzyzanek. Ultramicroscopy Quantitative STEM imaging of electron beam induced mass loss of epoxy resin sections. *Ultramicroscopy*, 202(March):44–50, 2019. doi:10.1016/j.ultramicro.2019.03.018 (full text of the paper in the annexe B.1) the detector calibration, image acquisition, data processing and visualisation were done by the author of the thesis.

qSTEM was used in the examination of epoxy resin EMbed 812 (Electron Microscopy Sciences, USA) and their properties under the electron beam. The study was done in collaboration with Laboratory of electron microscopy of the Biology Center of the Academy of Sciences in České Budějovice, where preparation, slicing and mounting of the thin slices on the TEM grids was done. We focused on several factors which can have an influence on the stability of the sections under the electron beam and on the quality of the images of samples embedded in this type of resin respectively. There are available studies dealing with the degradation of embedding media under the electron beam but the applied acceleration voltage is much higher than the voltage used in low-voltage STEM (dedicated STEM at 80 and 100 kV [179], energy-filtered TEM [180]). There is a lack of studies dealing with energies used in SEMs.

Resin EMbed 812, used in this study is a successor of the resin Epon 812 – the most used embedding medium in the area of TEM of biological samples. There are many types of embedding media such as methacrylate, melamine, polyester or epoxy resins. Previously mentioned EMbed 812 belongs to the latter group [181, 182]. EMbed 812 is suitable for embedding of both plant and animal tissue in a range of hardness from soft tissues to bones. It has a convenient combination of properties: fast penetration, high contrast, easy cutting, satisfactory staining for light and electron microscopy and high stability under electron beam [183]. Preparation of testing samples was done accordingly to data sheet in the middle hardness with the amount of DMP-30 0.77 ml. Other ingredients are in Tab. 8.1.

Tab. 8.1: Composition of possible variants of embedding epoxy resin EMbed 812 [19].

	Soft	Middle	Hard
	[ml]	[ml]	[ml]
EMbed 812	20	20	20
DDSA	22	16	9
NMA	5	8	12
DMP-30	0.70 - 0.94	0.66 - 0.88	0.62 - 0.82
BDMA ^a	1.18 - 1.40	1.10 - 1.30	1.00 - 1.20

^apossible replacement of DMP-30

The polymerization was carried out in casting moulds for 48 hours at 60 °C. The ultrathin sections were cut to 30, 60 and 100 nm thickness on a UCT ultramicrotome (Leica Microsystems, Austria) equipped with a diamond blade (Diatome, Switzerland). The sections were floated onto water and placed on a 300 mesh TEM grid (Electron Microscopy Sciences, USA) without the use of a supporting film. Mass-loss measurements were performed in all cases by the same procedure. The images of the sample were taken repeatedly from the same location at a magnification of 100,000 × (field of view 1.024 × 0.884 μm). The resulting series of images (typically 50) were

then further processed. The processing is schematically illustrated in Fig. 8.8. in order to reduce the random component caused by the inhomogeneous slice thickness, three measurements were taken from different parts of the sample, the results of those three measurements were then averaged.

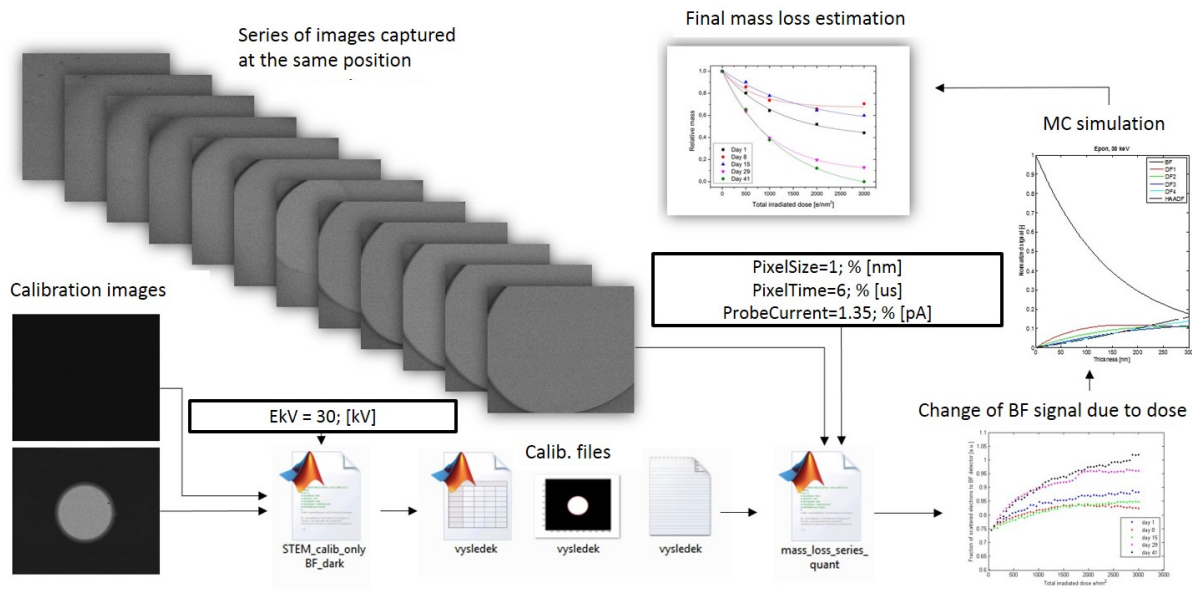


Fig. 8.8: Scheme of mass loss estimation by qSTEM.

The cumulative dose applied to a sample is given after the determination of the order of the image in series S as $D = (StI)/(a^2e)$, where t is the dwell time, I the beam current, a the pixel size of the recorded image, and e the elementary charge of an electron. Mass-loss information is obtained from normalised BF signal using Monte Carlo simulations of electron scattering in the MONCA package [16]. The procedure is analogous to the measurements published in [99].

Dependence on ageing

The dependency of the time-scale sensitivity was examined in a period of 40 days. Individual measurements were performed on slices 1, 8, 15, 29 and 41 days old (days from cutting off the epoxy block). The results show that the beam sensitivity and corresponding mass-loss rate is not the same in the whole period. The sensitivity is decreasing from day 1 with a minimum between day 8-15. After that, the trend is reversed and the sensitivity is increasing. In the most stable phase, the BF signal for 30 nm thick slices after irradiation by the dose of 3000 e/nm² is still at the level of 0.82, but at the day 41, the slice is burned through at the dose of 2880 e/nm². This indicates a change in properties, which may have a critical influence on the quality of images taken of the older slice. An interesting point is that the properties of the cuts deteriorate only after cutting – it is possible to long term storage the blocks without their unwanted changes in durability under the electron beam. The sensitivity of slices prepared from the freshly polymerised block is higher compared to slices prepared from 6 months old block with the same composition. The time-dependent sensitivity of an old block shows similar dependency but with much smaller dispersion than the new one. **The recommendation is to let the blocks mature properly in the desiccator and then observe around the tenth day after slicing.**¹

Influence of carbon layer coating

Slices with a thickness of 30 and 60 nm were tested together with one-side or both-side coating by an evaporated 3 nm thick carbon layer. Even one-side carbon layer is able to reduce the mass-loss rate, which changes to nearly linear dependence on the irradiated dose. Both-side carbon covering gives even better results. It is almost unimportant, when the carbon layer is prepared, the results are very similar and carbon covering directly before imaging has a stabilisation effect too.¹

Influence of beam current

Change of mass-loss rate was tested by increasing the primary beam current from 1.6 to 6.3 and 13 pA (nominal values). We can say, that mass-loss is mainly dependent on accumulated dose, but there is a significant change in case of non-carbon covered slice.¹

Influence of staining

For our study, we used resin sections with thickness 30 and 60 nm. Measurement was performed the second day after their preparation by the ultramicrotome. Some slices were stained with uranyl acetate for 30 minutes on the upper side. As seen in Fig. 8.9 A, the normalised BF signal has a similar trend with nearly linear tendency for both thicknesses of the slices without staining; the curves are shifted for the different thickness. Mass-loss (Fig. 8.9 B) shows two groups of thickness independent curves. First one is a slice without staining, where at the total irradiation dose of 3000 e/nm² still remains 64 % of the initial mass in the case of 30 nm and 51 % for 60 nm slice, respectively. However, the slices with staining are much more sensitive to the electron beam, where the curves in BF signal dependency have an exponential shape. Corresponding mass-loss shows the same exponential behaviour in both thicknesses. They remain only 21 % of initial mass for both 30 and 60 nm slices at the same dose of 3000 e/nm². We observed higher sensitivity of stained EMbed 812 thin sections under the incident electron beam. We found a change of 43 % mass for 30 nm and 30 % for 60 nm slices. This limits the usable dose for imaging by the low-voltage STEM (for energy of 30 keV) because stained sections are more susceptible to burn-out than the pure ones.²

Influence of plasma cleaning

As seen in Fig. 8.10 A, the normalised BF signal has a similar shape for both thicknesses (60 and 150 nm) of the slices without plasma cleaning; the curves are shifted only because of the different thickness. However, slices treated with the plasma cleaner show higher sensitivity to the incident electron beam with rapidly increasing BF signal; Fig. 8.10 B shows the remaining mass. At the total irradiation dose of 3000 e/nm² there still remains 89 % of initial mass for the 150 nm slice and 70 % for the 60 nm slice, respectively. However, the slices cleaned by plasma cleaning are much more sensitive to the electron beam, with 55 % remaining for the 150 nm slice and local destruction for the 60 nm slice. It shows contradictory requirements of plasma cleaning (often necessary to prevent the contamination originating from imperfect chamber vacuum)

¹Results described in this subsection were presented in talk at MCM 2015 Eger, abstract in [184] and published in [178] (full text in the annex B.1).

²Text of this subsection is an adapted version of a poster published as conference abstract at Microscopy & Microanalysis 2016 [7].

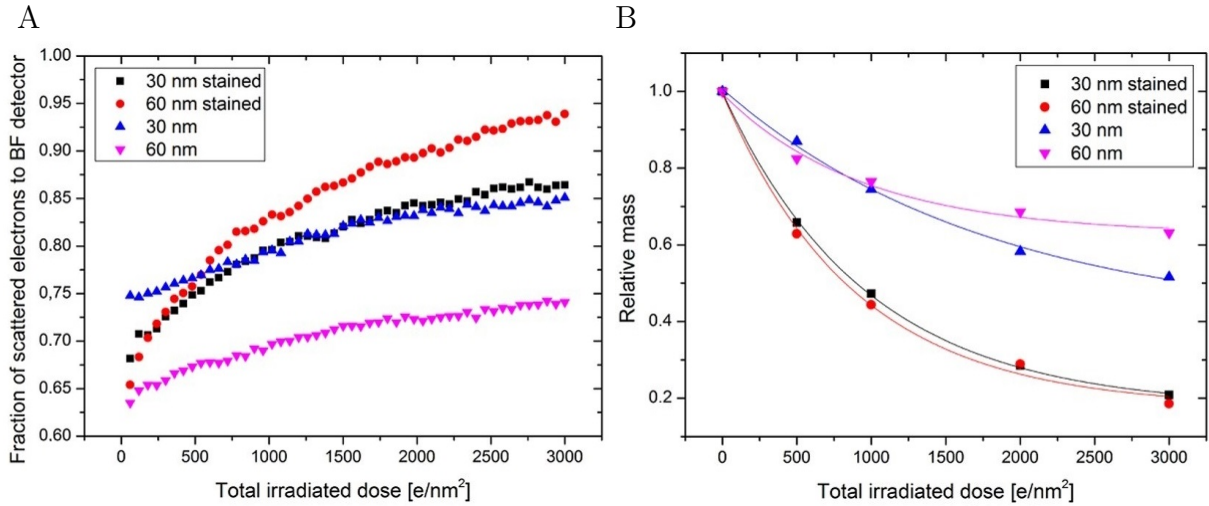


Fig. 8.9: The normalised BF signals (A) and recalculated relative mass (B) dependencies of the total irradiation dose on slices of various thicknesses with and without staining. Data were recorded on the second day. Taken from [7].

and maintaining the least possible damage to the sample during the observation itself. We estimated the influence of plasma cleaning time on the most sensitive sample: 30 nm EMbed 812 slice. As seen in Fig. 8.10 C, the effect of mass-loss is more significant at higher cleaning time. Changes of sensitivity to the electron beam are in cases of 20 and 40 s cleaning times very similar. Compared to the sample after 120 s, where the slice is burn-out at the dose, where at non-cleaned sample the BF signal remains on 0.82.³

Influence of temperature

In general, the mass-loss depends on the sample composition, and the contamination emerges mainly because of the poor vacuum in the specimen chamber of the SEM and the poor cleanliness of the sample surface. One of the possibilities to limit the damage is performing the STEM imaging at low temperature. We focus on quantitative investigations of the mass-loss of embedding media ultrathin sections at room temperature and at -130°C . The Fig. 8.11 A shows the change of the BF signal with respect to the total dose of electrons for EMbed 812 resin section of a thickness of 60 nm. Our results show that the mass-loss can be reduced by the cooling of the sample at relatively low doses as seen in Fig. 8.11 B. Note that mass-loss at the dose of $3000 e/nm^2$ is very similar for both temperatures. We assume that this is due to the gradual heating of the sample placed on the grid and its poor thermal conductivity.⁴

³Text of this subsection is an adapted version of a poster published as conference abstract at EMC2016 Lyon [8].

⁴Text of this subsection is an adapted version of a poster published as conference abstract at conference Mikroskopie 2016, Lednice [9].

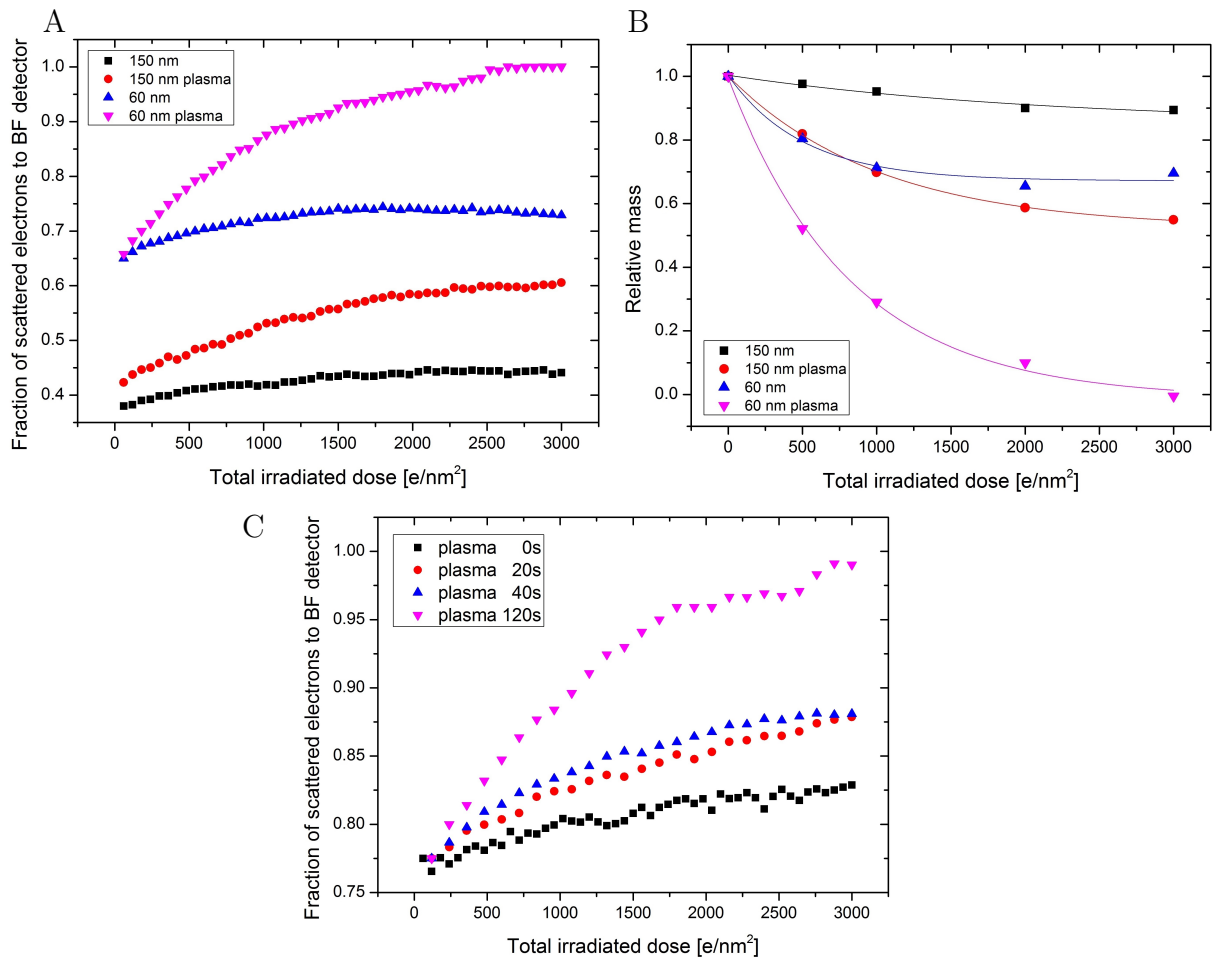


Fig. 8.10: (A) The normalised BF signals of 60 and 150 nm slices cleaned for 20 s. (B) Relative mass-loss dependencies on the total irradiation dose for 60 and 150 nm slices. (C) The normalised bright-field signals of 30 nm slices cleaned for different times. All images were recorded on the seventh day from cutting. Figures A and B are taken from [8].

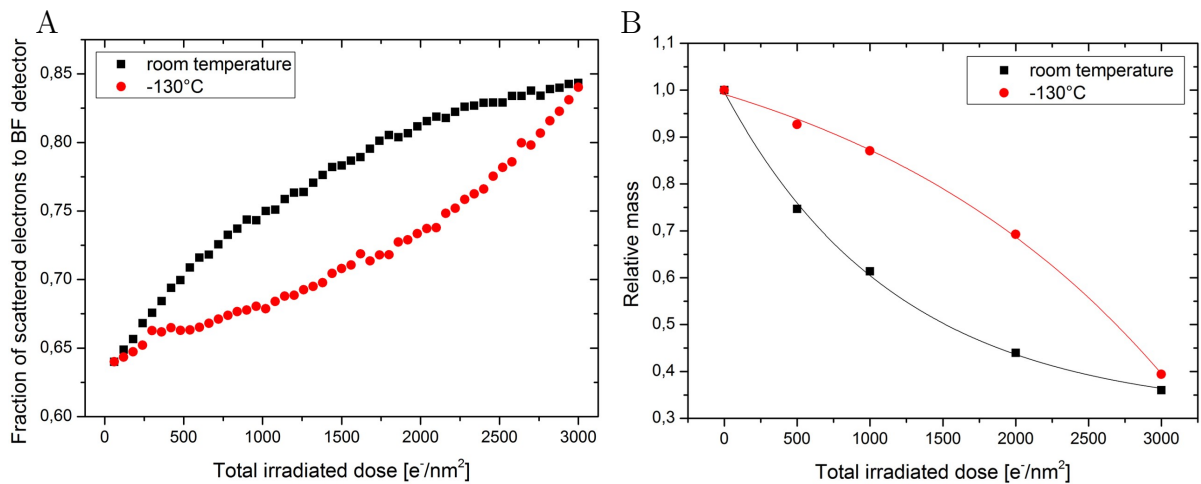


Fig. 8.11: The normalised BF signal (A) and relative mass-loss (B) dependencies of the 60 nm sections on the total irradiation dose for 60 nm slices at different temperatures. Taken from [9].

9 Quantitative imaging using pixelated STEM detector

The disadvantage of classical qSTEM is the need to calibrate the detector before the actual measurement. This makes impossible to use images that were taken with contrast and brightness setting adequate for imaging (using the whole range from black to white). We present a method how this disadvantage can be overcome and thickness evaluation can be performed even in the case of non-calibrated images. **The qSTEM changes to calibration-free with the use of 2D pixelated STEM detector.** Just setting to avoid under and over-saturation is needed. The method is based on a change of position of the maximum signal peak on the detector accordingly to sample thickness. Regular qSTEM technique uses detector calibration process as a bridge between a captured image of a sample and a computer simulation of electron scattering in a model sample with known geometry and composition [178, 130]. Unfortunately, this approach needs the capturing of two calibration images before each imaging session and it is probe current, beam energy and contrast/brightness dependent. We present a simple method for quantitative imaging using 2D STEM pixelated detector. In this case, no special calibration is needed. 4D datasets captured by the 2D STEM detectors are often used for many imaging and analytical techniques including thickness measurement in the field of material science and diffracting samples [141] or less frequently used for the analysis of amorphous samples [144]. The presented 4D-qSTEM method is based on shifting of the most common scattering angle to the higher angles with increasing sample thickness. As the primary electron beam is scanned over the sample (Fig. 9.1 A), individual scattering maps are captured for each beam position. Individual pixels are summarised by their distance from the centre (it is not rotational average but the sum of pixels at the same angle; Fig. 9.1 B) and plotted accordingly to its angle based on the detector/sample geometry.

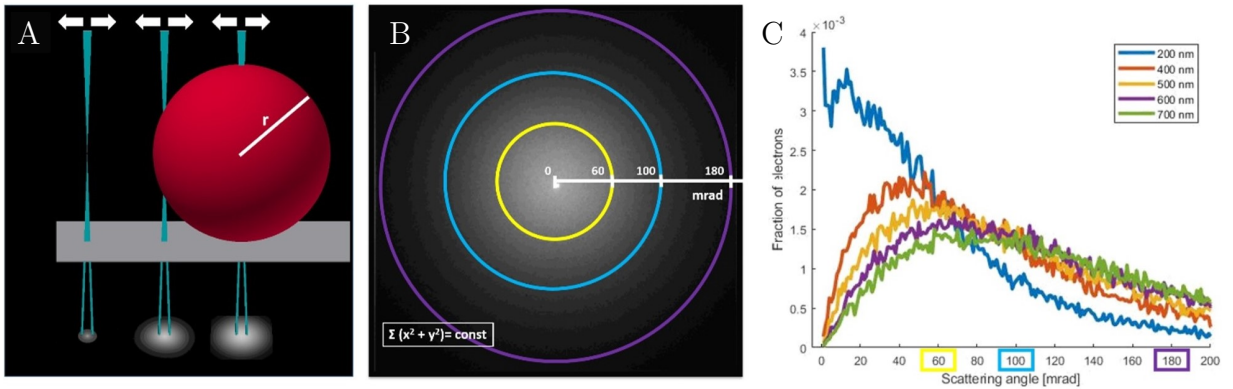


Fig. 9.1: Principle of 4D-qSTEM. (A) Test sample of a latex nanosphere with radius r is irradiated by scanning electron beam. Scattering patterns are captured independently for all beam positions. (B) Rotation sum of captured scattering pattern is computed and local dependency of the primary electron fraction is plotted accordingly to the scattering angle. (C) Simulated scattering angle dependency for several sample thicknesses. Note that the position of the peak is moving to the higher angles with increasing thickness.

The computational inputs of the method are similar dependencies based on the MC simulation of the electron scattering in a sample with known thickness, density and composition. The results of MC simulation are shown in Fig. 9.1 C. The most probable scattering angle is found at both parts and local thickness is estimated by finding the experiment-based angle

in simulation-based series. In the first experiments, latex nanospheres with a diameter of 575 nm (Fig. 9.2 A) were chosen as a model sample for their well-known dimensions in every point. From the comparison of the experimental scattering angle dependency and the simulation, the best match was found for the thickness 555 nm (Fig. 9.2 B). The error of estimation is around 3.5 % according to the measured nanosphere diameter, but this error could be caused by the imperfectly round shape of the nanosphere.

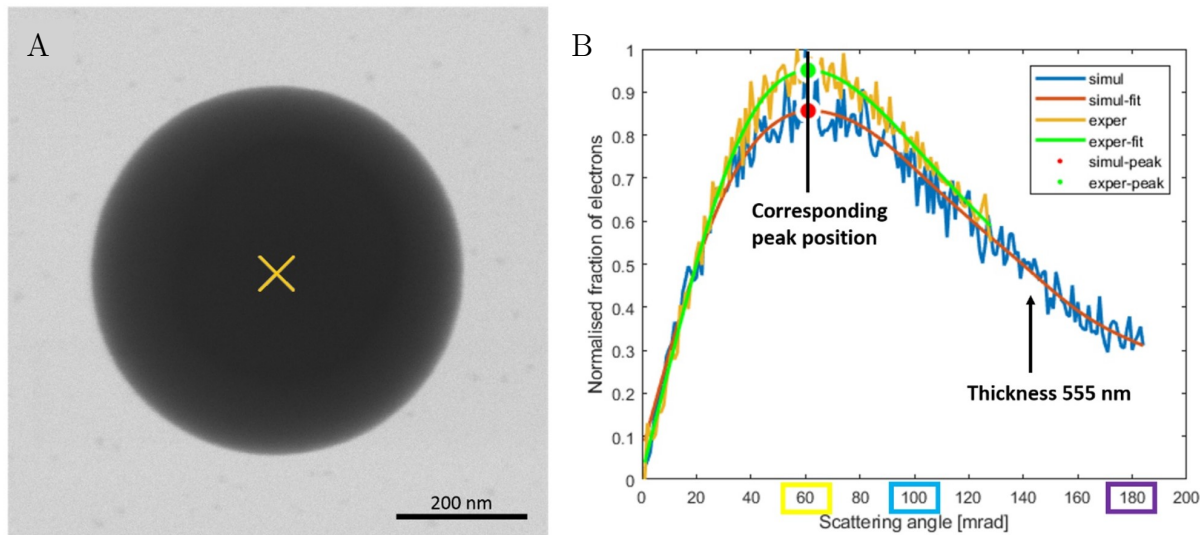


Fig. 9.2: (A) Test sample of a latex nanosphere with a diameter of 575 nm with the measured point in the middle of the sphere. (B) Comparison of scattering angle dependencies from the measured point and simulation for 555 nm thick layer of latex. Position of both peaks is at 61 mrad.

The main advantage of the method is that no previous detector calibration is needed. The usable range of the thicknesses, which can be determined, is given by the creation of detectable peak at low scattering angles for low thicknesses. In the case of latex, the measurable range is from 185 to 1000 nm. We assume that this method can enrich a number of methods based on pixelated STEM detectors and extend their use on amorphous types of samples.

9.1 Application: Thickness mapping of polymer blend PMMA/PS

All requirements for 4D-qSTEM-SRIP method (Summarised Radial Intensity Profile) are 4D data from pixelated STEM detector, knowledge of in-chamber geometry, and sample composition. The new calibration-less method was applied on two samples. For model monodisperse latex microspheres, the accuracy of the thickness estimation was better than 5 %. For the ultra-thin section of PS / PMMA polymer blend (where PS = polystyrene and PMMA = poly(methyl methacrylate)), we were able not only to differentiate the two chemically similar polymers without staining, but also to determine different mass-loss of the two polymers due to interaction with electron beam.

For more detailed results of the study see the paper R. Skoupy, M. Slouf, and V. Krzyzanek. 4D-qSTEM-SRIP: calibration-less local thickness estimation of amorphous samples. (*submitted*). Full text of the paper can be found in the annexe B.2. The original idea, image acquisition, data processing and visualisation were done by the author of the thesis.

10 Quantitative imaging using BSE detector

The technique of quantitative imaging as described for STEM is usable for BSE detectors as well, but there occurs a problem with precise calibration and response measurement of the BSE detector due to its position in SEM chamber because primary electrons cannot hit the BSE detector directly as in the case of STEM detector (Fig. 10.1 A).

The most of the studies use a comparison of a captured image with an image of known standard sample for its normalisation. We present a simple method for standard-less BSE detector calibration, which together with Monte Carlo simulation of BSE signal emitted from a sample with given geometry, brings a straight forward methodology of thin cover layer thickness measurement on substrates. The inability to irradiate the BSE detector by primary electron beam directly is overcome by the application of the electron mirror for reversion of electron trajectories as shown in Fig. 10.1 B.

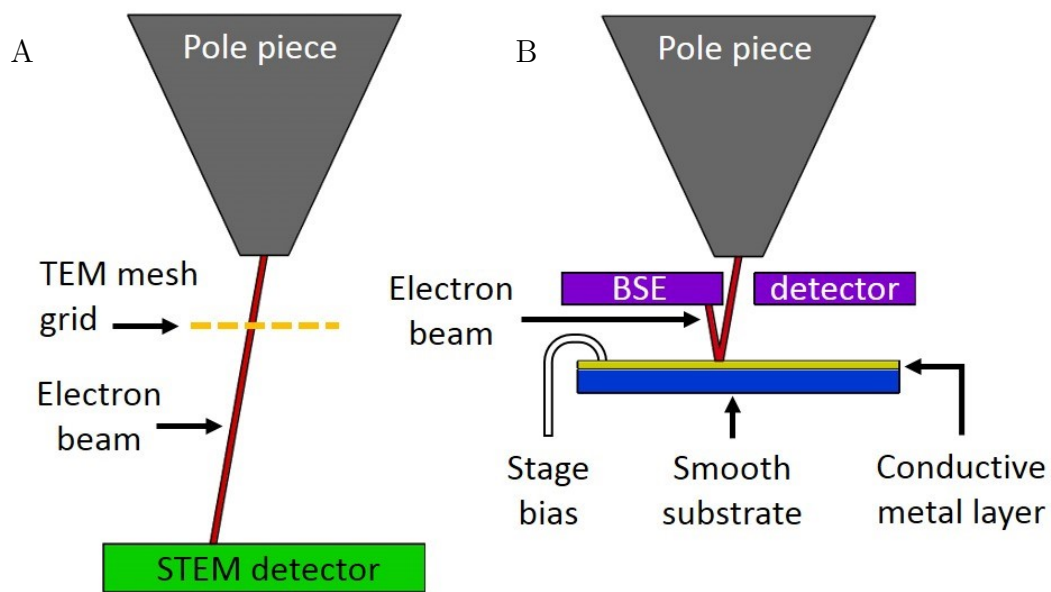


Fig. 10.1: Diagram of energy-dependent calibration of STEM detector (A) and BSE detector (B). Calibration of the BSE detector is performed by primary beam reflection on the biased sample instead of direct imaging used in case of the STEM detector. Taken from [10].

We tried several types of biased mirror samples (mica, Si wafer and glass) and the best results we obtained with gold-covered microscopy cover glass. Resulting selfie image of the BSE detector gives detector response to the full beam which is used as the upper limit for data normalisation of real sample images. The Fig. 10.2 A shows direct calibration images of the STEM detector and Fig. 10.2 B shows reversed calibration images of the BSE detector, respectively. The bottom limit is obtained from the image captured by the BSE detector when the electron beam is blanked. It is important to take care of over/undersaturation during the image recording.

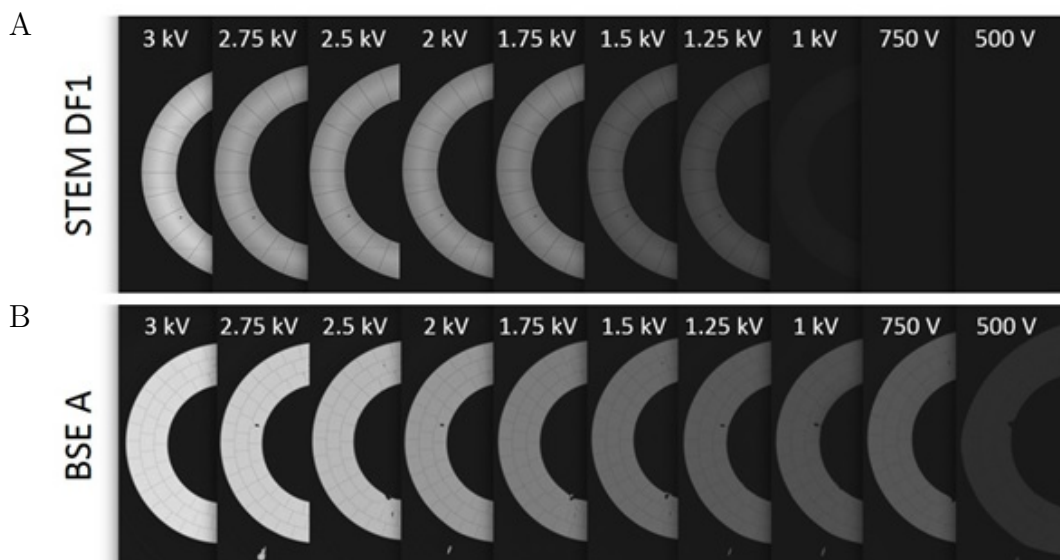


Fig. 10.2: Dependence of pixel intensity of the inner dark field segment DF1 of the STEM detector (A) and inner BSE detector segment A (B) on beam energy. Contrast/brightness settings were the same for the individual detectors across all energies. Taken from [10].

10.1 Application: Surface oxidation and thin coating thickness on substrates

We proved this method on a series of samples with different composition (Cr, Mo, Au) and thicknesses. In case of Cr and Mo the range was from 1 up to 25 nm and from 1 up to 13 nm in case of Au. All samples were prepared by calibrated sputtering on a silicon wafer as the substrate. We found a high precision of estimation with an error lower than 10 % in most cases (the results are shown in Fig. 10.3). The error is increasing at low thickness layers up to 70 % in the case of 1 nm Au. We assume that real error is different because of the inaccuracy of thickness determination by measuring the sputtering time. Sputtering speed was estimated by known time of sputtering and thickness measurement of resulting layer by a profilometer. The great advantage of this method is its magnification independence in a wide range from a hundred to several hundred thousand times.¹ The results of coating layer thickness mapping on a sample of 25 nm Mo on Si substrate is shown in Fig. 10.4. Areas of different coating layer thickness were found after appropriate data filtering. The mean value of 25.45 nm corresponds with its nominal thickness of 25 nm. It is evident from these results, that for higher resolution the image magnification has to be increased. The use of individual pixel values or just light filtration brings significant errors.

For more detailed results of the study see the paper R. Skoupy, T. Fort, and V. Krzyzanek. Nanoscale Estimation of Coating Thickness on Substrates via Standardless BSE Detector Calibration. *Nanomaterials*, 10(2):332, 2 2020. doi:10.3390/nano10020332. Full text of the paper can be found in the annexe B.3. The original idea, detector calibration, image acquisition, data processing and visualisation were done by the author of the thesis.

¹Text of this chapter is modified short version of conference abstract published at Microscopy & Microanalysis 2020, Milwaukee [10].

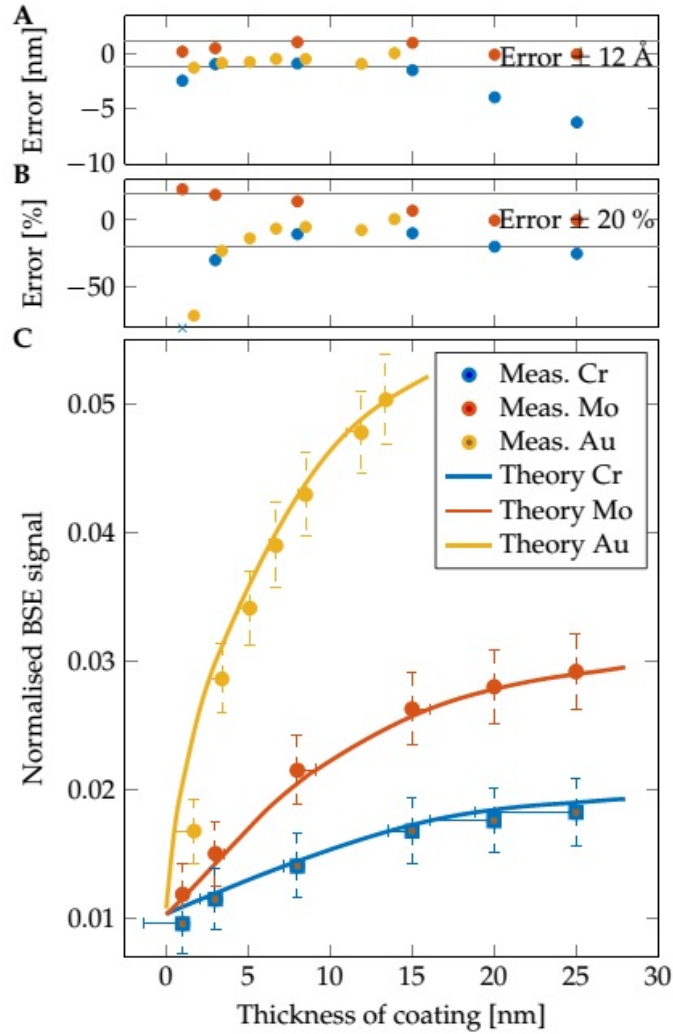


Fig. 10.3: Results of qBSE imaging. (A) Comparison of measured and nominal thicknesses. Most of the measurements show an error lower than 1.2 nm. (B) Comparison of measured and nominal thicknesses. Most of the measurements show an error lower than 20%. The blue \times mark shows a data point out of the used y-axis range. (C) Theoretical BSE signal captured by A segment in working distance of 4 mm for Cr, Mo and Au. The individual points show mean values of measured samples with its standard deviation and horizontal lines indicates the thickness assigned by qBSE imaging. The oxidised layer of Cr is highlighted by square marks. Taken from [11].

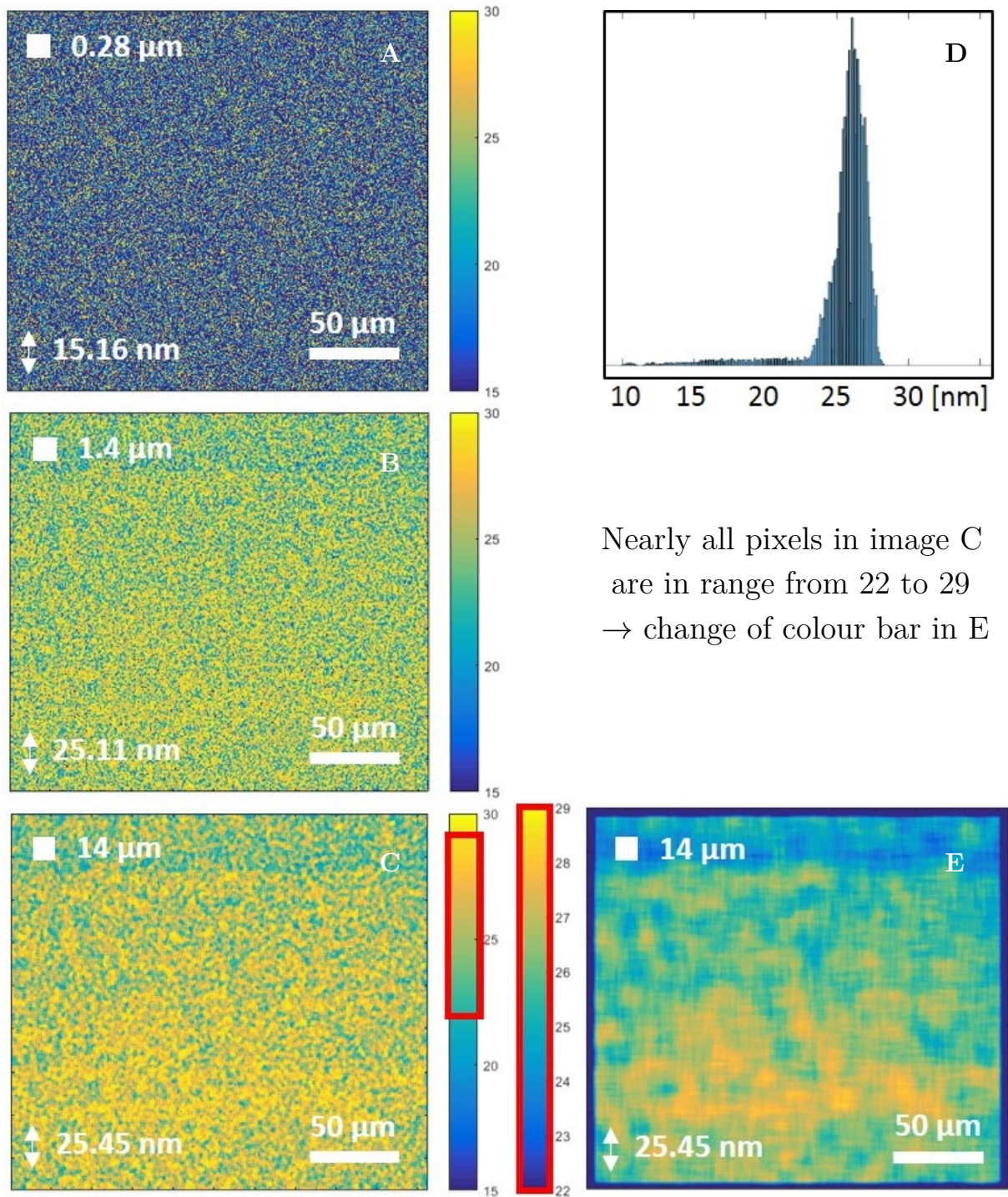


Fig. 10.4: Results of qBSE thickness mapping of the Mo layer with a nominal thickness of 25 nm. (A) Data without filtering – high influence of noise. (B) The same data after 2D median filtration with window 5×5 . (C) The same data after 2D median filtration with window 50×50 . (D) Histogram of values from image part C. (E) Resulting map shows thicker region in the lower part of an investigated area. Each map has information about the size of filter window \square and mean estimated thickness \updownarrow .

11 Correlation of various signals in SEM

When quantitative information comes from a different detector than from the primarily chosen image, the results can be considered as pseudo-quantitative imaging or all-in-one correlative microscopy. There are many combinations in the case of well equipped SEM but unfortunately, no SEM can be equipped with all available techniques. In our lab EDX, CL, SE, BSE, STEM and EBSD detectors are available. Unfortunately, WDS and EELS are missing. Also, the standard sample holders are not suitable for all performed experiments and some new types were developed for special usage.

In the case of EDX analysis on a bulk sample, surface roughness and electric conductivity are very important, because they can influence the resulting accuracy. They can be optimised by polishing and covering the sample with a conductive layer. In the case of a thin sample placed on a TEM grid, there is one more difficulty. The primary electron beam goes through the sample and impacts the stage or bottom part of the vacuum chamber, where additional X-rays are generated. This background limits the quality of acquired spectra. The problem was solved by using a sample holder specially designed to shade the X-ray photons originated under the sample plane.

In the case of CL, placing the sample to the focal point of parabolic collecting mirror of a CL detector plays crucial role. Higher setting accuracy becomes more important in case of weakly emitting samples. Standard TEM grid holder is not applicable because of unsuitable construction, where TEM grids are placed deep under the highest point of the holder. The solution is to develop a new sample holder suitable for CL and STEM. For generation of a sufficient amount of signal higher probe currents may be needed and so lowering sample temperature will be useful.

The developed sample holder assemblies are described in the following documentations (construction part, documentation drawing and some of the main ideas were made by the author of the thesis):

- Cryo-EDX-CL-STEM sample holder is described in functional specimen *Cryo-SEM holder for imaging of thin samples in the transmission mode with elemental and cathodoluminescence analysis*, full text in the annexe C.1.
- Cryo-CL-SEM is described in functional specimen *Cryo-SEM holder and anticontaminator system for cathodoluminescence analysis in SEM at very low temperatures*, full text in the annexe C.2.

11.1 EDX-SEM: Analysis of ancient dental calculus

Author contribution: In the presented papers D. Fialova, R. Skoupy, E. Drozdova, A. Patak, J. Pinos, L. Sin, R. Benus, and B. Klima. The Application of Scanning Electron Microscopy with Energy-Dispersive X-Ray Spectroscopy (SEM-EDX) in Ancient Dental Calculus for the Reconstruction of Human Habits. *Microscopy and Microanalysis*, 23(6):1207–1213, 2017. doi: 10.1017/s1431927617012661 (full text of paper in the annex B.4) nearly all SEM investigation was done by the author of the thesis. It includes sample preparation and mounting, SE and EDX imaging and analysis.

The great potential of EDX-SEM is in the detection of unusual chemical elements included in ancient human dental calculus to verify the hypotheses about life and burial habits of ancient populations and individuals. Elemental spectral analyses were performed on archaeological samples of three chosen individuals from different time periods. The unusual presence of Mg, Al, and Si in the first sample could confirm the hypothesis of high degree of dental abrasion caused by particles from grinding stones in flour. In the second sample, the presence of Cu could confirm that bronze jewelry could lie near the buried body. The elemental composition of the third sample with the presence of Pb and Cu confirms the origin of individual to Napoleonic Wars because the damage to his teeth could be explained by the systematic utilization of the teeth for the opening of paper cartridges (a charge with a dose of gunpowder and a bullet), which were used during the 18th and the 19th century AD. All these results contribute to the reconstruction of life (first and third individual) and burial (second individual) habits of ancient populations and individuals [12]. The main findings are summarised in Fig. 11.1.

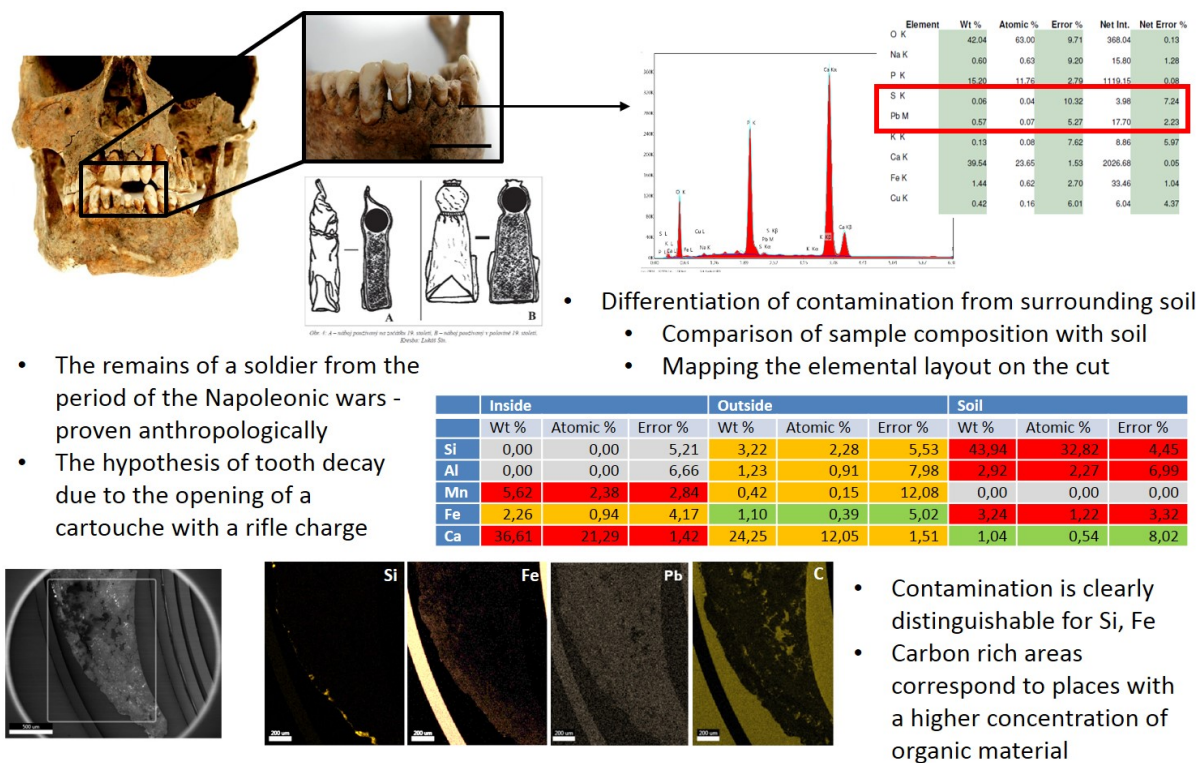


Fig. 11.1: Analysis of human ancient tartar. Confirmation of the hypothesis of tooth damage caused by repeated opening of cartridges with bullet and gunpowder. Based on [12].

11.2 EDX-STEM: Characterisation of urban aerosol pollution

Author contribution: In the presented paper S. Marvanova, P. Kulich, R. Skoupy, F. Hubatka, M. Ciganek, J. Bendl, J. Hovorka, and M. Machala. Size-segregated urban aerosol characterization by electron microscopy and dynamic light scattering and influence of sample preparation. *Atmospheric Environment*, 178:181–190, 2018. doi:10.1016/j.atmosenv.2018.02.004 (full text of paper in the annexe B.5) the SE, STEM and EDX analysis of particles mounted on TEM grids was done by the author of this thesis.

Size-segregated particulate matter (PM) is frequently used in chemical and toxicological studies. Nevertheless, toxicological *in vitro* studies working with the whole particles often lack a proper evaluation of PM real size distribution and characterization of agglomeration under the experimental conditions. In this study, changes in particle size distributions during the PM sample manipulation and also semiquantitative elemental composition of single particles were evaluated. Coarse (1–10 μm), upper accumulation (0.5–1 μm), lower accumulation (0.17–0.5 μm), and ultrafine (<0.17 μm) PM fractions were collected by high volume cascade impactor in Prague city center. Particles were examined using electron microscopy and their elemental composition was determined by EDX. Larger or smaller particles, not corresponding to the impaction cut points, were found in all fractions, as they occur in agglomerates and are impacted according to their aerodynamic diameter. Elemental composition of particles in size-segregated fractions varied significantly. Ns-soot occurred in all size fractions. Metallic nanospheres were found in accumulation fractions, but not in ultrafine fraction where ns-soot, carbonaceous particles, and inorganic salts were identified. Dynamic light scattering was used to measure particle size distribution in water and in cell culture media. PM suspension of lower accumulation fraction in water agglomerated after freezing/thawing the sample, and the agglomerates were disrupted by subsequent sonication. Ultrafine fraction did not agglomerate after freezing/thawing the sample. Both lower accumulation and ultrafine fractions were stable in cell culture media with fetal bovine serum, while high agglomeration occurred in media without fetal bovine serum as measured during 24 h [13]. The examples of investigated samples are shown in Fig. 11.2.

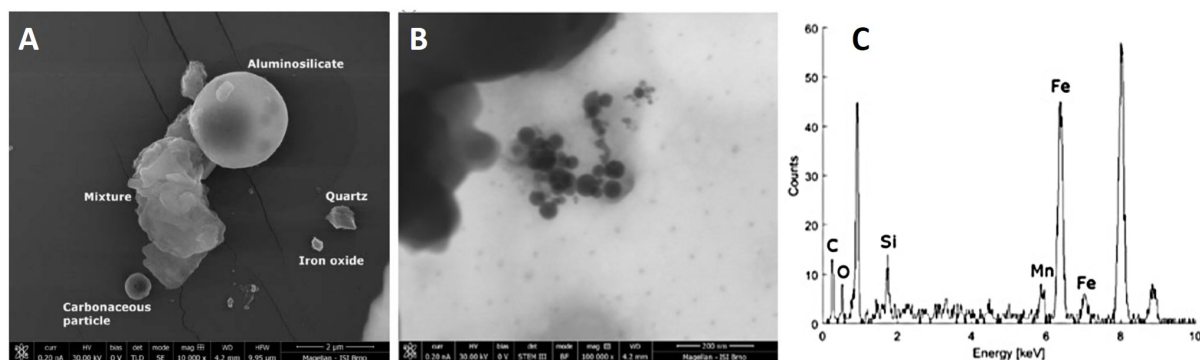


Fig. 11.2: Analysis of urban aerosol nanoparticles by EDX-S(T)EM. (A) SEM micrograph of various particles with their identification. (B) Agglomerate of iron nanoparticles with diameters ranging from 5 to 55 nm. (C) EDX spectrum of previous agglomerate. Adapted from [13].

11.3 EDX-STEM: Selenium nanonutrients for fish

Author contribution: In the presented paper F. Abdolapur Monikh, L. Chupani, K. Smerkova, T. Bosker, P. Cizar, V. Krzyzanek, L. Richtera, R. Franek, E. Zuskova, R. Skoupy, G. K. Darbha, M. Vijver, E. Valsami-Jones, and W. Peijnenburg. Engineered nanoselenium supplemented fish diet: toxicity comparison with ionic selenium and stability against particle dissolution, aggregation and release. *Environmental Science: Nano*, 2020. doi:10.1039/D0EN00240B the STEM and EDX analysis of particles mounted on TEM grids was done by the author of this thesis.

Transformation of nutrients to their nano-form, such as Se engineered nanonutrients (Se-ENNs), is expected to enhance the absorption of the nutrients into fish and increase the efficiency of the feed. However, dissolution, aggregation, and release of ENNs from the feed matrix may decrease the efficiency of the Se-ENNs. In this study, we provided fish feed supplemented with Se-ENNs which do not aggregate or dissolve and the particles are also not released from the feed matrix. As a proof of principle, we compared the toxicity of a diet containing Se-ENNs of two different sizes (60 and 120 nm) with diets containing ionic Se. The adverse effects were measured by monitoring the survival rate, acetylcholinesterase (AChE) levels and swimming behavior of zebrafish over 21 days of feeding with either the Se-ENNs or ionic Se supplemented fish diets. The number size distribution of the 60 nm Se-ENNs in the diet was similar to that in MilliQ water, while the size distribution of the 120 nm Se-ENNs in the diet was slightly wider. Ion and particle release from Se-ENNs containing diets in the exposure media was not observed, indicating the stability of the particles in the feed matrices. To determine toxicity, zebrafish (*Danio rerio*) were nourished using a control diet (without Se and Se-ENNs), Se (sodium selenite) containing diets (with 2.4 or 240 mg Se per kg feed) and Se-ENNs containing diets (with 2.4 or 240 mg Se-ENNs of 60 or 120 nm per kg feed) for 21 days. Both sizes of Se-ENNs were taken up in the fish, however only the 120 nm Se-ENNs were detected in the brains of fish. Zebrafish fed with Se-ENNs supplemented diets (60 and 120 nm) showed normal swimming behavior compared to the control. No significant alteration was determined in the AChE activity of the fish fed with the Se-ENNs supplemented diet. In contrast, feeding the zebrafish with a diet containing 240 mg/kg Se led to lethal effects. These observations clearly depict the potential benefits of using Se-ENNs as nutrients in fish feed [14]. Results of nanoparticle characterisation are shown in Fig. 11.3.

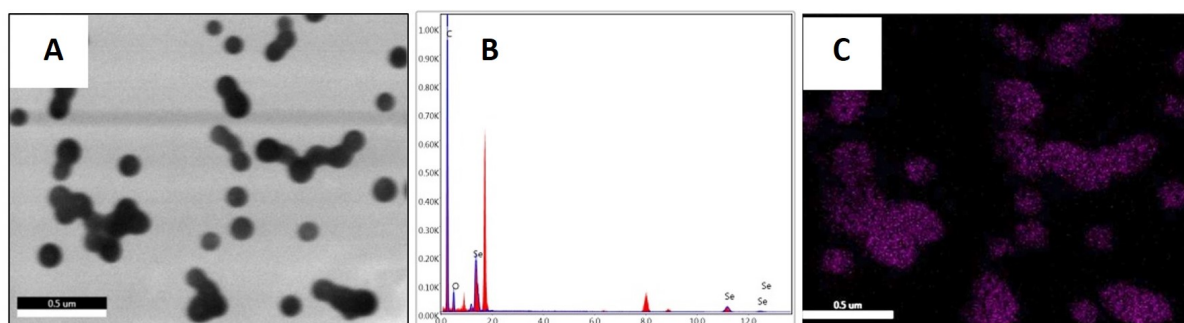


Fig. 11.3: The bright-field STEM image of selenium particles with nominal size of 120 nm (A), its EDX spectrum (B) and EDX map for selenium (C). Adapted from [14].

11.4 CL-STEM: Carboxylated nanodiamonds in THP-1 cells

Author contribution: In the presented paper P. T. Knotigova, J. Masek, F. Hubatka, J. Koutoucek, P. Kulich, P. Simeckova, E. Bartheldyova, M. Machala, T. Svadlakova, J. Krejsek, N. Vaskovicova, R. Skoupy, V. Krzyzanek, et al. Application of Advanced Microscopic Methods to Study the Interaction of Carboxylated Fluorescent Nanodiamonds with Membrane Structures in THP-1 Cells: Activation of Inflammasome NLRP3 as the Result of Lysosome Destabilization. *Molecular Pharmaceutics*, 16(8):3441–3451, 8 2019. doi:10.1021/acs.molpharmaceut.9b00225 (full text of paper in the annexe B.6) the CL imaging was partially done by the author of this thesis.

Nanodiamonds (ND), especially fluorescent nanodiamonds, represent potentially applicable drugs and probes carriers for *in vitro/in vivo* applications. The main purpose of this study was to relate physical-chemical properties of carboxylated ND to their intracellular distribution, impact on membranes and cell immunity – activation of inflammasome in *in vitro* THP-1 cell line model. Dynamic light scattering, nanoparticle tracking analysis and microscopic methods were used to characterize nanodiamond particles and their intracellular distribution. Fluorescent NDs penetrated cell membranes by both macropinocytosis and mechanical cutting through cell membranes. We proved accumulation of fluorescent NDs in lysosomes. In this case, lysosomes were destabilised and Cathepsin B was released into cytoplasm and triggered pathways leading to activation of inflammasome NLRP3 as detected in THP-1 cells. Activation of inflammasome by ND represents an important event that could underlie the described toxicological effects *in vivo* induced by NDs. According to our knowledge, this is the first *in vitro* study demonstrating direct activation of inflammasome by ND. These findings are important for understanding the mechanism(s) of action of ND complexes and explain the ambiguity of the existing toxicological data [15]. An example of investigated nanodiamond cluster is shown in Fig. 11.4.

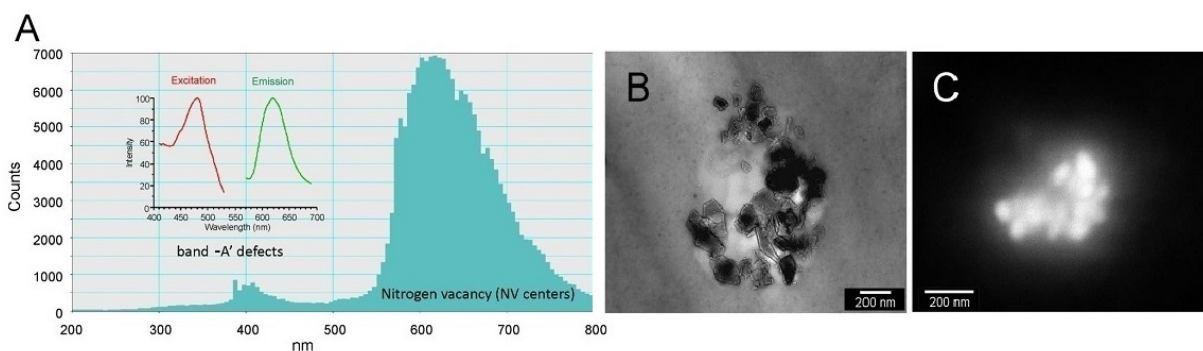


Fig. 11.4: (A) CL spectrum of fluorescent nanodiamond measured in SEM and fluorescence spectrum (insert) of the same sample. (B) Detail of intracellular vesicle coated by fluorescent nanodiamonds visualized by TEM. (C) CL detail of fluorescent nanodiamond cluster associated with intracellular vesicle in THP-1 cell. Adapted from [15].

11.5 EDX-CL-STEM: TiO₂ nanoparticles distribution in mice organs

Author contribution: In the presented conference proceedings paper M. Machala, P. Kulich, O. Sery, S. Marvanova, R. Skoupy, A. Rusnak, P. Mikuska, and Z. Vecera. The deposition of inhaled titanium nanoparticles in mice organs. In *Toxicology Letters: Abstracts of the 52nd Congress of the European Societies of Toxicology (EUROTOX) Fibes Congress Center Seville*, volume 258, page S277, 2016. doi:10.1016/j.toxlet.2016.06.1969 and corresponding study where the paper is in preparation, the CL-EDX-STEM imaging was done by the author of this thesis.

In the presented study, biokinetics and deposition of titanium dioxide nanoparticles were studied in female ICR mice, after continuous 12-week exposure in inhalation chamber. Uniformity, shape and size of NPs were characterized by TEM and SEM. The study particularly focused on the distribution of Ti NPs in selected tissues. The samples of lung, liver, kidney, spleen and brain were sectioned, fixed and then embedded in Epon-Durcupan mixture. TEM and/or SEM were used for sample observation. Finally, EDX was used in order to evaluate Ti presence in secondary lysosomes of target organ cells. The results indicate that Ti NPs may pass into alveoli and then passively transfer through their membrane, as no signs of phagocytosis or endocytosis were observed. The exposure to Ti NPs gradually induced a loss of type I pneumocytes and alveoli thickening. Within the type II pneumocytes, Ti NPs were found to be deposited within secondary lysosomes, as confirmed by two types of independent EDX analyses. In general, our findings seem to support the hypothesis that the inhaled Ti NPs are translocated via lung-red blood cells-target organ axis and that erythrocytes may serve as principle carriers of Ti NPs [186]. The main findings are summarised in Fig. 11.5 and 11.6.

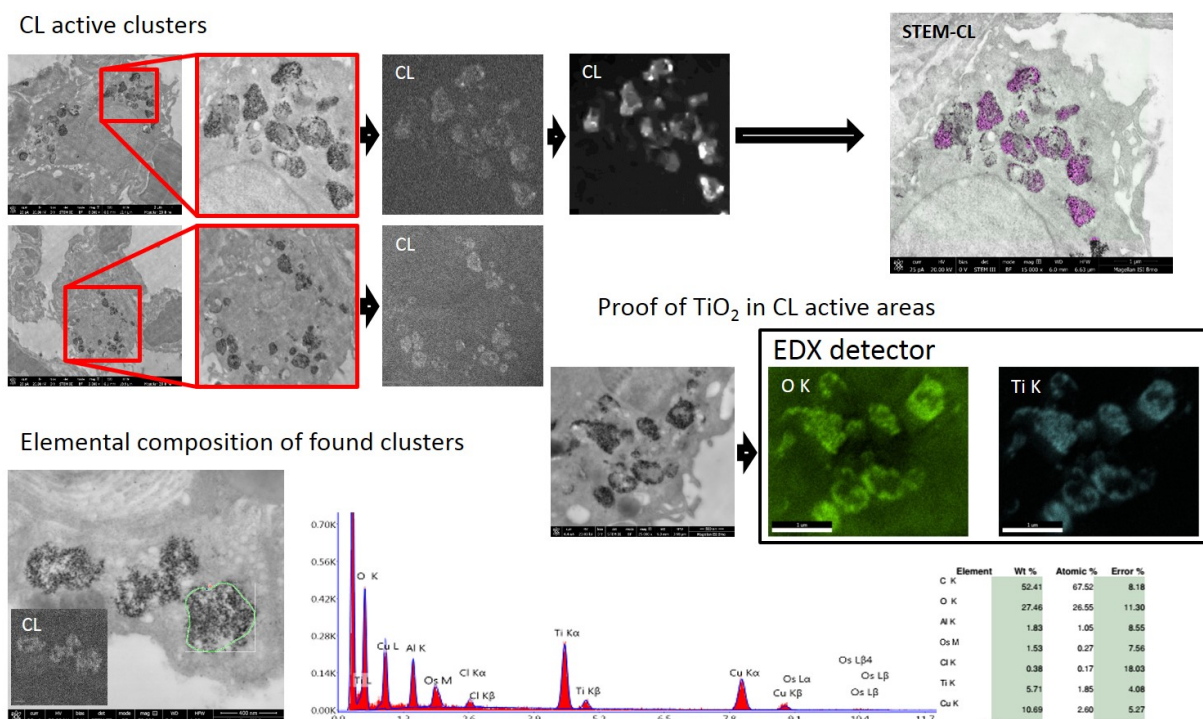


Fig. 11.5: Correlative imaging of TiO₂ nanoparticles inside lung mouse tissue. High-resolution BF-STEM images are supplemented with CL, EDX mapping and EDX spectral analysis of chosen clusters.

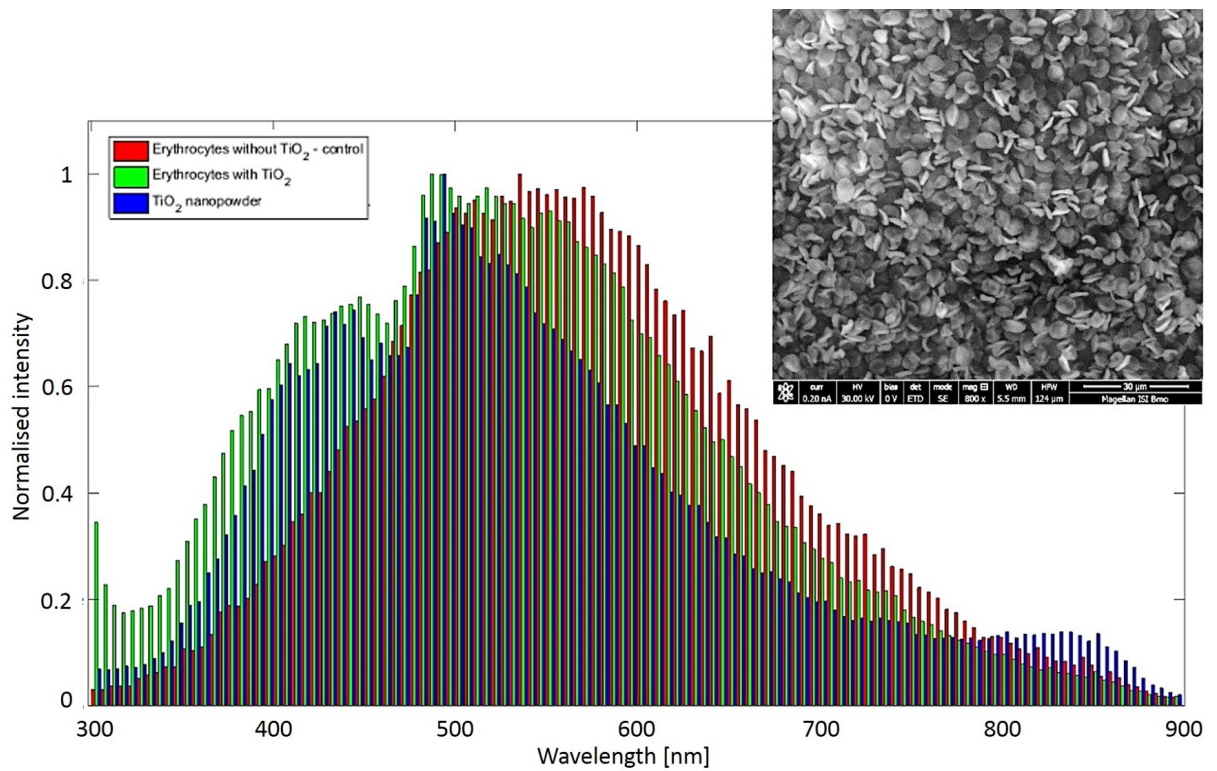


Fig. 11.6: Proof of evidence of TiO₂ inside mouse erythrocytes. CL spectrum of erythrocytes with TiO₂ is a combination of TiO₂ free erythrocytes and pure TiO₂ powder. This is visible at peak at 430 nm and extension of the main peak to the lower wavelengths.

Part IV

Conclusion

The presented thesis describes the possibilities of quantitative imaging in a scanning electron microscope. The thesis includes necessary theory description in the *Part I: State of the art*. The main focus is placed on types of signals generated in SEM after impact of primary electron beam and their using in various imaging and analytical techniques. It also gives overview of electron beam/matter simulation principles and software, which are available and widely used in the field of electron microscopy. The theoretical part consists of basic description of fundamental processes, physics and techniques with links to closely focused literature dealing with individual areas, where very detailed descriptions can be found. This part is composed of information from literature review or web pages dealing with Monte Carlo software and summarises available knowledge.

Previous purely theoretical part is followed by the *Part II: Quantitative imaging* which is based on recently published literature review together with author's findings, simulations and experience added with the aim to ensure easier understanding and clarity. The methods of quantitative STEM and BSE imaging are introduced and described in detail. It includes principles, application areas, specifics of different detector types (scintillator based vs. semiconductor, annular vs. pixelated), detector calibration methods and their influence on the results or signal transformation from qualitative to quantitative. Moreover two quantitative imaging modes: *thickness measurement assuming a constant density* and *density measurement assuming a constant thickness* are introduced and discussed for further use in the application part.

The most comprehensive *Part III: Results* shows achieved results, which were accomplished during work on the thesis. The description is in very detailed form in case of results, which were not published in reviewed journals yet. On the other hand, the results that have been so far published are mentioned only in the form of an overview with highlighting of the main ideas together with links to the full texts placed in the annexes. This part is divided into several chapters which differ in their focus.

The first one, *Chapter 7: Quantitative imaging using scintillator based STEM detector* represents fully calibrated detection system for qSTEM. The system has its main advantage in simultaneous beam current fluctuation correction during the data acquisition. The system was mounted, tested and prepared for its use in applications when a previously unexpected problem has occurred. The system is working in low-magnification mode where no magnetic field is on a sample, but for practical use the maximum magnification of low-mag mode is not satisfactory. Unfortunately, the magnetic field closure is not provided for this type of microscope and the effort to bypass the limitation by refining the scan step with external scanning unit brought interference to the captured image. The experiences gained during the system development were used during design of second generation of fast scintillator based STEM detector, which is adapted for its mounting on more suitable microscopes.

The next *Chapter 8: Quantitative imaging using semiconductor annular STEM detector* deals with in-depth analysis of the accuracy of the method and influence of imperfect STEM detector adjustment on the optical axis of the electron column. It was found out, that usual misalignment does not bring any significant errors and no special care is needed. The accuracy was estimated on sample of latex nanosphere where true local thickness can be computed from its geometry. The error was estimated in percent units for individual STEM detector segments with possible accuracy enhancing, by simultaneous imaging in two different segments (BF and HAADF). The method of qSTEM was applied for the study of electron beam induced mass-loss of epoxy resin sections at various conditions. The aim was to find out recommendations which

would reduce the induced mass-loss. The samples of EMbed 812 resin were studied in slices with thicknesses of 30, 60, 100 and 150 nm and beam energy of 30 keV. The variable conditions were age, staining, beam current, plasma cleaning, covering by thin carbon layer and temperature. The general recommendation coming from our study is imaging around the day 10 after slicing, cover slices by a thin carbon layer, work without staining and plasma cleaning and at low temperatures. Beam current dependency is weak and do not play significant role.

The main disadvantage of annular STEM detector based qSTEM is its need for a precise detector calibration and contrast and brightness settings before each imaging session. This limitation may be overcome by using different signal property than the signal intensity. The *Chapter 9: Quantitative imaging using pixelated STEM detector* presents a new methodology of calibration-less quantitative STEM imaging. In this case, the angle of the most probable scattering is used instead of image intensity and so contrast drift does not play any role. This approach has limitation in finite range of thicknesses which can be measured. It is given by a creation of detectable peak in amount of captured electrons to angle dependency and maximum cover angle of the detector. Another advantage of the method is the possibility to apply it on previously captured data because no special steps are needed before imaging.

The principle of quantitative imaging is not limited to STEM detector and it is applicable for BSE detector as well. Many papers dealing with quantitative BSE imaging can be found, but all of them use some type of standard based calibration for linking captured data and simulation or standard series. The *Chapter 10: Quantitative imaging using BSE detector* introduces new BSE detector calibration technique, which enables absolute and standard-less calibration of the detector in its working (inserted) position. The primary electron beam is reflected on biased electron mirror, made of thin gold coating on a glass substrate, and impacts the detector on its sensitive side. The developed calibration method was proved by measurement of thin metal coatings on silicon substrates with high accuracy better than 1 nm in most cases. The qBSE technique is magnification independent in wide range of magnifications (tested from 50 up to 500,000 \times) and the information about local covering layer thickness is in each pixel of the captured image and thus the method is applicable for 2D mapping at various fields of view.

Last but not least, the thesis includes multiple applications of widespread quantitative techniques of cathodoluminescence and energy dispersive X-ray spectroscopy in combination with high resolution imaging in transmitted or secondary electrons. The *Chapter 11: Correlation of various signals in SEM* consists of five different applications dealing with different types of samples. To perform those measurements several types of sample holders enabling correlative CL, EDX and STEM/SE were designed, made and applied.

In general, the thesis presents the possibilities of quantitative imaging in scanning electron microscope together with instrumental and methodological development of 2D-STEM and BSE detector based techniques, where significant results and improvements were achieved.

Bibliography

- [1] A. Ul-Hamid. *A Beginners' Guide to Scanning Electron Microscopy*. Springer International Publishing, Cham, 2018. doi:10.1007/978-3-319-98482-7.
- [2] D. B. Williams and C. B. Carter. *Transmission Electron Microscopy*. Springer US, Boston, MA, 2009. doi:10.1007/978-0-387-76501-3.
- [3] D. Drouin, A. R. Couture, D. Joly, X. Tastet, V. Aimez, and R. Gauvin. CASINO V2.42—A Fast and Easy-to-use Modeling Tool for Scanning Electron Microscopy and Microanalysis Users. *Scanning*, 29(3):92–101, 5 2007. doi:10.1002/sca.20000.
- [4] L. Reimer. *Scanning Electron Microscopy: Physics of Image Formation and Microanalysis*. Springer Berlin Heidelberg, New York, second edition, 1998.
- [5] R. F. Egerton. *Physical Principles of Electron Microscopy*. Springer US, Boston, MA, 1 edition edition, 2005. doi:10.1007/b136495.
- [6] L. Reimer and C. Tollkamp. Measuring the backscattering coefficient and secondary electron yield inside a scanning electron microscope. *Scanning*, 3(1):35–39, 1980. doi:10.1002/sca.4950030105.
- [7] R. Skoupy, J. Nebesarova, and V. Krzyzanek. Electron Beam Induced Mass Loss Dependence on Stained Thin Epon Resin Sections. *Microscopy and Microanalysis*, 22(S3):926–927, 7 2016. doi:10.1017/S143192761600547X.
- [8] R. Skoupy, V. Krzyzanek, and J. Nebesarova. Plasma cleaning effect on the stability of the Epon resin sections. In *European Microscopy Congress 2016: Proceedings*, pages 597–598, Weinheim, Germany, 12 2016. Wiley-VCH Verlag GmbH & Co. KGaA. doi:10.1002/9783527808465.EMC2016.5995.
- [9] R. Skoupy, J. Nebesářová, and V. Krzyžánek. Temperature dependent mass loss of Epon resin sections. In *Mikroskopie 2016: Proceedings*, page 56. Czechoslovak microscopy society, Praha, 2016.
- [10] R. Skoupy and V. Krzyzanek. Beam energy dependent calibration of STEM and BSE detectors for thin film thickness estimation. In *Microscopy and Microanalysis, Milwaukee*, Milwaukee, 2020.
- [11] R. Skoupy, T. Fort, and V. Krzyzanek. Nanoscale Estimation of Coating Thickness on Substrates via Standardless BSE Detector Calibration. *Nanomaterials*, 10(2):332, 2 2020. doi:10.3390/nano10020332.
- [12] D. Fialova, R. Skoupy, E. Drozdova, A. Patak, J. Pinos, L. Sin, R. Benus, and B. Klima. The Application of Scanning Electron Microscopy with Energy-Dispersive X-Ray Spectroscopy (SEM-EDX) in Ancient Dental Calculus for the Reconstruction of Human Habits. *Microscopy and Microanalysis*, 23(6):1207–1213, 2017. doi:10.1017/s1431927617012661.
- [13] S. Marvanova, P. Kulich, R. Skoupy, F. Hubatka, M. Ciganek, J. Bendl, J. Hovorka, and M. Machala. Size-segregated urban aerosol characterization by electron microscopy and

- dynamic light scattering and influence of sample preparation. *Atmospheric Environment*, 178:181–190, 2018. doi:10.1016/j.atmosenv.2018.02.004.
- [14] F. Abdollahpur Monikh, L. Chupani, K. Smerkova, T. Bosker, P. Cizar, V. Krzyzanek, L. Richtera, R. Franek, E. Zuskova, R. Skoupy, G. K. Darbha, M. Vijver, E. Valsami-Jones, and W. Peijnenburg. Engineered nanoselenium supplemented fish diet: toxicity comparison with ionic selenium and stability against particle dissolution, aggregation and release. *Environmental Science: Nano*, 2020. doi:10.1039/DOEN00240B.
- [15] P. T. Knotigova, J. Masek, F. Hubatka, J. Kotoucek, P. Kulich, P. Simeckova, E. Bartheldyova, M. Machala, T. Svadlakova, J. Krejsek, N. Vaskovicova, R. Skoupy, V. Krzyzanek, et al. Application of Advanced Microscopic Methods to Study the Interaction of Carboxylated Fluorescent Nanodiamonds with Membrane Structures in THP-1 Cells: Activation of Inflammasome NLRP3 as the Result of Lysosome Destabilization. *Molecular Pharmaceutics*, 16(8):3441–3451, 8 2019. doi:10.1021/acs.molpharmaceut.9b00225.
- [16] V. Krzyzanek and R. Reichelt. MONCA: A New MATLAB Package for Monte Carlo Simulation of Electron Scattering in Thin Specimens in the Energy Range 10 – 200 keV. *Microscopy and Microanalysis*, 9(S03):110–111, 9 2003. doi:10.1017/S1431927603014065.
- [17] Michael Stöger-Pollach. EELS and CL for chemical and optical quantification in (scanning) transmission electron microscopy, 2019.
- [18] NISTMonte: A Monte Carlo simulation of electron and x-ray transport for complex sample geometries. URL: <https://cst1.nist.gov/div837/837.02/epq/index.html>.
- [19] ELECTRON MICROSCOPY SCIENCES: Technical data sheets: EMbed 812 Kit, 2019. URL: <https://www.emsdiasum.com/microscopy/technical/datasheet/14120.aspx>.
- [20] 3D SEM | SEM | Volumescope 2 | Thermo Fisher Scientific - CZ. URL: <https://www.thermofisher.com/cz/en/home/electron-microscopy/products/scanning-electron-microscopes/volumescope-2-sem.html>.
- [21] R. F. Egerton. *Physical Principles of Electron Microscopy*. Springer International Publishing, Cham, 2016. doi:10.1007/978-3-319-39877-8.
- [22] J. I. Goldstein, D. E. Newbury, P. Echlin, D. C. Joy, C. E. Lyman, E. Lifshin, L. Sawyer, and J. R. Michael. *Scanning Electron Microscopy and X-ray Microanalysis*. Springer US, Boston, MA, 2003. doi:10.1007/978-1-4615-0215-9.
- [23] J. I. Goldstein, D. E. Newbury, J. R. Michael, N. W. Ritchie, J. H. J. Scott, and D. C. Joy. *Scanning Electron Microscopy and X-Ray Microanalysis*. Springer New York, New York, NY, 2018. doi:10.1007/978-1-4939-6676-9.
- [24] G. Salviati, F. Fabbri, F. Detto, F. Rossi, L. Lazzarini, and T. Sekiguchi. Cathodoluminescence of Self-assembled Nanosystems: The Cases of Tetrapods, Nanowires, and Nanocrystals. In *Characterization of Semiconductor Heterostructures and Nanostructures: Second Edition*. 2013. doi:10.1016/B978-0-444-59551-5.00013-3.

- [25] B. G. Yacobi and D. B. Holt. *Cathodoluminescence Microscopy of Inorganic Solids*. Springer US, Boston, MA, 1990. doi:10.1007/978-1-4757-9595-0.
- [26] J. Wolstenholme. *Auger Electron Spectroscopy: Practical Application to Materials Analysis and Characterization of Surfaces, Interfaces, and Thin Films*. Momentum Press, New York, 2015.
- [27] S. J. Pennycook and P. D. Nellist, editors. *Scanning Transmission Electron Microscopy*. Springer New York, New York, NY, 2011. URL: <http://link.springer.com/10.1007/978-1-4419-7200-2>, doi:10.1007/978-1-4419-7200-2.
- [28] A. J. Schwartz, M. Kumar, B. L. Adams, and D. P. Field, editors. *Electron Backscatter Diffraction in Materials Science*. Springer US, Boston, MA, 2009. doi:10.1007/978-0-387-88136-2.
- [29] A. Khursheed. Energy Analyzer Attachments for the Scanning Electron Microscope. *Microscopy and Microanalysis*, 21(S4):130–135, 6 2015. doi:10.1017/S1431927615013264.
- [30] D. Gall. Electron mean free path in elemental metals. *Journal of Applied Physics*, 119(8):085101, 2 2016. URL: <http://aip.scitation.org/doi/10.1063/1.4942216>, doi:10.1063/1.4942216.
- [31] L. Reimer. Quantitative scanning electron microscopy of surfaces. *Le Journal de Physique Colloques*, 45(C2):2–291, 2 1984. doi:10.1051/jphyscol:1984265.
- [32] B. J. Inkson. Scanning electron microscopy (SEM) and transmission electron microscopy (TEM) for materials characterization. In *Materials Characterization Using Nondestructive Evaluation (NDE) Methods*, pages 17–43. Elsevier, 2016. doi:10.1016/B978-0-08-100040-3.00002-X.
- [33] J. C. Rivière. Auger electron spectroscopy. *Contemporary Physics*, 14(6):513–539, 1973. doi:10.1080/00107517308210772.
- [34] D. M. Mattox. *Substrate (“Real”) Surfaces and Surface Modification*. 1998. doi:10.1016/b978-081551422-0.50003-6.
- [35] Electron Microscopy: Phase Focus. URL: <https://www.phasefocus.com/other-products/pi-box>.
- [36] T. Luo and A. Khursheed. Transmission EELS attachment for SEM. *IEEE Transactions on Device and Materials Reliability*, 6(2):182–185, 2006. doi:10.1109/TDMR.2006.876582.
- [37] Ultra-high Resolution Scanning Electron Microscope SU9000 : Hitachi High-Tech in Europe. URL: https://www.hitachi-hightech.com/eu/product_detail/?pn=em-su9000&version=.
- [38] T. Sunaoshi, K. Kaji, Y. Orai, C. Schamp, and E. Voelkl. STEM/SEM, Chemical Analysis, Atomic Resolution and Surface Imaging At less than 30 kV with No Aberration Correction for Nanomaterials on Graphene Support. *Microscopy and Microanalysis*, 22(S3):604–605, 2016. doi:10.1017/s1431927616003871.

- [39] G. Salviati, F. Rossi, N. Armani, V. Grillo, and L. Lazzarini. Power-dependent cathodoluminescence in III-nitrides heterostructures: From internal field screening to controlled band-gap modulation. In C. Lamberti, editor, *Characterization of Semiconductor Heterostructures and Nanostructures*, pages 209–248. Elsevier B.V., 2008. doi:10.1016/B978-0-444-53099-8.00007-5.
- [40] N. Brodusch, K. Zaghbi, and R. Gauvin. Improvement of the energy resolution of energy dispersive spectrometers (EDS) using Richardson–Lucy deconvolution. *Ultramicroscopy*, 209:112886, 2 2020. doi:10.1016/j.ultramicro.2019.112886.
- [41] MagnaRay WD Spectrometer, 2008. URL: www.thermo.com.
- [42] O. L. Krivanek, T. C. Lovejoy, M. F. Murfitt, G. Skone, P. E. Batson, and N. Dellby. Towards sub-10 meV energy resolution STEM-EELS. *Journal of Physics: Conference Series*, 522(1), 2014. doi:10.1088/1742-6596/522/1/012023.
- [43] Nion Co. - Results. URL: <http://www.nion.com/results.html>.
- [44] N. Silvis-Cividjian and C. W. Hagen. Electron-Beam-Induced Nanometer-Scale Deposition. pages 1–235. Elsevier Science Publishing Co Inc., San Diego, 2006. doi:10.1016/S1076-5670(06)43001-9.
- [45] R. Shimizu and D. Ze-Jun. Monte Carlo modelling of electron-solid interactions. *Reports on Progress in Physics*, 55(4):487–531, 1992. doi:10.1088/0034-4885/55/4/002.
- [46] T. Klein, E. Buhr, and C. Georg Frase. *TSEM: A review of scanning electron microscopy in transmission mode and its applications*, volume 171. Elsevier Inc., 2012. doi:10.1016/B978-0-12-394297-5.00006-4.
- [47] H. Bethe. Theory of passage of swift corpuscular rays through matter. *Annalen der Physik*, 5(3):325–400, 1930.
- [48] D. C. Joy and S. Luo. An empirical stopping power relationship for low-energy electrons. *Scanning*, 11(4):176–180, 1989. doi:10.1002/sca.4950110404.
- [49] E. Rutherford. Elastic cross section. *Philosophical Magazine*, 21:669–680, 1911.
- [50] D. C. Joy. *Monte Carlo Modeling for Electron Microscopy and Microanalysis*. Oxford University Press, New York, 1995.
- [51] D. E. Newbury. Electron beam specimen interactions in the analytical electron microscope. In D. C. Joy, A. D. J. Romig, and J. I. Goldstein, editors, *Principles of Analytical Electron Microscopy*. Plenum Press, New York.
- [52] J. Henoc and F. Maurice. A flexible and complete Monte Carlo procedure for the study of the choice of parameters. In *In Electron Probe Quantitation*, pages 105–143. Plenum Press, New York, 1991.
- [53] N. F. Mott. The scattering of fast electrons by atomic nuclei. *Proceedings of the Royal Society of London. Series A, Containing Papers of a Mathematical and Physical Character*, 124(794):425–442, 6 1929. doi:10.1098/rspa.1929.0127.

- [54] N. F. Mott. The polarisation of electrons by double scattering. *Proceedings of the Royal Society of London. Series A, Containing Papers of a Mathematical and Physical Character*, 135(827):429–458, 3 1932. doi:10.1098/rspa.1932.0044.
- [55] M. J. Boschini, C. Consolandi, M. Gervasi, S. Giani, D. Grandi, V. Ivanchenko, P. Nieminen, S. Pensotti, P. G. Rancoita, and M. Tacconi. An expression for the Mott cross section of electrons and positrons on nuclei with Z up to 118. *Radiation Physics and Chemistry*, 90:39–66, 2013. doi:10.1016/j.radphyschem.2013.04.020.
- [56] R. Gauvin and D. Drouin. A formula to compute total elastic mott cross-sections. *Scanning*, 15(3):140–150, 1993. doi:10.1002/sca.4950150306.
- [57] R. Browning, T. Z. Li, B. Chui, J. Ye, R. F. W. Pease, Z. Czyzewski, and D. C. Joy. Empirical forms for the electron/atom elastic scattering cross sections from 0.1 to 30 keV. *Journal of Applied Physics*, 76(4):2016–2022, 8 1994. doi:10.1063/1.357669.
- [58] F. Salvat, A. Jablonski, and C. J. Powell. Elsepa - Dirac partial-wave calculation of elastic scattering of electrons and positrons by atoms, positive ions and molecules. *Computer Physics Communications*, 165(2):157–190, 2005. doi:10.1016/j.cpc.2004.09.006.
- [59] Z. Ruan, R. G. Zeng, Y. Ming, M. Zhang, B. Da, S. F. Mao, and Z. J. Ding. Quantum-trajectory Monte Carlo method for study of electron-crystal interaction in STEM. *Physical Chemistry Chemical Physics*, 17(27):17628–17637, 2015. doi:10.1039/c5cp02300a.
- [60] Small World Electron Flight Simulator Version 3.1 Software for Modelling of Electron Beam and X-ray | 09306-AB | SPI Supplies. URL: <https://www.2spi.com/item/09306-ab/>.
- [61] P. Hovington, D. Drouin, and R. Gauvin. CASINO: A new monte carlo code in C language for electron beam interaction -part I: Description of the program. *Scanning*, 19(1):1–14, 2006. doi:10.1002/sca.4950190101.
- [62] Casino. URL: <https://www.gel.usherbrooke.ca/casino/What.html>.
- [63] P. Pinard, H. Demers, R. Gauvin, and S. Richter. pyMonteCarlo: A Common Programming Interface for Running Identical Simulations using Different Monte Carlo Programs. *Microscopy and Microanalysis*, 19(S2):822–823, 8 2013. doi:10.1017/S1431927613006107.
- [64] pyMonteCarlo — pyMonteCarlo 1.0.0 documentation. URL: <https://pymontecarlo.readthedocs.io/en/latest/index.html>.
- [65] H. Demers, N. Poirier-Demers, A. R. Couture, D. Joly, M. Guilmain, N. de Jonge, and D. Drouin. Three-dimensional electron microscopy simulation with the CASINO Monte Carlo software. *Scanning*, 33(3):135–146, 5 2011. doi:10.1002/sca.20262.
- [66] H. Demers, N. Poirier-Demers, D. Drouin, and N. De Jonge. Simulating STEM imaging of nanoparticles in micrometers-thick substrates. *Microscopy and Microanalysis*, 16(6):795–804, 12 2010. doi:10.1017/S1431927610094080.

- [67] pycasinotools — pycasinotools 0.2.2 documentation. URL: <https://pycasinotools.readthedocs.io/en/latest/readme.html>.
- [68] R. Gauvin, E. Lifshin, H. Demers, P. Horny, and H. Campbell. Win X-ray: A new Monte Carlo program that computes X-ray spectra obtained with a scanning electron microscope. *Microscopy and Microanalysis*, 12(1):49–64, 2006. doi:10.1017/S1431927606060089.
- [69] Our Programs | McGill Electron Microscopy Research Group. URL: <https://www.memrg.com/programs-download>.
- [70] P. Michaud and R. Gauvin. MC X-Ray, The Monte Carlo Program for Quantitative Electron Microscopy of Real Materials. *Microscopy and Microanalysis*, 16(S2):278–279, 7 2010. doi:10.1017/S1431927610054668.
- [71] DTSA-II: Son of DeskTop Spectrum Analyzer. URL: <https://www.cstl.nist.gov/div837/837.02/epq/dtsa2/index.html>.
- [72] N. W. Ritchie. A new Monte Carlo application for complex sample geometries. *Surface and Interface Analysis*, 37(11):1006–1011, 2005. doi:10.1002/sia.2093.
- [73] J. R. Lowney and E. Marx. User’s Manual for the Program MONSEL-1: Monte Carlo Simulation of SEM Signals for Linewidth Metrology. Technical report, National Institute of Standards and Technology, Gaithersburg, 1994.
- [74] J. R. Lowney. MONSEL-II: Monte Carlo simulation of SEM signals for linewidth metrology. *Microbeam Analysis*, 4:131–136, 1995.
- [75] J. R. Lowney. Monte Carlo simulation of scanning electron microscope signals for lithographic metrology. *Scanning*, 18(4):301–306, 12 1996. doi:10.1002/sca.1996.4950180406.
- [76] Welcome — pyPENELOPE. URL: <http://pypenelope.sourceforge.net/>.
- [77] PENELOPE2014, A Code System for Monte-Carlo Simulation of Electron and Photon Transport. URL: <https://www.oecd-nea.org/tools/abstract/detail/nea-1525>.
- [78] F. Salvat, J. M. Fernández, and J. Sempau. PENELOPE -2006 : A Code System for Monte Carlo Simulation of Electron and Photon Transport. In *Workshop Proceedings. NUCLEAR ENERGY AGENCY ORGANISATION FOR ECONOMIC CO-OPERATION AND DEVELOPMENT*, 2006.
- [79] E. Kieft and E. Bosch. Refinement of Monte Carlo simulations of electron-specimen interaction in low-voltage SEM. *Journal of Physics D: Applied Physics*, 41(21), 11 2008. doi:10.1088/0022-3727/41/21/215310.
- [80] S. Agostinelli, J. Allison, K. Amako, J. Apostolakis, H. Araujo, P. Arce, M. Asai, D. Axen, S. Banerjee, G. Barrand, F. Behner, L. Bellagamba, J. Boudreau, et al. Geant4—a simulation toolkit. *Nuclear Instruments and Methods in Physics Research Section A: Accelerators, Spectrometers, Detectors and Associated Equipment*, 506(3):250–303, 7 2003. URL: <https://linkinghub.elsevier.com/retrieve/pii/S0168900203013688>, doi:10.1016/S0168-9002(03)01368-8.

- [81] J. Allison, K. Amako, J. Apostolakis, H. Araujo, P. Arce Dubois, M. Asai, G. Barrand, R. Capra, S. Chauvie, R. Chytracsek, G. Cirrone, G. Cooperman, G. Cosmo, et al. Geant4 developments and applications. *IEEE Transactions on Nuclear Science*, 53(1):270–278, 2 2006. URL: <http://ieeexplore.ieee.org/document/1610988/>, doi:10.1109/TNS.2006.869826.
- [82] J. Allison, K. Amako, J. Apostolakis, P. Arce, M. Asai, T. Aso, E. Bagli, A. Bagulya, S. Banerjee, G. Barrand, B. Beck, A. Bogdanov, D. Brandt, et al. Recent developments in Geant4. *Nuclear Instruments and Methods in Physics Research Section A: Accelerators, Spectrometers, Detectors and Associated Equipment*, 835:186–225, 11 2016. URL: <https://linkinghub.elsevier.com/retrieve/pii/S0168900216306957>, doi:10.1016/j.nima.2016.06.125.
- [83] E. Kieft and E. Bosch. Refinement of Monte Carlo simulations of electron-specimen interaction in low-voltage SEM. *Journal of Physics D: Applied Physics*, 41(21), 2008. doi:10.1088/0022-3727/41/21/215310.
- [84] Overview | geant4.web.cern.ch. URL: <http://geant4.web.cern.ch/>.
- [85] CHARIOT: The World’s Most Advanced Monte Carlo Simulation Software for SEM and EBL Applications. URL: <http://www.abeamtech.com/?dir=products/CHARIOT&pg=index>.
- [86] S. V. Babin, S. Borisov, E. Cheremukhin, E. Grachev, V. Korol, and L. E. Ocola. Software tool for advanced Monte Carlo simulation of electron scattering in EBL and SEM: CHARIOT. *Emerging Lithographic Technologies VII*, 5037(510):583, 2003. doi:10.1117/12.504568.
- [87] S. Babin, S. Borisov, A. Ivanchikov, and I. Ruzavin. CHARIOT: Software tool for modeling SEM signal and e-beam lithography. *Physics Procedia*, 1(1):305–313, 2008. URL: <http://dx.doi.org/10.1016/j.phpro.2008.07.110>, doi:10.1016/j.phpro.2008.07.110.
- [88] Home: MC-SET - Monte Carlo Simulation of Electron Trajectories. URL: <https://www.mc-set.com/>.
- [89] R. L. Myklebust, D. E. Newbury, and H. Yakowitz. NBS Monte Carlo Electron Trajectory Calculation Program. In *Proceeding of a Workshop on a Use of Monte Carlo Calculations in Electron Probe Microanalysis and Scanning Electron Microscopy*, pages 105–128, Gaithersburt, 1977. U.S. Government Printing Office.
- [90] EISS - Electron beam Monte Carlo simulator. URL: http://nanonems.imb-cnm.csic.es/index.php?option=com_content&view=category&layout=blog&id=2&Itemid=9&lang=en.
- [91] Monte Carlo Simulations. URL: <http://web.utk.edu/~srcutk/htm/simulati.htm>.
- [92] D. Gnieser, C. G. Frase, H. Bosse, and R. Tutsch. MCSEM- a modular Monte Carlo simulation program for various applications in SEM metrology and SEM photogrammetry. In *EMC 2008 14th European Microscopy Congress 1–5 September 2008, Aachen, Germany*, pages 549–550. Springer Berlin Heidelberg, Berlin, Heidelberg. doi:10.1007/978-3-540-85156-1{_}275.

- [93] K.-P. Johnsen, C. G. Frase, H. Bosse, and D. Gnieser. SEM image modeling using the modular Monte Carlo model MCSEM. *Metrology, Inspection, and Process Control for Microlithography XXIV*, 7638:76381O, 2010. doi:10.1117/12.846543.
- [94] S. A. Müller, K. N. Goldie, R. Bürki, R. Häring, and A. Engel. Factors influencing the precision of quantitative scanning transmission electron microscopy. *Ultramicroscopy*, 46(1-4):317–334, 10 1992. doi:10.1016/0304-3991(92)90022-C.
- [95] A. Engel and R. Reichelt. Processing of quantitative scanning transmission electron micrographs. *Scanning Microscopy*, 2:285–293, 1988.
- [96] J. S. Wall and M. N. Simon. Scanning Transmission Electron Microscopy of DNA-Protein Complexes. In *DNA-Protein Interactions*, volume 148, pages 589–601. Humana Press, New Jersey, 2001. doi:10.1385/1-59259-208-2:589.
- [97] Globins and Other Nitric Oxide-Reactive Proteins. In K. R. Robert, editor, *Methods in Enzymology*, page 672. Elsevier, 2011.
- [98] V. Krzyżanek and S. Tacke. MASDET2 - software for quantitative STEM imaging. In *European Microscopy Congress 2016: Proceedings*, pages 583–584, Weinheim, Germany, 11 2016. Wiley-VCH Verlag GmbH & Co. KGaA. doi:10.1002/9783527808465.
- [99] V. Krzyżanek, S. A. Müller, A. Engel, and R. Reichelt. MASDET-A fast and user-friendly multiplatform software for mass determination by dark-field electron microscopy. *Journal of Structural Biology*, 165(2):78–87, 2009. doi:10.1016/j.jsb.2008.10.006.
- [100] V. Krzyżanek, N. Sporenberg, U. Keller, J. Guddorf, R. Reichelt, and M. Schönhoff. Polyelectrolyte multilayer capsules: Nanostructure and visualisation of nanopores in the wall. *Soft Matter*, 7(15):7034–7041, 2011. doi:10.1039/c1sm05406f.
- [101] S. Tacke, V. Krzyżanek, H. Nüsse, R. A. Wepf, J. Klingauf, and R. Reichelt. A Versatile High-Vacuum Cryo-transfer System for Cryo-microscopy and Analytics. *Biophysical Journal*, 110(4):758–765, 2016. doi:10.1016/j.bpj.2016.01.024.
- [102] M. Tian, O. Dyck, J. Ge, and G. Duscher. Measuring the areal density of nanomaterials by electron energy-loss spectroscopy. *Ultramicroscopy*, 196(March 2018):154–160, 1 2019. doi:10.1016/j.ultramic.2018.10.009.
- [103] TEM Microscope | Talos L120C | Thermo Fisher Scientific - CZ. URL: <https://www.thermofisher.com/cz/en/home/electron-microscopy/products/transmission-electron-microscopes/talos-l120c-tem.html>.
- [104] SALVE Sub Angstrom Low Voltage Electron Microscopy Project III of Ulm University / FEI company / CEOS / DFG / MWK: Tools - SALVE III microscope. URL: <https://www.salve-project.de/tools/salve3/index.html>.
- [105] LVEM 5 | DeLong Instruments. URL: <https://www.delong.cz/products/lvem5/>.
- [106] Low Voltage Electron Microscope LVEM 25 | DeLong Instruments. URL: <https://www.delong.cz/products/lvem25/>.

- [107] U. Ehlers, R. Herken, B. Herrmann, F. Mayer, and D. G. Robinson. *Methods of Preparation for Electron Microscopy*. Springer, 1987.
- [108] G. McMullan, A. R. Faruqi, D. Clare, and R. Henderson. Comparison of optimal performance at 300keV of three direct electron detectors for use in low dose electron microscopy. *Ultramicroscopy*, 147:156–63, 12 2014. doi:10.1016/j.ultramicro.2014.08.002.
- [109] M. Kuijper, G. van Hoften, B. Janssen, R. Geurink, S. De Carlo, M. Vos, G. van Duinen, B. van Haeringen, and M. Storms. FEI’s direct electron detector developments: Embarking on a revolution in cryo-TEM. *Journal of Structural Biology*, 192(2):179–187, 11 2015. doi:10.1016/j.jsb.2015.09.014.
- [110] R. F. Egerton. Choice of operating voltage for a transmission electron microscope. *Ultramicroscopy*, 145:85–93, 2014. doi:10.1016/j.ultramicro.2013.10.019.
- [111] H. Schatten, J. Walocha, J. Litwin, A. Miodoński, S. Sepsenwol, T. Naguro, H. Nakane, S. Inaga, P. Walther, R. Albrecht, D. Meyer, O. Olorundare, J. Holl, et al. *Scanning Electron Microscopy for the Life Sciences*. Cambridge University Press., 2012.
- [112] A. E. Yakushevska, M. N. Lebbink, W. J. C. Geerts, L. Spek, E. G. van Donselaar, K. A. Jansen, B. M. Humbel, J. A. Post, A. J. Verkleij, and A. J. Koster. STEM tomography in cell biology. *Journal of Structural Biology*, 159(3):381–391, 2007. doi:10.1016/j.jsb.2007.04.006.
- [113] L. Marton and L. I. Schiff. Determination of object thickness in electron microscopy. *Journal of Applied Physics*, 12(10):759–765, 1941. doi:10.1063/1.1712863.
- [114] A. E. Ennos. The origin of specimen contamination in the electron microscope. *British Journal of Applied Physics*, 4(4):101–106, 1953. doi:10.1088/0508-3443/4/4/302.
- [115] C. E. Hall. Electron densitometry of stained virus particles. *The Journal of Biophysical and Biochemical Cytology*, 1(1):1–12, 1 1955. doi:10.1083/jcb.1.1.1.
- [116] E. Zeitler and G. Bahr. Contributions to the quantitative interpretation of electron microscope pictures. *Experimental Cell Research*, 12(1):44–65, 2 1957. doi:10.1016/0014-4827(57)90293-8.
- [117] N. H. Sarkar and P. Sadhukhan. Estimation of Mass-Scattering Coefficient of Biological Samples. *Nature*, 197(4874):1263–1264, 3 1963. doi:10.1038/1971263a0.
- [118] N. H. Sarkar. Mass-scattering cross section of thin carbon films. *Journal of Applied Physics*, 37(12):4389–4394, 1966. doi:10.1063/1.1708048.
- [119] N. H. Sarkar. Mass-scattering cross sections of biological specimens. *Journal of Applied Physics*, 38(4):1830–1831, 1967. doi:10.1063/1.1709768.
- [120] V. E. Cosslett. I.-PROSPECTS FOR SUBSTANCE DIFFERENTIATION BY ELECTRON AND X-RAY MICRO-METHODS*. *Journal of the Royal Microscopical Society*, 78(1-2):1–17, 3 1958. doi:10.1111/j.1365-2818.1958.tb02031.x.
- [121] M. L. DE. Estimation of Mass Thickness of Biological Samples from their Electron Micrographs. *Nature*, 192(4802):547–547, 11 1961. doi:10.1038/192547a0.

- [122] N. R. Silvester and R. E. Burge. A quantitative estimation of the uptake of two new electron stains by the cytoplasmic membrane of ram sperm. *The Journal of biophysical and biochemical cytology*, 6(2):179–188, 1959. doi:10.1083/jcb.6.2.179.
- [123] R. E. Burge and N. R. Silvester. The measurement of mass, thickness, and density in the electron microscope. *The Journal of biophysical and biochemical cytology*, 8(24):1–11, 1960. doi:10.1083/jcb.8.1.1.
- [124] E. Zeitler and G. F. Bahr. A photometric procedure for weight determination of submicroscopic particles quantitative electron microscopy. *Journal of Applied Physics*, 33(3):847–853, 1962. doi:10.1063/1.1777179.
- [125] A. Engel. Molecular weight determination by scanning transmission electron microscopy. *Ultramicroscopy*, 3(March):273–281, 1978. doi:10.1016/S0304-3991(78)80037-0.
- [126] R. Freeman and K. R. Leonard. Comparative mass measurement of biological macromolecules by scanning transmission electron microscopy. *Journal of Microscopy*, 122(3):275–286, 1981. doi:10.1111/j.1365-2818.1981.tb01267.x.
- [127] A. Engel, F. Christen, and B. Michel. Digital acquisition and processing of electron micrographs using a scanning transmission electron microscope. *Ultramicroscopy*, 7(1):45–54, 1981. doi:10.1016/0304-3991(81)90022-X.
- [128] A. A. Sousa and R. D. Leapman. Quantitative STEM mass measurement of biological macromolecules in a 300 kV TEM. *Journal of Microscopy*, 228(1):25–33, 2007. doi:10.1111/j.1365-2818.2007.01819.x.
- [129] V. Krzyzanek and R. Reichelt. High-Resolution Scanning Electron Microscope for Mass Determination: Progress in the Development of a New Nanoanalytical Tool. *Microscopy and Microanalysis*, 13(S03):80–81, 2007. doi:10.1017/S1431927607080403.
- [130] M. Pfaff, E. Müller, M. F. G. Klein, A. Colsmann, U. Lemmer, V. Krzyzanek, R. Reichelt, and D. Gerthsen. Low-energy electron scattering in carbon-based materials analyzed by scanning transmission electron microscopy and its application to sample thickness determination. *Journal of Microscopy*, 243(1):31–39, 2011. doi:10.1111/j.1365-2818.2010.03475.x.
- [131] V. Morandi and P. G. Merli. Contrast and resolution versus specimen thickness in low energy scanning transmission electron microscopy. *Journal of Applied Physics*, 101(11), 2007. doi:10.1063/1.2745333.
- [132] A. Sen, U. Baxa, M. N. Simon, J. S. Wall, R. Sabate, S. J. Saupe, and A. C. Steven. Mass analysis by scanning transmission electron microscopy and electron diffraction validate predictions of stacked β -solenoid model of HET-s prion fibrils. *Journal of Biological Chemistry*, 282(8):5545–5550, 2007. doi:10.1074/jbc.M611464200.
- [133] S. A. Müller and A. Engel. Structure and mass analysis by scanning transmission electron microscopy. *Micron*, 32(1):21–31, 2001. doi:10.1016/S0968-4328(00)00022-6.

- [134] E. Buhr, M. U. Bug, D. Bergmann, P. Cizmar, and C. G. Frase. Simultaneous measurement of lateral and vertical size of nanoparticles using transmission scanning electron microscopy (TSEM). *Measurement Science and Technology*, 28(3), 2017. doi:10.1088/1361-6501/28/3/034002.
- [135] Z. Barkay, I. Rivkin, and R. Margalit. Three-dimensional characterization of drug-encapsulating particles using STEM detector in FEG-SEM. *Micron*, 40(4):480–485, 2009. doi:10.1016/j.micron.2008.12.003.
- [136] T. Volkenandt, E. Müller, and D. Gerthsen. Sample thickness determination by scanning transmission electron microscopy at low electron energies. *Microscopy and Microanalysis*, 20(1):111–123, 2014. doi:10.1017/S1431927613013913.
- [137] E. Buhr, N. Senftleben, T. Klein, D. Bergmann, D. Gnieser, C. G. Frase, and H. Bosse. Characterization of nanoparticles by scanning electron microscopy in transmission mode. *Measurement Science and Technology*, 20(8), 2009. doi:10.1088/0957-0233/20/8/084025.
- [138] T. Woehl and R. Keller. Dark-field image contrast in transmission scanning electron microscopy: Effects of substrate thickness and detector collection angle. *Ultramicroscopy*, 171:166–176, 2016. doi:10.1016/j.ultramicro.2016.08.008.
- [139] M. Čalkovský, E. Müller, M. Hugenschmidt, and D. Gerthsen. Differential electron scattering cross-sections at low electron energies: The influence of screening parameter. *Ultramicroscopy*, 207(August):112843, 12 2019. doi:10.1016/j.ultramicro.2019.112843.
- [140] T. Volkenandt, E. Müller, D. Z. Hu, D. M. Schaadt, and D. Gerthsen. Quantification of sample thickness and in-concentration of InGaAs quantum wells by transmission measurements in a scanning electron microscope. *Microscopy and Microanalysis*, 16(5):604–613, 2010. doi:10.1017/S1431927610000292.
- [141] C. Ophus. Four-Dimensional Scanning Transmission Electron Microscopy (4D-STEM): From Scanning Nanodiffraction to Ptychography and Beyond. *Microscopy and Microanalysis*, 25(3):563–582, 6 2019. doi:10.1017/S1431927619000497.
- [142] B. H. Savitzky, L. A. Hughes, S. E. Zeltmann, H. G. Brown, S. Zhao, P. M. Pelz, E. S. Barnard, J. Donohue, L. R. DaCosta, T. C. Pekin, E. Kennedy, M. T. Janish, M. M. Schneider, et al. py4DSTEM: a software package for multimodal analysis of four-dimensional scanning transmission electron microscopy datasets. Technical report, 2020. URL: <http://arxiv.org/abs/2003.09523>--.
- [143] J. M. LeBeau, S. D. Findlay, L. J. Allen, and S. Stemmer. Position averaged convergent beam electron diffraction: Theory and applications. *Ultramicroscopy*, 110(2):118–125, 1 2010. doi:10.1016/j.ultramicro.2009.10.001.
- [144] X. Mu, A. Mazilkin, C. Sprau, A. Colsmann, and C. Kübel. Mapping structure and morphology of amorphous organic thin films by 4D-STEM pair distribution function analysis. *Microscopy*, 68(4):301–309, 2019. doi:10.1093/jmicro/dfz015.

- [145] O. Panova, C. Ophus, C. J. Takacs, K. C. Bustillo, L. Balhorn, A. Salleo, N. Balsara, and A. M. Minor. Diffraction imaging of nanocrystalline structures in organic semiconductor molecular thin films. *Nature Materials*, 18(8):860–865, 8 2019. doi:10.1038/s41563-019-0387-3.
- [146] O. Panova, X. C. Chen, K. C. Bustillo, C. Ophus, M. P. Bhatt, N. Balsara, and A. M. Minor. Orientation mapping of semicrystalline polymers using scanning electron nanobeam diffraction. *Micron*, 88:30–36, 9 2016. doi:10.1016/j.micron.2016.05.008.
- [147] D. Srolovitz, T. Egami, and V. Vitek. Radial distribution function and structural relaxation in amorphous solids. *Physical Review B*, 24(12):6936–6944, 1981. doi:10.1103/PhysRevB.24.6936.
- [148] S. Goudsmit and J. L. Saunderson. Multiple scattering of electrons. *Physical Review*, 57(6):552, 1940. doi:10.1103/PhysRev.57.552.2.
- [149] H. W. Lewis. Multiple scattering in an infinite medium. *Physical Review*, 78(5):526–529, 1950. doi:10.1103/PhysRev.78.526.
- [150] C. Negreanu, X. Llovet, R. Chawla, and F. Salvat. Calculation of multiple-scattering angular distributions of electrons and positrons. *Radiation Physics and Chemistry*, 74(5):264–281, 2005. doi:10.1016/j.radphyschem.2005.07.006.
- [151] W. Bothe. Durchgang von Elektronen durch Materie. In H. Geiger and W. Bothe, editors, *Handbuch der Physik 22,2: Negative und positive Strahlen*, pages 1–74. Springer, Berlin, 2nd edition, 1933.
- [152] V. E. Cosslett and R. N. Thomas. Multiple scattering of 5-30 keV electrons in evaporated metal films: I. Total transmission and angular distribution. *British Journal of Applied Physics*, 15(8):883–907, 1964. doi:10.1088/0508-3443/15/8/303.
- [153] J. A. Crowther. On the scattering of Homogeneous β -Rays and the number of Electrons in the Atom. *Proceedings of the Royal Society of London. Series A, Containing Papers of a Mathematical and Physical Character*, 84(570):226–247, 9 1910. doi:10.1098/rspa.1910.0074.
- [154] S. A. Müller and A. Engel. Biological Scanning Transmission Electron Microscopy: Imaging and Single Molecule Mass Determination. *CHIMIA International Journal for Chemistry*, 60(11):749–753, 2006. doi:10.2533/chimia.2006.749.
- [155] F. Krumeick. Properties of electrons, their interactions with matter and applications in electron microscopy. Technical report, ETH, 2011. URL: <http://www.microscopy.ethz.ch/downloads/Interactions.pdf>.
- [156] V. E. Cosslett and R. N. Thomas. Multiple scattering of 5 - 30 keV electrons in evaporated metal films III: Backscattering and absorption. *British Journal of Applied Physics*, 16(6):779–796, 1965. doi:10.1088/0508-3443/16/6/303.
- [157] H. Niedrig. Physical background of electron backscattering. *Scanning*, 1(1):17–34, 1978. doi:10.1002/sca.4950010103.

- [158] A. M. D. Assa'd and M. M. E. Gomati. Backscattering Coefficients for Low Energy Electrons. *Scanning Microscopy*, 12(1):185–192, 1998.
- [159] W.-R. Lin, Y.-J. Chuang, C.-H. Lee, F.-G. Tseng, and F.-R. Chen. Fabrication and characterization of a sensitivity multi-annular backscattered electron detector for desktop SEM. *Sensors*, 18(3093):1–13, 2018. doi:10.1109/ISNE.2018.8394642.
- [160] J. Seiter, E. Müller, H. Blank, H. Gehrke, D. Marko, and D. Gerthsen. Backscattered electron SEM imaging of cells and determination of the information depth. *Journal of Microscopy*, 254(2):75–83, 2014. doi:10.1111/jmi.12120.
- [161] M. Dapor, N. Bazzanella, L. Toniutti, A. Miotello, and S. Gialanella. Backscattered electrons from surface films deposited on bulk targets: A comparison between computational and experimental results. *Nuclear Instruments and Methods in Physics Research, Section B: Beam Interactions with Materials and Atoms*, 269(14):1672–1674, 2011. doi:10.1016/j.nimb.2010.11.016.
- [162] M. Dapor, N. Bazzanella, L. Toniutti, A. Miotello, M. Crivellari, and S. Gialanella. Backscattered electrons from gold surface films deposited on silicon substrates: A joint experimental and computational investigation to add new potentiality to electron microscopy. *Surface and Interface Analysis*, 45(2):677–681, 2013. doi:10.1002/sia.5144.
- [163] E. Müller and D. Gerthsen. Composition quantification of electron-transparent samples by backscattered electron imaging in scanning electron microscopy. *Ultramicroscopy*, 173(March 2016):71–75, 2017. doi:10.1016/j.ultramicro.2016.12.003.
- [164] H. Kim, T. Negishi, M. Kudo, H. Takei, and K. Yasuda. Quantitative backscattered electron imaging of field emission scanning electron microscopy for discrimination of nano-scale elements with nm-order spatial resolution. *Journal of Electron Microscopy*, 59(5):379–385, 2010. doi:10.1093/jmicro/dfq012.
- [165] A. Garitagoitia Cid, R. Rosenkranz, M. Löffler, A. Clausner, Y. Standke, and E. Zschech. Quantitative analysis of backscattered electron (BSE) contrast using low voltage scanning electron microscopy (LVSEM) and its application to AlGaN/GaN layers. *Ultramicroscopy*, 195:47–52, 12 2018. doi:10.1016/j.ultramicro.2018.08.026.
- [166] E. Sánchez, M. Torres Deluigi, and G. Castellano. Mean atomic number quantitative assessment in backscattered electron imaging. *Microscopy and Microanalysis*, 18(6):1355–1361, 2012. doi:10.1017/S1431927612013566.
- [167] D. F. Kyser and K. Murata. Application of Monte Carlo Simulation to Electron Microprobe Analysis of Thin Flms on Substrates. In *Proceeding of a Workshop on a Use of Monte Carlo Calculations in Electron Probe Microanalysis and Scanning Electron Microscopy*, pages 129–138, Gaithersburg, 1977. U.S. Government Printing Office.
- [168] P. B. DeNee. Measurement of mass and thickness of respirable dust particles by SEM backscatter electron microscopy. *Scanning Electron Microscopy*, 11:771–746, 1978.
- [169] P. Merli, V. Morandi, and F. Corticelli. Backscattered electron imaging and scanning transmission electron microscopy imaging of multi-layers. *Ultramicroscopy*, 94(2):89–98, 2 2003. doi:10.1016/S0304-3991(02)00217-6.

- [170] M. Dapor. Backscattering of low energy electrons from carbon films deposited on aluminum: A Monte Carlo simulation. *Journal of Applied Physics*, 95(2):718–721, 2004. doi:10.1063/1.1633655.
- [171] Y. T. Yue, H. M. Li, and Z. J. Ding. Monte Carlo simulation of secondary electron and backscattered electron images for a nanoparticle-matrix system. *Journal of Physics D: Applied Physics*, 38(12):1966–1977, 2005. doi:10.1088/0022-3727/38/12/017.
- [172] T. Kowoll, E. Müller, S. Fritsch-Decker, S. Hettler, H. Störmer, C. Weiss, and D. Gerthsen. Contrast of Backscattered Electron SEM Images of Nanoparticles on Substrates with Complex Structure. *Scanning*, 2017:1–12, 2017. doi:10.1155/2017/4907457.
- [173] A. M. D. Assa'd. Monte Carlo calculation of the backscattering coefficient of thin films of low on high atomic number materials and the reverse as a function of the incident electron energy and film thickness. *Applied Physics A*, 124(10):699, 10 2018. doi:10.1007/s00339-018-2073-8.
- [174] A. M. Assa'd. Monte Carlo computation of the influence of carbon contamination layer on the energy distribution of backscattered electrons emerging from Al and Au. *Jordan Journal of Physics*, 12(1):37–44, 2019.
- [175] R. Skoupý and V. Krzyžánek. Determination of thickness refinement using STEM detector segments. In *NANOCON 2018 - Conference Proceedings, 10th Anniversary International Conference on Nanomaterials - Research and Application*, pages 677–681, 2019.
- [176] R. Skoupy and V. Krzyzanek. Determining the accuracy of qSTEM for use in electron beam induced mass loss studies. In *Mikroskopie 2019: Proceedings*, pages 105–106. Československá mikroskopická společnost, Praha, 2019.
- [177] R. Skoupý and V. Krzyžánek. Assessing the thickness error rate of quantitative STEM measurements. In *Proceedings from the 14th multinational congress on microscopy*, page 498, Belgrade, 2019.
- [178] R. Skoupy, J. Nebesarova, M. Slouf, and V. Krzyzanek. Ultramicroscopy Quantitative STEM imaging of electron beam induced mass loss of epoxy resin sections. *Ultramicroscopy*, 202(March):44–50, 2019. doi:10.1016/j.ultramicroscopy.2019.03.018.
- [179] R. Reichelt, E. Carlemalm, W. Villiger, and A. Engel. Concentration determination of embedded biological matter by scanning transmission electron microscopy. *Ultramicroscopy*, 16(1):69–80, 1985. doi:10.1016/S0304-3991(85)80009-7.
- [180] M. Aronova, A. Sousa, G. Zhang, and R. Leapman. Limitations of beam damage in electron spectroscopic tomography of embedded cells. *Journal of Microscopy*, 239(3):223–232, 9 2010. doi:10.1111/j.1365-2818.2010.03376.x.
- [181] M. A. Hayat. *Principles and Techniques of Electron Microscopy: Biological Applications*. Cambridge University Press., 2000.
- [182] J. H. Luft. Improvements in epoxy resin embedding methods. *The Journal of Biophysical and Biochemical Cytology*, 9(2):409–414, 2 1961. doi:10.1083/jcb.9.2.409.

- [183] A. M. Glauert and P. R. Lewis. *Biological Specimen Preparation for Transmission Electron Microscopy*. Princeton University Press, Princeton, 12 1998. doi:10.1515/9781400865024.
- [184] R. Skoupý, V. Krzyžánek, L. Kocová, and J. Nebesářová. Electron beam induced mass loss dependence on aging of Epon resin sections. In A. Kittel and B. Pecz, editors, *12th Multinational Congress on Microscopy: Proceedings*, pages 112–113. Akademiai Kiado, Budapest, 2015.
- [185] R. Skoupy, M. Slouf, and V. Krzyzanek. 4D-qSTEM-SRIP: calibration-less local thickness estimation of amorphous samples. (*submitted*).
- [186] M. Machala, P. Kulich, O. Sery, S. Marvanova, R. Skoupy, A. Rusnak, P. Mikuska, and Z. Vecera. The deposition of inhaled titanium nanoparticles in mice organs. In *Toxicology Letters: Abstracts of the 52nd Congress of the European Societies of Toxicology (EUROTOX) Fibres Congress Center Seville*, volume 258, page S277, 2016. doi:10.1016/j.toxlet.2016.06.1969.

List of abbreviations

(A)BF	(Annular) Bright Field
(A)DF	(Annular) Dark Field
AE/S	Auger Electron/Spectroscopy
AFM	Atomic Force Microscopy
BSE	Back-Scatter Electron
BSV	Tomato Bushy Stunt
CBS	Circular Back-scatter Detector
CCD	Charge-Coupled Device
CL	CathodoLuminescence
CMOS	Complementary Metal Oxide Semiconductor
DLA	Discrete Loss Approximation
EBIC	Electron Beam-Induced Current
EBSD	Electron Back-Scatter Diffraction
EDX, EDS	Energy Dispersive X-ray Spectroscopy
EELS	Electron Energy Loss Spectroscopy
ETD	Everhart-Thornley Detector
FIB-SEM	Focused Ion Beam Scanning Electron Microscope
HAADF	High Angle Annular Dark field
HPF	High Pressure Freezer
LLE	Low-Loss Electrons
LM	Light Microscope
MC	Monte Carlo
NPs	Nano Particles
PACBED	Position-Averaged Convergent Beam Electron Diffraction
PDF	Pair Distribution Function
ppm	parts per million
PS, PMMA	PolyStyrene, Poly(MethylMethAcrylate)
qBSE	Quantitative Back-Scattered Electron imaging
DQE	Detection Quantum Efficiency
qSTEM	Quantitative Scanning Transmission Electron Microscopy
SBF-SEM	Serial Block Face Scanning Electron Microscope
SDA	Slowing Down Approximation
SE	Secondary Electron
SEM	Scanning Electron Microscope
SNCLM	Scanning Nearfield CathodoLuminescence Microscopy
SNOM	Scanning Near-field Optical Microscopy
STEM	Scanning Transmission Electron Microscope/Microscopy
TEM	Transmission Electron Microscope
TLD	Through the Lens Detector
TMV	Tobacco Mosaic Virus
WD	Working Distance
WDX, WDS	Wavelength-dispersive X-ray Spectroscopy
μXRF	Micro X-Ray Fluorescence